Accelerated Lifetime Testing of Off-Line LED Drivers

Beschleunigte Lebensdaueruntersuchung von netzbetriebenen LED Betriebsgeräten
Zur Erlangung des akademischen Grades Doktor-Ingenieur (Dr.-Ing.)
Genehmigte Dissertation von Ferdinand Tilman Keil aus Hünfeld
Tag der Einreichung: 20. September 2022, Tag der Prüfung: 16. November 2022

1. Gutachten: Prof. Dr.-Ing. Klaus Hofmann
2. Gutachten: Prof. Dr.-Ing. Tran Quoc Khanh
Darmstadt, Technische Universität Darmstadt

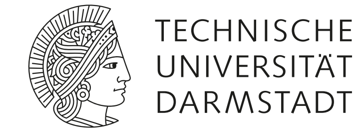

Electrical Engineering and Information Technology Department
Integrated Electronic Systems Lab

Accelerated Lifetime Testing of Off-Line LED Drivers
Beschleunigte Lebensdaueruntersuchung von netzbetriebenen LED Betriebsgeräten

Accepted doctoral thesis by Ferdinand Tilman Keil

Date of submission: 20. September 2022
Date of thesis defense: 16. November 2022

Darmstadt, Technische Universität Darmstadt

Bitte zitieren Sie dieses Dokument als:
URN: urn:nbn:de:tuda-tuprints-237821
URL: http://tuprints.ulb.tu-darmstadt.de/23782
Jahr der Veröffentlichung auf TUprints: 2023

Dieses Dokument wird bereitgestellt von tuprints,
E-Publishing-Service der TU Darmstadt
http://tuprints.ulb.tu-darmstadt.de
tuprints@ulb.tu-darmstadt.de

Die Veröffentlichung steht unter folgender Creative Commons Lizenz:
Namensnennung – Weitergabe unter gleichen Bedingungen 4.0 International
https://creativecommons.org/licenses/by-sa/4.0/

This work is licensed under a Creative Commons License:
Attribution–ShareAlike 4.0 International
https://creativecommons.org/licenses/by-sa/4.0/

Für Laura.

Prüft aber alles und das Gute behaltet.
1. Thessalonicher 5-21

Erklärungen laut Promotionsordnung

§ 8 Abs. 1 lit. c PromO

Ich versichere hiermit, dass die elektronische Version meiner Dissertation mit der schriftlichen Version übereinstimmt.

§ 8 Abs. 1 lit. d PromO

Ich versichere hiermit, dass zu einem vorherigen Zeitpunkt noch keine Promotion versucht wurde. In diesem Fall sind nähere Angaben über Zeitpunkt, Hochschule, Dissertationsthema und Ergebnis dieses Versuchs mitzuteilen.

§ 9 Abs. 1 PromO

Ich versichere hiermit, dass die vorliegende Dissertation selbstständig und nur unter Verwendung der angegebenen Quellen verfasst wurde.

§ 9 Abs. 2 PromO

Die Arbeit hat bisher noch nicht zu Prüfungszwecken gedient.

Darmstadt, 20. September 2022

Ferdinand Keil

Kurzfassung

Innerhalb von nur zehn Jahren haben LEDs den größten Marktanteil im Bereich der Beleuchtung erobert. Dank ihrer hohen Energieeffizienz und langen Lebensdauer sind sie die erste Wahl für viele Anwendungen. Jedoch werden immer noch Ausfälle von LED basierten Leuchten beobachtet. Im Fall von defekten Straßenleuchten wird darüber sogar in der Zeitung berichtet. Vorangegangene Untersuchungen haben gezeigt, dass die meisten Ausfälle auf das Betriebsgerät zurückzuführen sind. Diese Arbeit versucht zu klären wie lange moderne netzbetriebene Betriebsgeräte in einer gegebenen Umgebungsbedingung überleben können, welche Umweltfaktoren und Eigenschaften des Betriebsgerätes die Lebensdauer maßgeblich beeinflussen und welches die die Lebensdauer begrenzenden Ausfallmechanismen sind.

Es wird eine beschleunigte Lebensdauerstudie mit insgesamt 75 geprüften Geräten vorgestellt und ihre Ergebnisse werden analysiert. Die Tests werden bei vier Umgebungsbedingungen durchgeführt: trockene Hitze bei 85 °C sowie feuchte Hitze bei 65 °C und 90 % relativer Luftfeuchtigkeit sowie 75 °C/75 % und 85 °C/85 %. Während der Versuche fallen 39 Prüflinge aus. Eine erste Analyse widmet sich der Degradation der Aluminium-Elektrolytkondensatoren in trockener Hitze. Es kann gezeigt werden, dass diese vernachlässigbar ist. Nachfolgend wird die Ausfallursache von 27 Prüflingen mittels einer forensischen Untersuchung bestimmt. Am häufigsten sind dabei Kurzschlüsse im Leiterplattensubstrat und Defekte von IC Gehäusen zu beobachten. Es kann ebenfalls gezeigt werden, dass Metalloxid-Varistoren in bestimmten Schaltungskonfigurationen gehäuft ausfallen.

Für drei Betriebsgerätetypen, für die vollständige Datensätze vorliegen, werden die Parameter von zwei physikalischen Lebensdauermodellen bestimmt. Anhand einer grafischen Auswertung dieser Modelle wird gezeigt, dass diese Treiber mit großer Wahrscheinlichkeit länger betrieben werden können als vom Hersteller garantiert wird. Dank eines erweiterten Ansatzes können die Modellparameter auch noch für drei Geräte mit rechts-zensierten Datenpunkten bestimmt werden. Auch diese werden höchstwahrscheinlich die vom Hersteller angegebenen Lebensdauern erreichen. Mit Hilfe der Cox Regression, einer Methode aus dem Bereich der Ereigniszeitanalyse, kann bestimmt werden welche Eigenschaften des Betriebsgerätes maßgeblichen Einfluss auf dessen Lebensdauer haben. Die Modellparameter werden für die Ausfälle bei 85 °C/85 % berechnet. Nachdem die drei besten Modelle anhand eines Anpassungsmaßes ausgewählt worden sind, zeigt sich, dass die maximale Ausgangsleistung, die Einstellbarkeit des Ausgangsstromes und das verwendete Leiterplattensubstrat die entscheidenden Eigenschaften sind. Ausgehend von diesen Erkenntnissen werden Empfehlungen für künftige Schaltungsentwürfe gegeben.

Diese Arbeit kann anhand einer beschleunigten Lebensdauerstudie zeigen, dass moderne netzbetriebene Betriebsgeräte die von den Herstellern angegebenen Lebensdauern erreichen können. Ausfälle können jedoch beobachtet werden, wenn die Geräte hoher Luftfeuchtigkeit ausgesetzt sind. Der Einsatz von FR-4 als Leiterplattensubstrat kann die Lebensdauer signifikant erhöhen. Falls die Geräte dennoch ausfallen, so sind Kurzschlüsse im Leiterplattensubstrat und Defekte an IC Gehäusen die häufigsten Ursachen.

Abstract

It took just ten years for light-emitting diodes (LEDs) to become the most successful lighting technology by market share. Their high energy efficiency and long lifetime make them the first choice in many lighting applications. However, failures of LED based luminaires can still be observed. If public lighting installations such as street lights fail it can even make the news. Previous research has shown that the driver is the culprit in most of these cases. This work tries to answer how long modern drivers can survive in a given environmental condition, which external factors and driver properties affect the lifetime and what the lifetime limiting failure modes are.

An accelerated lifetime study with a total of 75 tested devices is conducted and its results are analysed. Four different environmental conditions are selected for the tests, namely dry heat at 85 °C and damp heat at 65 °C and 90 % relative humidity as well as 75 °C/75 % and 85 °C/85 %. During testing 39 failures are observed. A first analysis focuses on the degradation of aluminium electrolytic capacitors in dry heat. It can be shown that the parametric changes are negligible. This is followed by a forensic failure mode analysis that successfully uncovers the failure modes of 27 failed devices. Dielectric breakdown of the printed circuit board (PCB) and integrated circuit (IC) package defects are determined to be the most common failure causes. It is also demonstrated that metal oxide varistors (MOVs) are at risk of failing in certain circuit configurations.

Two physical accelerated failure time models get fitted for three drivers with complete datasets. Plotting the resulting lifetime model for a range of temperature/humidity combinations shows that these drivers will likely outlast the lifetime guaranteed by the manufacturer in their respective data sheets. An extension is proposed to apply the models to three drivers whose datasets contain right-censored values. It can be demonstrated that these drivers will meet the guaranteed lifetime as well. The Cox proportional hazards model (Cox PH model), a model from the field of survival analysis, is applied to the data from the 85 °C/85 % condition to identify driver properties that affect the lifetime. The three best fitting models are selected and their parameters are whether a driver's output current is programmable, its maximum output power in Watt and which PCB substrate was used for the circuit assembly. Based on the previous results a list of recommendations for future off-line driver designs is compiled.

In conclusion, this work demonstrates that modern off-line LED drivers can reach the manufacturer specified lifetimes based on the results of the accelerated life study. Drivers fail if subjected to high levels of humidity. Choosing FR-4 as the PCB substrate can significantly lower a driver's risk of failure. If it fails, the most common failure modes are dielectric breakdown of the PCB and a defect of an IC package.

Contents

Glossary xix

Acronyms xxi

1 Introduction 1

1.1 What Are LED Drivers and How Do They Work . . . 3

1.2 Outline of This Work . . . 5

2 Methods 7

2.1 Central Requirements for the Test Setup . . . 7

2.1.1 Test Using Damp Heat . . . 7

2.1.2 Automated Monitoring of the Required Parameters . . . 9

2.1.3 Reliable Test Setup . . . 9

2.2 Selection of the Drivers for the Test . . . 10

2.3 Experimental Setup . . . 10

2.3.1 Selection of the Environmental Conditions . . . 12

2.4 Test Automation . . . 13

2.5 Failure Mode Analysis . . . 15

2.6 Physical Models for Life Tests with Constant Stress . . . 16

2.7 Survival Analysis . . . 18

2.7.1 Kaplan-Meier Method . . . 18

2.7.2 Cox Proportional Hazards Model . . . 20

3 Results 23

3.1 Degradation of Aluminium Electrolytic Capacitors . . . 23

3.2 Failure Modes . . . 27

3.2.1 Dielectric Breakdown of the PCB . . . 27

3.2.2 IC Package Failure . . . 42

3.2.3 Metal Oxide Varistor . . . 46

3.2.4 MOSFET . . . 51

3.2.5 Metallised Film Capacitor . . . 55

3.2.6 Diode . . . 59

3.2.7 Inductor . . . 62

3.2.8 Resistor . . . 64

4 Discussion 67

4.1 Lifetime Extrapolation With Physical Models . . . 67

4.1.1 Model Fitting for Censored Datasets . . . 70

4.1.2 Estimated Driver Lifetime in Different Climatic Conditions . . . 72

4.2 Survival Analysis of the Accelerated Lifetime Test Results 75
4.3 Improving the Robustness of Off-Line LED Drivers 80

5 Conclusion **83**
5.1 Summary 83
5.2 Outlook 84

A List of All Tested Devices by UID **95**

List of Own Publications **97**

Supervised Theses **99**

List of Figures

1.1 Global lighting sales by technology. It is evident that the market share of the light-emitting diode (LED) based luminaires has increased exponentially over the shown ten year interval. The prognosis for 2025 has been drawn hatched to indicate the associated uncertainty. Adapted from [71]. . . . 1
1.2 Two pie charts showing which failure modes are most common in LED based luminaires. Adapted from [88]. . . . 2

2.1 Lifetime of an LED driver vs. case temperature as specified by the manufacturer [97]. . . . 8
2.2 Schematic diagram showing the equipment used in the experiments as well as the wiring between the devices under test (DUTs) and the test gear. Each chamber has a capacity of up to 15 drivers, however for illustrative purposes the wiring for only one driver is shown. . . . 11
2.3 Trade-off between time invested to make a task more efficient and actual time saved presented in matrix form [49].[1] . . . 13
2.4 Flow chart illustrating how the applications for test automation, data processing and analysis work together and interact with the test equipment. The directory or file icon indicate that output is stored in files for later processing. . . . 14
2.5 Flow chart illustrating the chosen failure mode analysis approach. Based on [24, p. 4-207]. . . . 16

3.1 Bar chart illustrating the frequency of the different failure modes identified in the tested devices. 27
3.2 Pictures showing the breakdown on the printed circuit board (PCB) between two inductors for all three failed devices. The failure mode is highly consistent, presenting an almost identical sight in the three devices. . . . 29
3.3 Plots of primary side root mean square (RMS) current and power factor for the three failed devices. The three devices show identical behaviour: before the failure the current increases while the power factor (PF) simultaneously decreases. Due to equipment malfunction the plot for the third driver shows a gap in the data. . . . 30
3.4 Analysis of the PCB from the failed device V037. First image shows the PCB before testing for reference. Burn marks are shown before and after the soot is cleaned up with isopropyl alcohol. Last image shows the PCB after cleaning and with the top side components in a transparent overlay (transformer yellow, diode orange, aluminium electrolytic capacitor turquoise, metal film capacitor red, inductor purple). . . . 31
3.5 Event tree and analysis to determine the root cause for the dielectric failure of device V037. . 32
3.6 Detailed analysis of the dielectric breakdown of device V068, from the location of the actual failure to the circuit schematic and finally the voltage difference between the nodes where the failure occurred. . . . 34
3.7 Damage on the PCB of driver V111. The damaged components can be referenced using the assigned designators. The magnified image highlights the breakdown that short-circuits diode D2. 35
3.8 Event tree analysis of the failure of device V111. . . . 36

3.9 Analysis of the failure of driver Vossloh-Schwabe ECXE 1050.233. The magnifier in the first image indicates where the failure was observed but on a new PCB. The first detail image also shows a new PCB. The breakdown on the devices V118 and V119 can be seen in the two following detail images. The voltage across the two circuit nodes where the breakdown occurred reaches almost 500 V. 38
3.10 Event tree analysis of the failure of the driver Vossloh-Schwabe ECXe 1050.233. 39
3.11 Analysis of the failure of driver Vossloh-Schwabe ECXE 700.199. The magnifier in the first image indicates where the failure was observed but on a new PCB. The first detail image also shows a new PCB. The distance between the two circuit nodes measures barely 0.5 mm. 40
3.12 Simplified schematic of driver Vossloh-Schwabe ECXE 700.199. The path of the dielectric breakdown is indicated by a lightning icon. The trace that burnt-off as a consequence of that short is drawn dashed. 41
3.13 switched-mode power supply (SMPS) integrated circuit (IC) *LNK302DN* on the PCB and detail images of the three ICs showing cracks after they had failed. The images are shown in greyscale to enhance the contrast of the cracks. 43
3.14 Comparison between the layout recommended by the IC's manufacturer [76] and the actual layout found on the PCB of driver OSRAM OT 40/120-277/1A0 4DIMLT2 E. The chip has been removed so that the top copper layout is unobstructed. The layout is missing a copper fill connected to the IC's pins. 43
3.15 Pictures of the damaged ICs from the four failed devices. The damage pattern is almost identical between the four images. 44
3.16 Comparison of the manufacturer recommended layout for the IC [114] and the actual implementation on the PCB of driver Vossloh-Schwabe ECXd 700.149. There is no copper fill connected to the IC's pins in the implementation. 45
3.17 Schematic of the electromagnetic interference (EMI) filter circuit of the WE-EF ED100-66/700-1050/230-50-60/O-O. The topology is unusually complex, as two filter sections, each consisting of a common-mode choke, metal film capacitor and metal oxide varistor (MOV), have been connected back to back. 47
3.18 Test setup for measuring the voltage and current at MOV RV2 of the driver WE-EF ED100-66/700-1050/230-50-60/O-O and the resulting measurement results. 48
3.19 This section shows two metal film capacitors and an MOV that failed during the testing of the driver LUMNIUM 54H-120B-GM-0450 in an 85 °C/85 % environment. The failed MOV is identified to be the root failure cause for the device. 50
3.20 Simplified schematic of the driver LUMNIUM 54H-120B-GM-0450 and measurement results for the MOV RV2. 50
3.21 Bottom side of the failed device of driver type N/A LGM52W041P2 next to a simplified schematic. The component designators of the damaged components can easily be cross referenced between the schematic and the actual circuit. 52
3.22 Event tree analysis of the failure of device V137. 53
3.23 Damaged components on the two sub-assemblies of the failed device V097. Note that the two damaged resistors on the left side of the control PCB did play a role in the failure of the device. 54
3.24 PCB of the device V149 showing two badly damaged film capacitors. Connection to mains is coming from the left side, the main converter can be found to the right. Figure 3.24b shows that molten debris from one of the caps made its way between the pins of the bridge rectifier. . 56
3.25 Plots showing the measured RMS current, power factor and temperature for the device V149. The power factor increases over time, while temperature and primary side current stay almost constant. 56

3.26 PCB of the device V065 after testing in 85 °C/85 %. The damaged capacitors C206 and C207 can be seen surrounding the grey cylinder in the center of the detail image. Both feature cracks in their case, but the damage to C207 is the most drastic. 57
3.27 This data was recorded during the testing of V065. Shown here are the RMS input current, power factor, current total harmonic distortion (THD) and output current ripple. The slow increase in current ripple proves that the output decoupling capacitor's performance degraded significantly over the course of the experiment. 58
3.28 Reverse engineered schematic of the filter section of the driver Philips CertaDrive 60W 360mA 170V 230V. Parts of the circuit have been left out as they were neither damaged nor are they conducive to the understanding of the failure. 60
3.29 An event tree analysis is conducted to identify the root failure cause for the driver Philips CertaDrive 60W 360mA 170V 230V. It is clear, that only the failure of diode D13 explains the observed failure signature. 61
3.30 Detail images showing the damaged components on the driver Philips CertaDrive 60W 360mA 170V 230V. The inductor shown in the right image is connected in parallel to the resistor on the left. The burn mark in the inductor is approximately 2 mm long and 150 µm wide. 61
3.31 The top side of the PCB of device V134 shows no serious damage. However, under the microscope the fused open winding of inductor L1 can clearly be seen. Figure 3.31c also shows signs of corrosion as evidenced by the bright green copper oxide. 63
3.32 Schematic of the driver Vossloh-Schwabe ECXe 350.298 from the mains input to the primary side of the SMPS circuit. 64

4.1 Intensity plots visualizing the Peck and Intel model after fitting them for two drivers with complete data. The lifetimes specified by the manufacturers in the data sheets are marked with solid lines. A dashed line indicates the respective temperature limit for each lifetime. . . 68
4.2 Intensity plots visualizing the Peck and Intel model after fitting them for three drivers. The data for these three drivers contained one right-censored value each. The lifetimes specified by the manufacturers in the data sheets are marked with solid lines. A dashed line indicates the respective temperature limit for each lifetime. 71
4.3 Temperature (red) and relative humidity (blue) readings for five selected cities between January 1st, 2017 and December 31st, 2021. The axes are scaled identically between all five plots. Each data point represents the rolling average calculated over two days worth of hourly data. 73
4.4 Plot showing the ten best fitting Cox proportional hazards models (Cox PH models), sorted by their Akaike information criterion (AIC) value. Note that the first three models have almost identical values. 77
4.5 Scatter plots illustrating the correlation between $\beta_{\text{programmable}}$ and two other parameters. The diameter of the circles is proportional to the number of drivers that feature this combination of parameters. In case of a perfect correlation, two equally sized circles could be seen along one of the diagonals. 79
4.6 Illustration of the wavesoldering process. This is a continuous process, the PCBs get dragged through it on a conveyor belt. Please note the flux sprayer at the beginning of the process. It completely covers the PCB's area with liquid flux. 80
4.7 Frequency of the different failure modes distinguished by the base material used for circuit's PCB. 81
4.8 Pie chart illustrating the distribution of the observed failure modes. Dielectric breakdown of the circuit board was by far the most frequent failure mode. The devices where the failure mode could not be identified were not taken into account for this plot. 81

List of Tables

1.1 Comparison of the three most commonly used SMPS topologies. 4

2.1 Most important technical specifications of the two climate chambers used for the tests [99, 98]. 9
2.2 List of the test equipment used in the experimental setup. 10

3.1 List of lifetimes for all drivers that were tested in damp heat. 25

3.2 Capacitance and equivalent series resistance (ESR) values for aluminium electrolytic capacitors from a test in dry heat at 85 °C. The capacitors were desoldered from the tested devices after the experiment was terminated. Datasheet specifications are included for reference. 26

4.1 Parameters for the Peck and Intel model after fitting them for multiple drivers. The data available for the last three drivers contained right-censored lifetimes. The parameters shown have been calculated using the end of the test as the time of failure. 69

4.2 Extrapolated lifetimes for five cities with different climates. Lifetimes over 10 000 000 h were clipped as they are physically impossible. 74

4.3 Properties of the drivers that were used as covariates in the various Cox PH models. 76

4.4 Model parameters for the three Cox PH models with the lowest AIC value. Only the exponent of the value for the parameters β is given as it is easier to interpret. The p-values are given to indicate whether the effect is statistically significant. 78

4.5 Minimum required isolation distance as specified by four different international standards. The two peak voltage levels were chosen to represent line voltage and rectified line voltage as commonly found in the power factor correction (PFC) stage. 82

Glossary

back EMF Back electromotive force is caused by electromagnetic induction in an inductor. It opposes the change in current which induced it. The relationship is defined in Lenz's law.

FR-2 Composite material consisting of paper impregnated with epoxy resin. Used for printed circuit boards in low-cost applications. Performance is generally inferior compared to FR-4.

FR-4 Composite material consisting of woven fiberglass cloth impregnated with epoxy resin. Commonly used for printed circuit boards.

JEDEC The JEDEC Solid State Technology Association is an American semiconductor engineering trade organisation. The acronym stems from its earlier name, Joint Electron Device Engineering Council.

SO-8 Small outline IC package with eight pins. Compact size of just $3.9 \times 4.9\,\mathrm{mm}^2$. Standardized by JEDEC.

Acronyms

AIC Akaike information criterion
AiF Arbeitsgemeinschaft industrieller Forschungsvereinigungen
API application programming interface

CA California
CI confidence interval
COTS commercial off-the-shelf
Cox PH model Cox proportional hazards model
C-SAM c-mode scanning acoustic microscope

DALI digital adressable lighting interface
DAQ data acquisition unit
DUT device under test

EMC electromagnetic compatibility
EMI electromagnetic interference
ESD electrostatic discharge
ESR equivalent series resistance

FL Florida

GPIB general purpose interface bus

IC integrated circuit
IEA International Energy Agency
IGF Industrial Collective Research

JSON JavaScript object notation

LCR inductance (L), capacitance (C) and resistance (R)
LED light-emitting diode

MI Michigan
MOSFET metal-oxide-semiconductor field-effect transistor
MOV metal oxide varistor
MUX multiplexer

NM New Mexico

OS operating system

PCB printed circuit board

PF power factor
PFC power factor correction
PRC People's Republic of China

RMS root mean square

SMPS switched-mode power supply
SMT surface-mount technology
SSL solid state lighting

THD total harmonic distortion
THT through-hole technology

UID unique identifier
USA United States of America
USB universal serial bus

VHF very high frequency

ZnO zinc oxide
ZVEI Verband der Elektro- und Digitalindustrie

1 Introduction

Over the past ten years LED based lighting – also called solid state lighting (SSL) – has become the dominant lighting technology. Its superiority in terms of efficacy, longevity and light quality has made it the best choice for all but the most exotic applications. The exponential rise in market share of LED lighting from 2010 to 2020 is illustrated in Figure 1.1. By 2025, the International Energy Agency (IEA) expects LEDs to have replaced all other lighting technologies completely. Having started out as an expensive alternative to incandescent and compact fluorescent lamps, LED based lighting is now among the most cost effective lighting solutions for consumer and professional applications.

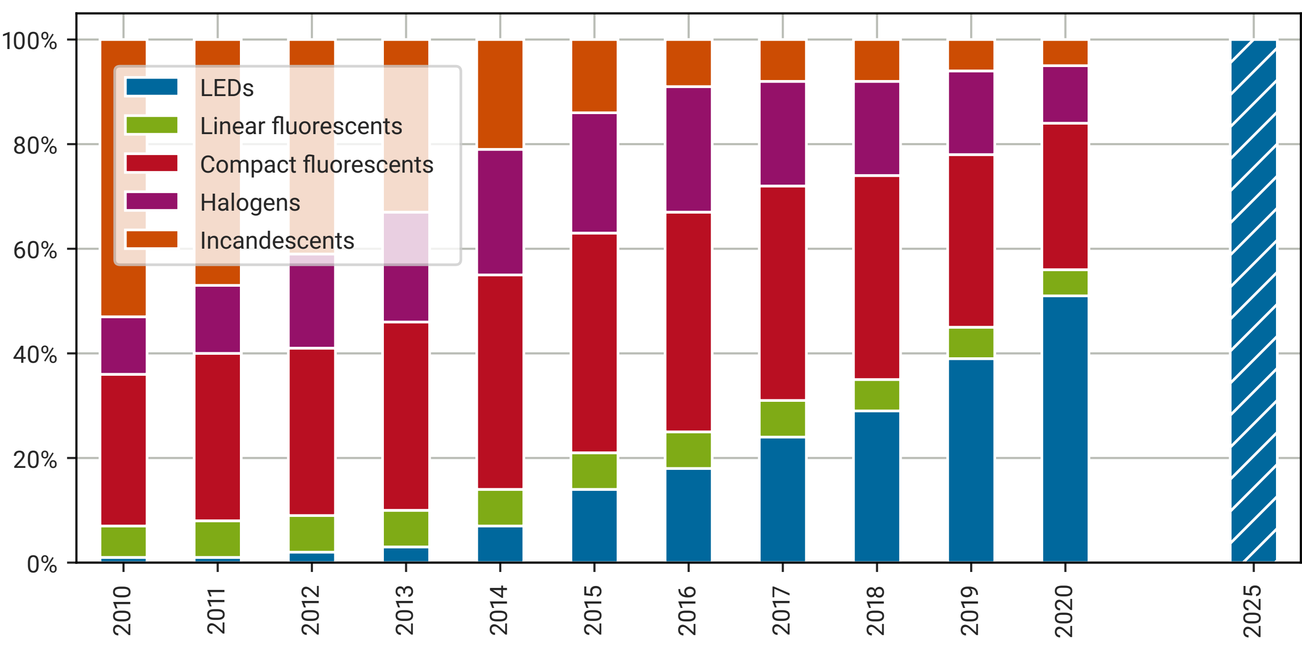

Figure 1.1: Global lighting sales by technology. It is evident that the market share of the LED based luminaires has increased exponentially over the shown ten year interval. The prognosis for 2025 has been drawn hatched to indicate the associated uncertainty. Adapted from [71].

Modern LEDs convert more electrical energy to light than all other lighting technologies. Replacing old luminaires with LED based ones is thought to lead to substantial energy savings and in turn to reduced carbon emissions. Besides its operational energy use, a life cycle assessment of an LED based luminaire will also have to include the energy expended during the manufacturing of the device. The longer the lifetime of the luminaire, the less weight this energy input will carry. Luckily modern LED luminaires are supposed to last for several 10 000 h, with the best being specified to last for up to 100 000 h. Yet, there have been cases of these luminaires failing prematurely. Failures of LED equipped street lights have been reported in Kaarst,

Germany [105], and in the United States of America (USA) in Santa Fe, NM [86], Berkeley, CA [100] and Detroit, MI [12]. Unsurprisingly, these failures make the news as they affect a safety critical installation (street lights) and are obvious to the general population. These are also very expensive failures, as each and every luminaire needs to be replaced by a technician with a service lift. LED lights can also fail in a domestic environment. Although no public statistics exists that aggregates these failures many consumers have experienced one personally.

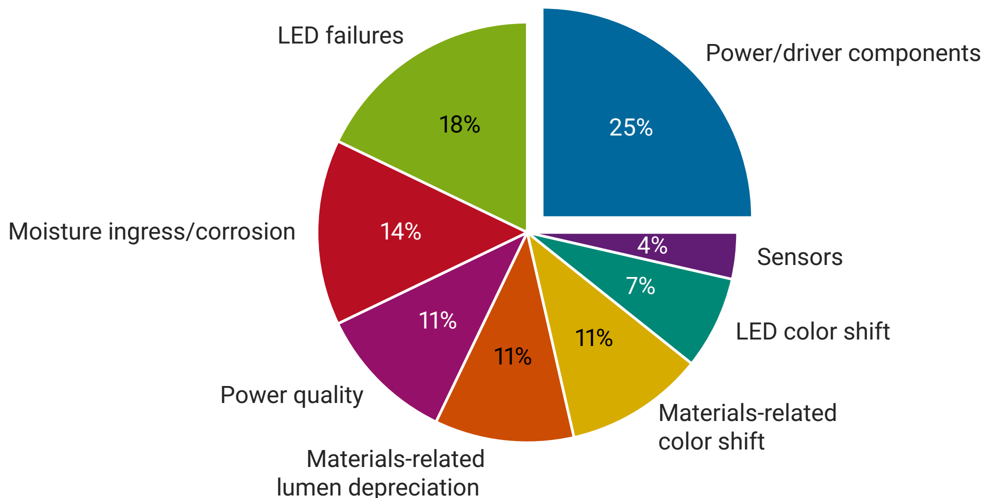

(a) Most commonly observed failure modes from an industry survey.

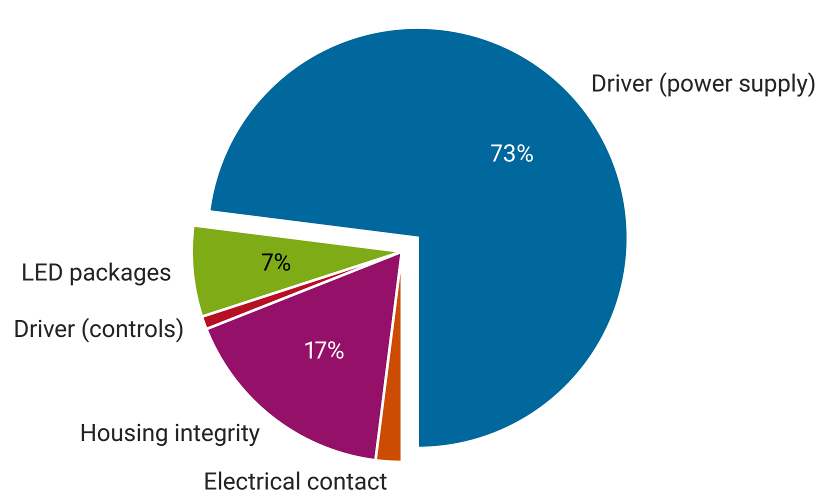

(b) SSL luminaire failure modes from field failures.

Figure 1.2: Two pie charts showing which failure modes are most common in LED based luminaires. Adapted from [88].

If an off-line LED based luminaire fails, the driver is most likely the culprit. A survey among lighting industry professionals as well as a study of actual field failures presented in Figure 1.2 back up this claim. It is therefore worthwhile to look at the drivers in more detail and try to find out what causes them to fail and how long they actually last. Although there are previous publications, like the ones by Catelani and Ciani [10] and Vuorela and Tuominen [123], it was the group around J. Lynn Davis that has published the most comprehensive body

of research on this matter so far [64, 67, 27, 66, 108, 25, 65, 29, 65, 24, 26, 28]. Their 2017 report [24] offers a detailed insight into possible failure modes of LED drivers subjected to accelerated testing. However, only three driver types were included in that study and a lifetime extrapolation was only done for one.

Many questions about the failure modes and lifetime of off-line LED drivers still remain to be answered. This work fills this gap through an experimental study. Three main questions were chosen as its guard posts.

When do off-line LED drivers fail? Here *when* does not refer to a specific point in time but rather the time if takes until a driver fails given certain environmental conditions. These conditions encompass the ambient temperature and relative humidity.

Why do off-line LED drivers fail? This means asking what are the external and intrinsic properties that make a driver more prone to failure. Examples would be operation at an elevated temperature or certain design, component or material choices for the driver's circuit assembly.

How do off-line LED drivers fail? This requires identifying the root failure cause through forensic analysis. It reveals which components are susceptible to failure and thus should be the focus of future efforts to make drivers more robust.

This work presents the results of a broad accelerated lifetime study and subjects them to a thorough analysis. A selection of off-line LED drivers, encompassing 25 different driver types, is tested. A grand total of 75 devices are put to the test in four different environmental conditions. All failed devices are examined and, where possible, the root failure cause is identified. The study is conducted as part of the project *PQL II* [118] which was awarded a grant by the German Federal Ministry of Economic Affairs and Energy[1]. The drivers that are included in the study were gratefully supplied by the luminaire manufacturers that participated in that project.

The term accelerated lifetime test implies that this kind of experiment delivers results in a short amount of time. However, this short amount of time has to be seen in comparison to the time a specimen would last under normal operating conditions. As modern off-line LED drivers are designed to last up to 100 000 h they can endure the conditions of an accelerated test for many thousand hours. The experimental effort to test a significant number of drivers until they fail is therefore enormous. The total test time[2] of the study of approximately 410 000 h illustrates this.

1.1 What Are LED Drivers and How Do They Work

Before the intricacies of accelerated lifetime testing can be discussed the subject of this study has to be introduced, the off-line LED driver. The following paragraphs will lay out what the driver's task is in an SSL system or luminaire and give a short description of its operating principle.

Light-emitting diodes (LEDs) light up when a current flows through them. In electrical terms they behave like diodes, meaning that their voltage-current relationship is exponential in nature. Thus, once the forward voltage of an LED is surpassed the current through it starts to increase rapidly. Together with the fact that the amount of light an LED emits is related to the current flowing through it by an almost linear relationship, it becomes obvious why they are usually supplied by a constant current rather than a voltage source.

The circuit supplying this constant current for the LED is called a driver. The driver itself is usually supplied

[1]This IGF Project of the ZVEI was supported via AiF within the programme for promoting the Industrial Collective Research (IGF) of the Federal Ministry of Economic Affairs and Energy (BMWi), based on a resolution of the German Parliament.

[2]Total test time is defined as the sum of the test times for all devices. A device is removed from the test if it fails or the test is terminated.

by a voltage source and includes some kind of regulation to generate a controlled and constant current. In the context of this work the driver is connected to 230 V line voltage and can therefore be referred to as an *off-line* LED driver. This type of driver can be found in all kinds of lighting equipment, from offices to industrial lighting and even street lights.

Most off-line LED drivers are based on a switched-mode power supply (SMPS) architecture. This type of power supply can operate at a very high efficiency when converting the line voltage to the constant current required by one or a series string of LEDs. An efficiency of 80 % or more is quite common for modern LED drivers, with values exceeding 90 % being possible with the most recent designs and under specific operating conditions. Modern drivers also come in a wide variety of configurations. For some the output current can be programmed either through a digital interface or via an external resistor. Drivers for complex lighting installations like those in office buildings regularly feature a communication interface like for example the digital adressable lighting interface (DALI).

Table 1.1: Comparison of the three most commonly used SMPS topologies.

Buck converter	Boost converter	Flyback converter
V_{in} V_{out}	V_{in} V_{out}	V_{in} V_{out}
Output voltage has to be *lower* than the input voltage. Needs only a simple inductor. No galvanic isolation between input and output.	Output voltage has to be *higher* than the input voltage. Needs only a simple inductor. No galvanic isolation between input and output.	Output voltage can be higher or lower than the input. Needs a coupled inductor which is a relatively expensive component. Requires additional circuitry (e.g. optocoupler) to sense the output voltage or current. Offers galvanic isolation between input and output.

Switched mode power supplies can be built around a multitude of available topologies. The three most common topologies are the buck converter, boost converter and flyback converter. Their properties are listed in Table 1.1 together with a simplified schematic[3]. Some drivers employ a two stage topology, where the first stage is called the PFC stage. Its control loop is setup in a way that the current it draws for mains is in phase with the power line voltage. This ensures a high PF to reduce the effect a device has on the power quality on the mains side[4]. The PFC stage usually uses either a boost or flyback converter. It can be followed by either of the three mentioned converter topologies depending on the design requirements. Modern control ICs make it

[3]A detailed description of their mode of operation can be found in the reference work by Billings and Morey [4].
[4]The PF varies between zero and one, with one indicating that the current drawn from the mains is perfectly in phase with the line voltage.

possible to produce single stage drivers with a PF close to one. However, this is still limited to drivers with a maximum output power of less than about 70 W.

1.2 Outline of This Work

The structure of this work follows the traditional pattern of introduction, methods, discussion and conclusion. This structure serves it well as the subject of this work can be looked upon as a classic study. To begin, this chapter serves as a short introduction and presents the motivation for this work.

Chapter 2 introduces the experimental design of the study. First, it gives justification for the choice of environmental conditions used in the accelerated lifetime test. Special focus is on the decision to use damp heat conditions. This is followed by a description of the experimental setup, including the climate chambers used for the tests and the automated measurement system that records important parameters of the specimens during testing. Finally, the analytical approach is presented. This includes the forensic procedure that is used to identify the root failure cause of a device as well as the physical and statistical models that are used to analyze the lifetime data.

Chapter 3 presents the results of the accelerated lifetime tests. After giving an overview of the drivers that have failed, the degradation of the aluminium electrolytic capacitors in the dry heat condition is examined in more detail. The second and most comprehensive part of this chapter contains the failure mode analyses. For every failed device where an analysis is possible the root failure cause and the reasoning that lead to its identification is described.

Chapter 4 starts with the results from fitting the physical accelerated failure time models to the available lifetime data. The lifetime of the drivers in different environmental conditions is calculated through extrapolation. To further an intuitive understanding of the results the lifetime is estimated for a handful of real world locations with different climatic conditions. This is followed by a statistical analysis that applies the Cox PH model. This analysis makes it possible to identify the properties of a driver that influence its reliability. Thus, the chapter is completed by a discussion of what can be done to increase the longevity of future driver designs.

Finally, Chapter 5 summarizes and concludes the results of this work. In an outlook future research activities are identified to gain further insight into the failure mechanisms that have been identified by this work.

2 Methods

When designing an electronic circuit assembly, a designer or team is confronted with a sheer infinite number of possible solutions. Each design decision might influence one or more performance parameters of the finished product, last but not least its reliability. An oversight, like a component that has not been correctly derated for the planned operating conditions, can quickly jeopardize the reliability goals the product was supposed to reach. Quality control measures are introduced to identify these problems before the product reaches the customer. However, it is in testing where the proverbial rubber finally hits the road.

As stated earlier, a series of accelerated lifetime testing experiments have been conducted for this work. This chapter presents the experimental design and the analytical approach. The first sections introduce the experimental setup, both in terms of the equipment that was put to use as well as the software that was written to automate the testing. This is followed by the forensic failure mode analysis approach that all failed specimen were subjected to. Finally, the models used to extrapolate the lifetime of a driver from the accelerated lifetime test data and two statistical methods to compare the results of groups of driver with another are introduced.

2.1 Central Requirements for the Test Setup

Although the degradation of the devices under test is accelerated substantially, the tests are still expected to last for several thousand hours. The experimental setup is designed with these very long test durations in mind. Thus, the following three central requirements are established for the test setup:

- control of the environmental conditions must include relative humidity,
- monitoring of all parameters must run automated and unattended and
- the test setup must be highly reliable so that it will not interfere with the experiments.

The following sections present these requirements in more details and outline how they are met.

2.1.1 Test Using Damp Heat

It is commonly agreed upon that elevated temperatures can accelerate the degradation of most electronic devices and systems [63]. As very long lifetimes and high reliability are expected from LED drivers, they are designed and qualified to survive harsh environmental conditions such as high temperatures. Figure 2.1, reproduced from the data-sheet of the driver LG LLP 150W 0.7A 125 280Vdc PISE-A150D shows its lifetime for temperatures from 20 °C to 80 °C. At a case temperature of 80 °C it is specified to last 50 000 h or over six years of continuous operation, which vastly exceeds the time available for a project like this. However, to gather trustworthy results the test conditions should stay as close as possible to the planned operating

conditions [87]. Although many other driver's data sheets do not contain graphs plotting the expected lifetime versus ambient temperature they are similarly robust.

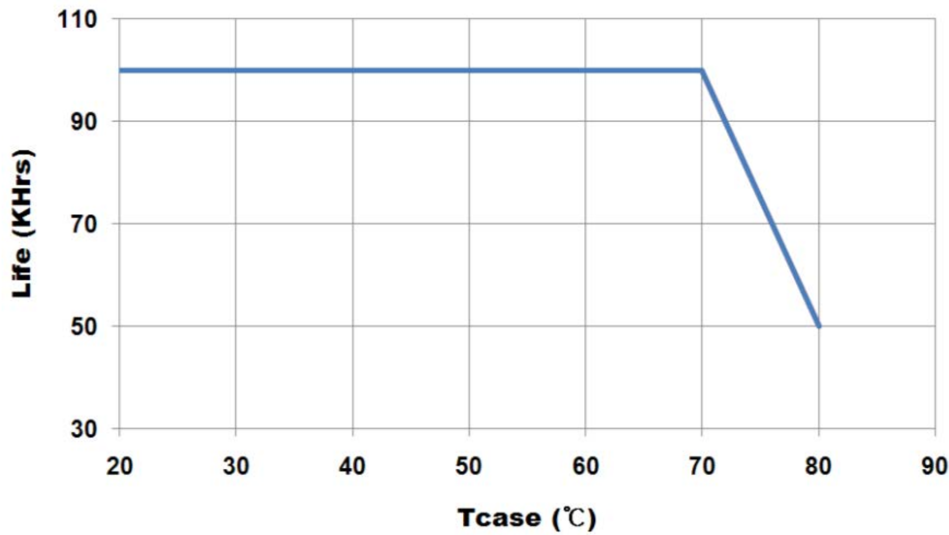

Figure 2.1: Lifetime of an LED driver vs. case temperature as specified by the manufacturer [97].

An additional stress is hence necessary to induce a sufficient number of failures in a manageable amount of time. The obvious choice is the relative humidity of the environment the device is operated in. In actual operation, devices will encounter a range of relative humidities, including very high levels. This is especially true for devices in outdoor applications. In 1997 a report found that dehumidification could lead to a 20 % increase in reliability for conformally coated, military spec assemblies [132], illustrating the major impact humidity has even on the most robust of designs. Additionally, the availability of established models describing its effect on lifetime enable the extrapolation from accelerated test data. Finally, as its value can be continuously varied over an interval from 0 % to 100 % this extrapolation can be achieved using basic regression methods.

Climate chambers – as opposed to the simpler temperature chambers – are laboratory devices that can create an environment with tight control over its temperature and relative humidity. A wide variety is available in the market. They differ in the range of temperature and humidity they cover as well as in the volume of the actual chamber. Additionally, some offer advanced control like the ability to run complex test sequences or they can be interfaced to a computer. They can also be fitted with access openings, so that wires and other connections can be run between the inside of the chamber and surrounding lab. This is most useful as it allows to keep all supplemental gear outside of the chamber where it can be easily accessed. Only the actual device under test has to be placed inside the chamber where it will have to endure its harsh environmental conditions.

For the experiments two climate chambers made by the Japanese manufacturer ESPEC are used. Their specifications are shown in Table 2.1. These chambers are quite spacious with an inside capacity of 408 l. The DUTs are placed in the chambers while their accompanying LED loads are stored outside. A substantial bundle of cables is required to make the necessary connections back and forth to the DUTs. The wiring diagram and a detailed description can be found in Section 2.3.

Table 2.1: Most important technical specifications of the two climate chambers used for the tests [99, 98].

Model	PL-3K	PR-3J
Inside Capacity	408 l	
Temperature range	−40 °C to +100 °C	−20 °C to +150 °C
Temperature fluctuation	±0.3 °C	
Temperature heat-up rate	$3.1\,°C\,min^{-1}$	$3.0\,°C\,min^{-1}$
Temperature pull-down range	$1.2\,°C\,min^{-1}$	$1.5\,°C\,min^{-1}$
Humidity range	20 % to 98 %	
Humidity fluctuation	±2.5 %	

2.1.2 Automated Monitoring of the Required Parameters

Overseeing an accelerated lifetime experiment includes routine maintenance on the laboratory equipment as well as constant monitoring of the devices under test. If the number of devices under test is increased and important parameters have to be checked more frequently, this becomes an overwhelming amount of work. Luckily, at least the measurement tasks can be automated.

One major benefit of automation are repeatable measurements at equal time intervals. The frequency of those measurements is then essentially only limited by the capabilities of the available test and measurement equipment. Further extending the automation to the evaluation and presentation of the acquired data lets the experimenter keep an eye on the progression of the test and intervene if undesirable behaviour is identified.

Finally, using automated monitoring with its frequent measurements the time-of-failure can be determined more accurately.

2.1.3 Reliable Test Setup

Having a reliable test setup might seem like an obvious requirement, but it still presents a significant challenge to the reliability engineer: the test setup needs to be more reliable than the device under test. Otherwise, there will be gaps in the data or - even worse - the test will come to an early end due to equipment failure[1]. As a consequence the monitoring setup – while it is not subjected to the accelerating stresses – has to work reliably over several test runs stretching over many thousand hours. The parts of the system that have to be inside the climate chambers must be so robust enough to outlast the devices under test they are connected to. This has to be taken into account for the design of the test setup.

The fact that the system is supposed to be used for repeated test runs leads into another requirement: as experience with the setup and the experiment grows, it will become desirable to make changes to the system and improve it. The design has to account for this in being modular and accessible.

[1]This actually happened in the experiments for this work: after several thousand hours one of the climate chambers failed, abruptly ending the fifth accelerated test run. Unfortunately, the cooling circuit had developed a leak that allowed humidity to enter the system. The chamber had to be scrapped.

Table 2.2: List of the test equipment used in the experimental setup.

	Model	Measured parameter	Interface	Comment
Multiplexer and Switch Unit	HP 3488A	none	GPIB	equipped with a combination of five multiplexer, matrix switch and/or relay modules
Oscilloscope	Tektronix TDS2001C	output current	USB	
Power Analyser	Tektronix PA1000	mains side (power, ...)	Ethernet	
Data Acquisition Switch Unit	Agilent 34970A	temperature at t_C point	GPIB	equipped with two 20-channel multiplexer modules

2.2 Selection of the Drivers for the Test

The drivers that were subjected to accelerated lifetime testing were gratefully provided by the luminaire manufacturers that participated in the *PQL II* project. They were free to decide which drivers to test based on internal criteria. The selection of drivers that has been provided covers a wide range of different types. It includes drivers for office and outdoor applications and those with or without a communication interface. Their maximum output power covers a range from about 30 to 170 W. The manufacturers also categorized the provided drivers as either *high-end* or *low-cost* to enable a comparison between these two groups. A detailed overview of the tested drivers can be found in Chapter 4 in Table 4.3.

2.3 Experimental Setup

As outlined above, the experimental setup should allow the constant monitoring of important parameters of the DUTs while being highly reliable at the same time. A methodic approach was chosen to ensure the resulting system would be able to pass these requirements. In a first step the parameters that would need to be monitored are determined. On the mains side the current draw of the DUT is an obvious choice. Add to that the real and apparent power the device consumes and the PF can be calculated as well. This parameter might give some indication of the degradation of components on the mains side of the circuit. The same is true for the current THD, as the degradation of some components might give rise to non-linear effects in the circuit.

Monitoring of the DUT itself should definitely include the temperature of the device. Commercial LED drivers usually bear a mark indicating the point where the highest acceptable temperature on its case surface should be measured [68, s. 3.16]. This is commonly know as the t_C point. As all drivers tested for this work bear this marking, the DUT's temperature is measured at this point using a type K thermocouple.

On the output side of the LED drivers only the current flowing through the LEDs is monitored. This decision is based on literature research indicating that the degradation of aluminium electrolytic capacitors being the most important failure mode for SMPS in general as well as LED drivers in particular [73, 43]. As their degradation causes an increase in the ripple superimposed on the constant output current this parameter is recorded as well.

To guarantee high reliability and availability of the test setup, commercial off-the-shelf (COTS) test equipment was used wherever possible. Table 2.2 lists the equipment that is used for the setup. A central component of the installation are the four HP 3488A multiplexer and switch units. They facilitate the switching between the 30 different DUTs spread over the two climate chambers. As the power analyser and oscilloscope offer only a single input these have to be multiplexed between the DUTs. The HP 3488A can carry up to five different modules enabling a variety of multiplexing tasks. Having been introduced over thirty years ago these devices can be acquired for quite reasonable prices. In this setup the 44472A dual one-by-four very high frequency (VHF) multiplexer was used in a staggered configuration to switch the oscilloscope's input to the appropriate output current measurement unit. 44473A matrix switch modules were used to do the same for the current input of the power analyser. Several 44471A general purpose relay modules were used for various tasks like controlling the relays switching the DUT's main supplies.

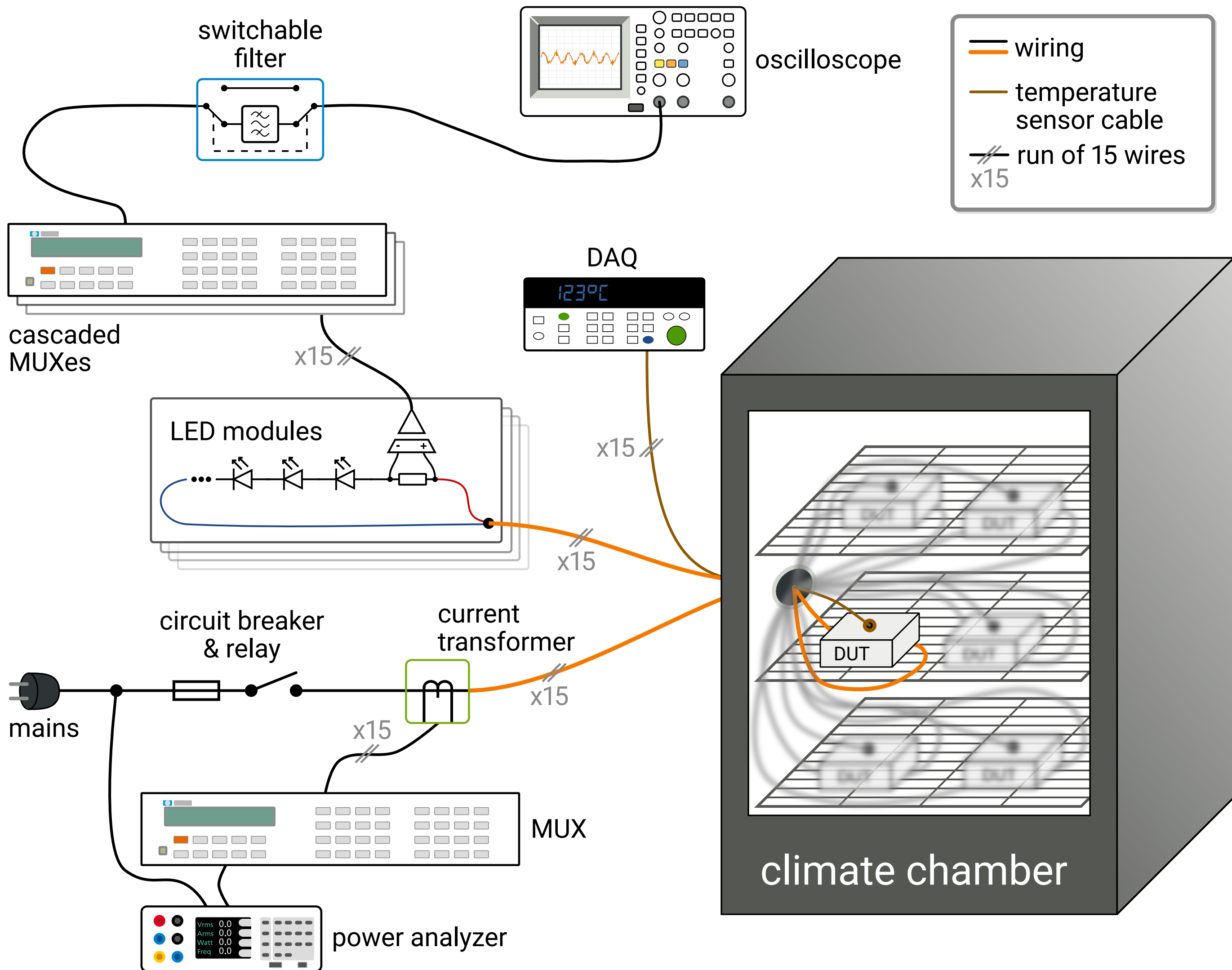

Figure 2.2: Schematic diagram showing the equipment used in the experiments as well as the wiring between the DUTs and the test gear. Each chamber has a capacity of up to 15 drivers, however for illustrative purposes the wiring for only one driver is shown.

A simplified wiring diagram of the test setup is presented in Figure 2.2. The wiring is repeated for the second climate chamber. It shows how the DUTs are placed in the chamber and hooked up to their corresponding LED modules. Between the driver and the LED module a galvanically isolated current transducer is inserted. This module consists of a shunt resistor and an isolated differential amplifier. This signal is then routed to a cascade of multiplexers (MUXes) that route the selected one to the switchable filter. This filter makes it possible to measure the high frequency ripple signal on the output current with the oscilloscope which for some driver would otherwise be drowned by low frequency ripple. All connections are carried out with 50 Ω-terminated coaxial cables to preserve the integrity of the current waveform. This includes the filter circuit.

The temperature sensors are placed on the t_C point of the case of the driver as discussed above. The wires from these type K thermocouples are directly connected to a multiplexer card inside the Agilent 34970 data acquisition unit (DAQ). This piece of test equipment combines a 6 1/2-digit multimeter with three slots that can carry different kinds of multiplexer modules, making it an all-in-one solution alleviating the need for a separate multiplexer.

The final piece of measurement equipment completing the trio is the power analyser. It has to sample the input voltage and current of each DUT. Selecting the correct input for each DUT is again achieved with HP 3488A units. The current measurement is galvanically isolated using a current transformer. The Tektronix PA1000 power analyser can factor in the current ratio of the transformer in its calculations if setup correctly. As the drivers in the two climate chambers are hooked up to two different phases of the three-phase mains the voltage of both has to be tapped. This is done with a resistor divider as to limit the voltages at the MUX to safe levels. However, this part of the circuit is not shown in Figure 2.2.

The power distribution circuit is equipped with a separate relay and 10 A circuit breaker for each DUT. An electrical failure of one device therefore does not trigger the 16 A circuit breaker in the central power distribution cabinet. Also, each device can be power cycled programmatically, enabling the use of power cycles in a test regimen.

2.3.1 Selection of the Environmental Conditions

Selecting the environmental conditions for an accelerated lifetime test is a delicate matter. These conditions determine the level of stress the DUTs are subjected to and therefore how long they are going to survive the test. If a physical model (see Section 2.6) is to be used to extrapolate the lifetime of a device after a series of tests at different stresses, the choice of environmental conditions will influence the accuracy of this estimation as well [87, 317ff]. A variety of approaches have been developed to plan an experiment so that the variance of the estimated models will be minimized. Unfortunately, test planning requires a priori knowledge about the outcome of the experiment to give a model-based estimation of the likely results.

As the necessary information about the behaviour of LED drivers in accelerated lifetime test is not available, a statistical test planning approach cannot be considered for this work. To enable comparison of the achieved results with information commonly published by electronic device and system manufacturers and researchers, 85 °C at a relative humidity of 85 % is selected as the first environmental condition to be tested. This temperature and humidity combination is one the most widely used environmental conditions and has been adopted into a variety of standards [112, 113, 33].

In 2017 Davis published the most extensive results of accelerated lifetime testing experiments of LED drivers so far [24]. In their work they chose three environmental conditions, namely 85 °C/85 %, 75 °C/75 % and 65 °C/90 %. As Davis successfully demonstrated the fitting of a lifetime model from their data, it is concluded that the selected stress levels would be appropriate for this work as well.

Previous publications suggests that the degradation of aluminium electrolytic capacitors is among the most common failure modes for LED drivers [43]. The degradation of these capacitors is caused by the evaporation of the liquid electrolyte [125] and thus is accelerated at elevated temperatures. To put this to the test an experiment in dry heat[2] at 85 °C is included in the series of experiments. This brings the total number of environmental conditions for this work to four: dry heat at 85 °C and damp heat at 65 °C/90 %, 75 °C/75 % and 85 °C/85 %.

2.4 Test Automation

As stated in Section 2.1, automating the test setup reaps immense benefits. The illustration in Figure 2.3 backs up this argument. The experiments for this work ran over several years. The DUTs should be monitored at least once a week and that task can be estimated to take approximately one full day for 30 devices. Just taking into account the amount of time saved by not having to do these measurements manually one could invest over two months before break-even, according to Figure 2.3. The higher reliability of an automated solution due to the reduced risk of human error is another benefit.

HOW LONG CAN YOU WORK ON MAKING A ROUTINE TASK MORE EFFICIENT BEFORE YOU'RE SPENDING MORE TIME THAN YOU SAVE?
(ACROSS FIVE YEARS)

HOW MUCH TIME YOU SHAVE OFF	HOW OFTEN YOU DO THE TASK					
	50/DAY	5/DAY	DAILY	WEEKLY	MONTHLY	YEARLY
1 SECOND	1 DAY	2 HOURS	30 MINUTES	4 MINUTES	1 MINUTE	5 SECONDS
5 SECONDS	5 DAYS	12 HOURS	2 HOURS	21 MINUTES	5 MINUTES	25 SECONDS
30 SECONDS	4 WEEKS	3 DAYS	12 HOURS	2 HOURS	30 MINUTES	2 MINUTES
1 MINUTE	8 WEEKS	6 DAYS	1 DAY	4 HOURS	1 HOUR	5 MINUTES
5 MINUTES	9 MONTHS	4 WEEKS	6 DAYS	21 HOURS	5 HOURS	25 MINUTES
30 MINUTES		6 MONTHS	5 WEEKS	5 DAYS	1 DAY	2 HOURS
1 HOUR		10 MONTHS	2 MONTHS	10 DAYS	2 DAYS	5 HOURS
6 HOURS				2 MONTHS	2 WEEKS	1 DAY
1 DAY					8 WEEKS	5 DAYS

Figure 2.3: Trade-off between time invested to make a task more efficient and actual time saved presented in matrix form [49].[3]

The programming language Python is chosen as the main language for the automation of the test setup. Python's ecosystem offers a broad range of libraries, drastically reducing the amount of effort to build complex software systems. It is also commonly used for data analysis as it offers very powerful tools for the import, manipulation, statistical analysis and presentation of data. This makes it possible to do almost all jobs

[2]For a *dry heat* condition the humidifier of the climate chamber is disabled. An active removal of the humidity inside the chamber is not necessary, as the relative humidity of the lab air is below 2 % once heated up to 85 °C.
[3]Created by Randall Munroe for the XKCD webcomic. Licensed under CC BY-NC 2.5.

surrounding the tests, from the acquisition of the data to generating plots for works like this, without leaving the familiar Python environment.

Another major component used for the test automation is the VISA library [89] made by NI (formerly National Instruments). This library serves as a common interface to test equipment, enabling access to the devices no matter how they are connected to the PC. The PyVISA [116] library makes its application programming interface (API) accessible from Python. Figure 2.4 outlines the architecture of the software setup from test automation to analysis.

The VISA library sits between the test equipment and the `test-runner.py` application. The application reads a test definition from a database. The test definition consists of a Python file defining a sequence of measurements as well as a JavaScript object notation (JSON) file containing the settings for the test gear. The application orchestrates the execution of the measurements, retrieves their results and stores them as files in the file system. Features of the underlying Linux operating system (OS) are used to start the application in regular intervals. The system is highly modular and can be easily adapted to different test scenarios. It is made up of approximately 3800 lines of Python code, with the biggest part being the drivers to control the different pieces of test equipment. Over the course of the experiments the test configuration database has grown to more than 20 000 lines of JSON and over 400 lines of Python code.

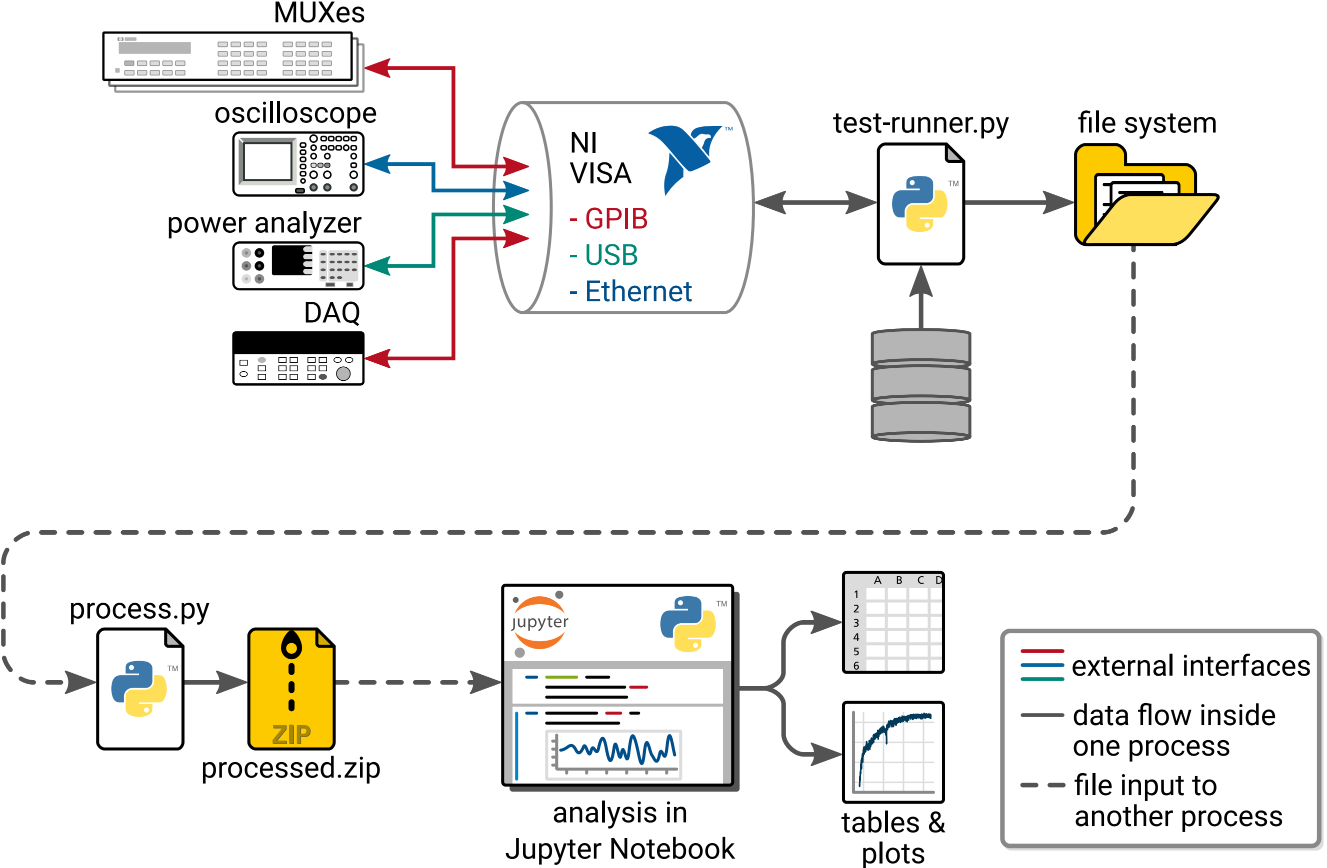

Figure 2.4: Flow chart illustrating how the applications for test automation, data processing and analysis work together and interact with the test equipment. The directory or file icon indicate that output is stored in files for later processing.

As highlighted by Figure 2.4, once the measurement results have been stored in the file system a second application takes over. This application is called `process.py` and it preprocesses the data for easier analysis. This is most important for the results from the oscilloscope, as the frequency and amplitude of the output current ripple can not be directly determined from the raw samples the test equipment returns. As this processing step is computationally expensive, it is advantageous to do it in advance to enable quick access and analysis of the data later on.

Finally, the considerable data sets produced by the automated test setup have to be evaluated. This is done in the Jupyter notebook environment [3], an interactive, browser-based tool for exploratory data analysis. The programming language of choice is once again Python. The most important tools used analysing the data are the pandas library [102] for data handling, SciPy [122] to apply non-linear regression and statistical tests and Matplotlib [47] to create graphical representations and plots. These tools have most definitely proven themselves in the preparation of this work. It is no surprise then, that they are also very popular in the emerging field of data science.

2.5 Failure Mode Analysis

Once the automated monitoring has detected a failure a forensic failure mode analysis must be undertaken to investigate what has caused the device to fail. The chosen approach has been adapted from a report by Davis et al. [24, p. 4-207]. The flow chart in Figure 2.5 gives a graphical representation of the process. The obvious first step is the detection of a failure or *lights out* event. This requires periodic examination of the DUTs and their LED loads. If a DUT's LED load goes dark and can not be brought back by power cycling, the device is considered to have failed. The precise time of failure is then determined by looking at the recorded input power draw. The moment where it falls to zero is assigned to be the time of failure.

In a next step – if possible – the device's case is removed for a visual inspection. All signs of damage, be it discolouration of the PCB material or components, charred or burned areas on the PCB, cracks in IC packages or corrosion on tracks or components are recorded. If an obvious or catastrophic damage is detected the inspection can be stopped here.

Some of the tested drivers are potted using a bitumen-like substance. As this substance is very sticky and viscous even when heated, it has been all but impossible to remove it. Research has indicated that dry-ice blasting might be capable to remove this type of potting. However, it was not considered for this work, as this method is only offered by a few specialized companies and is also quite costly due to the blasting medium.

Following the visual inspection a broad range of components is inspected using the continuity check mode of a multimeter. This allows the detection of short or open circuit failures. The components are transformers and inductors, power transistors, diodes and of course the input protection fuse. Again, all findings are recorded for later evaluation.

Finally, if a failure cause cannot be determined in the previous steps, a detailed analysis is conducted. The approach of this analysis has to be tailored to the specific device based on the earlier findings and its circuit topology. The measures included checking of certain voltages in the circuit (e.g. at the PFC capacitor) under bias, thermal imaging of the powered circuit and removal of components to examine them out of the circuit.

The failure mode analysis has been successful in the majority of cases. The detailed results are be presented in Section 3.2.

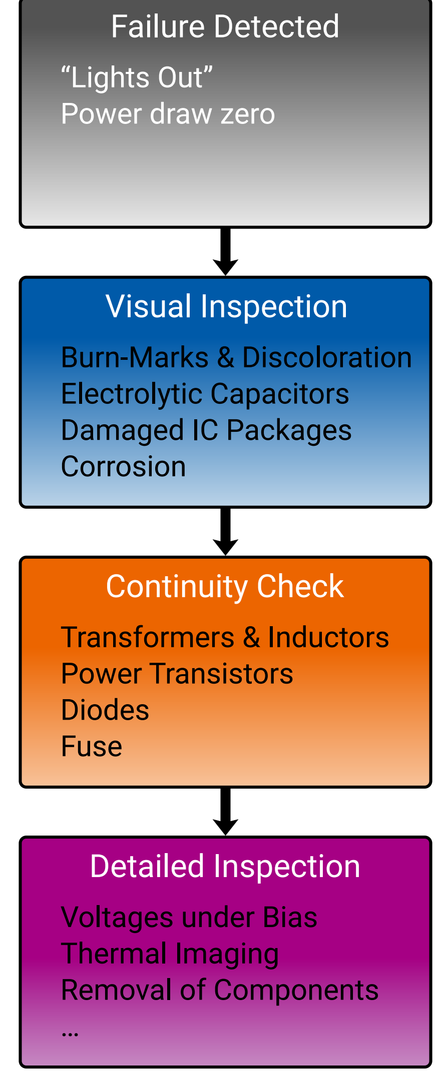

Figure 2.5: Flow chart illustrating the chosen failure mode analysis approach. Based on [24, p. 4-207].

2.6 Physical Models for Life Tests with Constant Stress

Physical models are required to establish a relationship between the accelerating variables or stresses of a life test (e.g. temperature, humidity, voltage) and the lifetime of a tested specimen. If a sufficient number of data points is at hand the model's parameters can be estimated. The fitted model can then be used to estimate the lifetime of the specimen at a different combination of accelerating variables or stress. This approach is used extensively in accelerated life testing, where devices are exposed to high stress levels to drastically shorten their lifetime. The resulting lifetimes at different stresses are then used to fit a model and extrapolate a value at the lower stress at which the device is expected to be operated in.

In the context of this work *physical* models associate *physical* variables like temperature or relative humidity with an acceleration factor. They are however not necessarily based on a physical understanding of the underlying failure mechanism. They should rather be looked upon as empirical models being fit to an existing data set. The confidence that the model correctly describes the effect the accelerating stresses have on the

lifetime of the specimen therefore has to be motivated by the data rather than by trust in the model itself.

The lifetime is not the same even for devices tested under the same conditions, but scatters and can be described by a statistical distribution. Hence, the result of a model gives the *nominal* lifetime which is the mean, median or other percentile of the lifetime, depending of the underlying distribution.

Two models are selected for this work: the Peck model, proposed by Peck in 1986, and the Intel model. The name of the latter follows the nomenclature found in [87].

Both models are based on the earlier work of Arrhenius. In his 1889 work Arrhenius proposed an equation to model the effect temperature has on the rate of chemical reactions. The *Arrhenius law* is defined as

$$k = A\,\exp(\frac{E_A}{k_B T}), \tag{2.1}$$

with k being the reaction rate, A a constant factor, the absolute temperature T, Boltzmann's constant k_B and finally the activation energy E_A of the reaction. Due to its simple form and decent fitting results this equation has found widespread application in engineering. Although the model has been attributed to describe chemical kinetics very well [15, p. 188], its haphazard application to a vast array of failure modes has been criticised [90, 63, pp. 2–8]. It is the reliability engineer's obligation to take appropriate care when applying this model and interpreting its results.

Peck came up with an extension to the Arrhenius law when doing a meta analysis of published data of the failure of epoxy packages tested in an 85 °C/85 % environment [95]. The failures were almost exclusively caused by electrolytic corrosion of the aluminium metallization on the semiconductor die inside the packages. The model is given by the equation

$$\tau = A\,(RH)^{-n}\,\exp(\frac{E_A}{k_B T}), \tag{2.2}$$

where τ is the nominal lifetime and n a parameter defining the size of the effect the relative humidity RH has on the lifetime. The remainder of the equation is just the Arrhenius law as in Equation (2.1).

The second model used in this work is an extension of a model describing the rate of chemical reactions proposed in 1935 by both Eyring and Evans and Polanyi. It is commonly called the Eyring model and enables the inclusion of any number of stressors, but commonly includes temperature. Intel Corporation extended this model to describe the effect temperature and relative humidity had on the corrosion of the on-die metallization in plastic packages. The model can be written as

$$\tau = A\,\exp(-B \cdot RH)\,\exp(\frac{E_A}{k_B T}), \tag{2.3}$$

where B is a parameter determining the effect the relative humidity RH has on the nominal lifetime τ of a device. The right side of the equation is once more the Arrhenius law as presented in Equation (2.1).

Both models can be fit for devices where failures have been observed at three or more different environmental conditions and the lifetimes have been recorded. The model parameters can then be estimated using non-linear curve fitting based on the least-squares method. As stated earlier, the lifetimes of devices scatter and can be described using an appropriate statistical distribution. Popular choices are the log-normal distribution or the more flexible Weibull distribution. The parameters of a compound model consisting of a physical model and a chosen distribution can be determined using maximum-likelihood estimation. However, this requires that multiple failures have been recorded at each environmental condition. Due to experimental limitations and

devices not failing in the allotted test time, this is not the case for the experiments conducted for this work. A detailed treatise on how to deal with compound models can be found in [87].

Once a model has been fitted to a dataset the question arises how well that model explains the data. This can be quantified by calculating a goodness-of-fit metric. Given that a least-squares regression approach is used to fit the data, the coefficient of determination or R^2 is the obvious choice. The interpretation of this metric is straightforward, with a value of one indicating a perfect fit and zero no correlation at all. Given that each driver is tested at no more than three environmental conditions and the models have only three parameters that need to be fitted, a perfect fit is what is expected. The coefficient of determination is defined as

$$R^2 = 1 - \frac{\sum (y - \hat{y})^2}{\sum (y - \bar{y})^2}, \tag{2.4}$$

where y denotes the data, $\bar{y}$ the data's mean and $\hat{y}$ the model's estimation. The numerator of the fraction is also called the sum of squares of residuals and is the value that the least-squares regression is trying to minimize. Dividing it by what is called the total sum of squares and subtracting the result from one normalizes the value to an interval between -1 and 1[4], greatly aiding in its interpretation.

2.7 Survival Analysis

Survival analysis is a field of statistics dealing with time-to-event data. The event can be a failure of a technical device or the death of a patient under treatment. It gets its name from the fact that in many cases the event marks the end of life of the observed subject. Its methods find widespread application in the analysis of medical or biological studies, however, they are also used in engineering, economics and sociology.

As many of the methods that are now regarded to be part of survival analysis have been developed with medical studies in mind, they are often capable of dealing with censored data. Of the different kinds of censoring that have been defined only right censoring plays a role in the context of this work. Right censored time-to-event data points are those where it is known that the subject has survived until a certain point in time, but not what happened after that. These data points result from an experiment that has been terminated before all subjects reached the end of their lifetime or because subject has been excluded from the experiment for reasons that are not considered to be the sought after event. An common example from the field of engineering is that an experiment has to be terminated as the lab capacity is required for another study.

In the following sections two methods will be presented: the Kaplan-Meier method and the Cox proportional hazards model. Both can handle right censored data and can be used to evaluate the results of a comparative study by estimating the corresponding survival functions for each class of subjects included in the study. The survival function $\hat{S}(t)$ gives the probability of a subject to survive past a given point in time.

2.7.1 Kaplan-Meier Method

The Kaplan-Meier method [54] calculates an estimate of the survival function of a population from a sample. It does so without assuming a survival distribution and therefore is a non-parametric method. Named after Edward L. Kaplan and Paul Meier, it requires less ex ante knowledge about the random process generating

[4]An R^2 value of -1 indicates that the model fits the data perfectly but its slope has to be inverted.

the data than e.g. compound models that were mentioned in Section 2.6. It also deals gracefully with right censored data.

To apply the model the time when a subject has been removed from the study has to be recorded as well as whether this was due to the expected event or censoring. This results in a dataset where for a time point $t_{(i)}$ the number of subjects remaining at risk is n_i and the number of failures is m_i. The Kaplan-Meier estimator for the survival function can then be written in product limit form

$$\hat{S}(t) = \prod_{t_{(i)} \leq t} \frac{n_i - m_i}{n_i}. \tag{2.5}$$

To factor in the censored data points they are subtracted from the number of subjects remaining at risk at the time point where they were removed from the study. This is hardly surprising, as these subjects are not *under risk* any longer once they have left the study.

In a comparative study design, the log-rank testing can be used to check whether the difference between two estimated survival functions is statistically significant. The calculation of the test statistic is presented in the following. There exists a wide variety of equations to calculate this statistic. These equations are mathematically identical, however, this is often not immediately obvious. The form presented below can be found in the book by Kleinbaum and Klein [58, pp. 67–71]. Its only difference to the calculation presented in the original paper by Mantel [79][5] is the omission of the *continuity correction* as proposed by Yates [134]. This correction factor has come under considerable scrutiny over the years [16, 81], which is why it is not used in the more recent equations presented by Kleinbaum and Klein.

To check whether the survival function of two groups are different a test statistic can be calculated. The two groups are defined by the number of subjects remaining at risk $n_{1,i}$ and $n_{2,i}$ and the number of failures $m_{1,i}$ and $m_{2,i}$. First the numbers of expected failures for both groups are calculated using

$$e_{1,i} = \left(\frac{n_{1,i}}{n_{1,i} + n_{2,i}}\right) \times \left(m_{1,i} + m_{2,i}\right) \text{ and} \tag{2.6}$$

$$e_{2,i} = \left(\frac{n_{2,i}}{n_{1,i} + n_{2,i}}\right) \times \left(m_{1,i} + m_{2,i}\right). \tag{2.7}$$

To calculate the test statistic for the log-rank test, the sum of observed minus expected failures over all time points $t_{(i)}$ as well as its variance have to be calculated for either group j using

$$O_j - E_j = \sum_{t_{(i)} \leq t} \left(m_{j,i} - e_{j,i}\right) \text{ and} \tag{2.8}$$

$$\text{Var}\left(O_j - E_j\right) = \sum_{t_{(i)} \leq t t_{(i)} \leq t} \frac{n_{1,i} n_{2,i} \left(m_{1,i} + m_{2,i}\right) \left(n_{1,i} + n_{2,i} - m_{1,i} - m_{2,i}\right)}{\left(n_{1,i} + n_{2,i}\right)^2 \left(n_{1,i} + n_{2,i} - 1\right)}. \tag{2.9}$$

Finally, the test statistic can be calculated for either group. For the second group it is given by

$$X^2 = \frac{\left(O_2 - E_2\right)^2}{\text{Var}\left(O_2 - E_2\right)}. \tag{2.10}$$

[4]Curiously, the test has not been named after its inventor. Instead, the name log-rank test was later given to it by Peto and Peto [96].

This statistic is approximately X^2 with one degree of freedom. The corresponding p-value can then be looked up in a table or directly computed using an appropriate software tool. The test can be extended to compare a multitude of groups instead of just two. It is also possible to check the accuracy of the survival function that was estimated with the Kaplan-Meier method function through the calculation of an appropriate confidence interval.

2.7.2 Cox Proportional Hazards Model

The Cox Proportional Hazards model (Cox PH model) is usually given in terms of its hazard function [21, 22]. Its hazard model formula is defined as

$$h(t, \mathbf{X}) = h_0(t)\, e^{\boldsymbol{\beta}\mathbf{X}} = h_0(t)\, e^{\sum_{i=1}^{p} \beta_i X_i}. \tag{2.11}$$

The hazard function gives the risk for a specimen to fail at time t, given that it has survived so far. The relationship between the hazard function $h(t)$ and the survival function $S(t)$ can be expressed by

$$h(t) = -\frac{d}{dt} S(t) \tag{2.12}$$

for continuous distributions [22, p. 14].

The hazard formula of the Cox PH model is a product of two quantities. The first one, $h_0(t)$, is called the *baseline hazard* function. The second is the exponential expression e to $\boldsymbol{\beta}\mathbf{X}$ or $\sum \beta_i X_i$, where $\mathbf{X} = (X_1, X_2, \dots X_p)$ are the p explanatory variables. Its eponymous property is that the baseline hazard does not involve the X's while the explanatory variables are independent of the time t. The resulting hazard is therefore *proportional* to the second quantity which is in turn determined by the explanatory variables. The hazard formula reduces to the baseline hazard if all X's are zero ($\mathbf{X} = \mathbf{0}$) and is thus denoted by a subscript zero.

In contrast to the Kaplan-Meier Method, which is limited to binary comparisons, the explanatory variables in the Cox PH model can be a combination of categorical and continuous variables. Being able to handle continuous variables like voltages, currents or power levels is especially useful in an engineering context.

Another factor in the model's success is that it is *semiparametric* as the baseline hazard function does not need to be specified. The model parameters $\boldsymbol{\beta}$ can be estimated without requiring knowledge about the baseline hazard function and thus insight on the impact of the explanatory variables can be gained. The Cox PH model is also statistically *robust*, meaning that it will approximate the underlying parametric model when fitted [57, p. 110]. In addition to the effect size for the explanatory variables, as given by the estimated parameters $\boldsymbol{\beta}$, the standard error and confidence interval can be estimated as well. This enables valuable insight into whether the observed effects are statistically significant.

Estimation of the model's parameters is done using the maximum likelihood method. This work relies on the Python library *lifelines* [23], as it comes with tried and tested support for working with Cox PH models including parameter estimation. It also makes it possible to visualize the effect of explanatory variables on the survival function through the plotting of curves for given parameters.

It is common that a wide array of explanatory variables has been recorded for each specimen. An actual model consisting of a subset of these variables has to be decided upon before it can be fitted to the data. This model selection process is a central part of fitting a Cox PH model. Domain knowledge can guide the selection process and in some cases it is all that is needed. However, due to the number of possible variables an

optimization approach is required for the model selection process in most situations . This approach consists of a goodness-of-fit metric and a procedure optimizing it. AIC is a goodness-of-fit metric commonly used with Cox PH models [84, pp. 81–84]. It has been suggested by Akaike in 1992 [1] and is defined as

$$\text{AIC} = -2 \cdot l(\hat{\beta}) + 2k, \tag{2.13}$$

where $l(\hat{\beta})$ denotes the value of the partial log likelihood for a particular model and k is the number of parameters or variables in that model. As the AIC includes the number of parameters as a penalizing term it counteracts the tendency of the partial log likelihood value to overfit the data. It also makes it possible to compare models with different numbers of parameters.

The second part of the solution of the optimization problem is the procedure. When digital computers first became available their never before seen computing power lead to the development of the stepwise model selection procedure [32]. In the stepwise selection process the variable whose inclusion or exclusion improves the goodness-of-fit metric the most is selected and then either added or removed from the model. The process converges to a good or even the optimal solution. However, the processing power of today's computers is sufficient that it has become feasible to perform an exhaustive search. This approach computes the goodness-of-fit metric, for example the AIC, for every possible combination of parameters. All that is left is to choose the optimal solution based on the calculated metric.

3 Results

For this work 25 different driver types get tested at four different environmental conditions for a total of 75 tested devices. The reasoning behind the selection of the test conditions has been presented in Section 2.3.1. To reiterate, the four conditions are dry heat at 85 °C and damp heat at 65 °C/90 %, 75 °C/75 % and 85 °C/85 %. During the tests 39 failures are recorded. Only a single failure occurs in dry heat, the remaining 38 are observed during humidity testing. Table 3.1 lists the lifetimes of all the devices that fail in the damp heat tests. Each device is also marked with its corresponding failure mode. The in-depth failure mode analysis will be presented in Section 3.2. For a handful of devices it is not possible to determine the time of failure. They are marked accordingly.

A few general trends are immediately obvious when looking at Table 3.1. The tests at 85 °C/85 % can be considered to be the most brutal, as evidenced by the rather short lifetimes devices experience in that environment. An especially drastic case is the driver with unique identifier (UID) V091 that is power-cycled hourly during the test. It lasts only 31.25 h. It is also noteworthy that a substantial number of devices outlast the duration of the test and are therefore right-censored data points. Again, these are marked accordingly. As only a single device fails in dry heat test there is no column for this condition in Table 3.1.

This chapter will first present an analysis of how the electronic capacitors have fared in the devices that are tested in dry heat. Popular notion that many SMPS circuits fail due to degraded electrolytic capacitors. This is followed by the results of the detailed failure mode analyses. As each failure mode is quite unique they are each presented in their own section.

3.1 Degradation of Aluminium Electrolytic Capacitors

It is commonly assumed that aluminium electrolytic capacitors are the most failure prone component in SMPS circuits[44, 8, 43, 73]. The off-line LED drivers that are tested for this work are all based on the SMPS architecture and should therefore be susceptible to the same failure modes. To put this assumption to the test, an accelerated lifetime experiment is conducted by applying dry heat at 85 °C to the specimens. As the evaporation of the liquid electrolyte is the most common failure mechanism for aluminium electrolytic capacitors [125], the lifetime of the tested drivers should be severely decreased when placed in a hot environment.

The test is terminated after 14 400 h. The devices are power cycled in one hour intervals for a span of 5160 h to add an additional stress. Over the course of this inordinately long test run only a single device fails. That failure however is not due to the degradation of one of its electrolytic capacitors but rather caused by a metal-oxide-semiconductor field-effect transistor (MOSFET). The failure is presented in more detail in Section 3.2.4.

The aluminium electrolytic capacitors in the tested devices are tested individually to determine the amount of damage they have accrued. All tested drivers are disassembled and their capacitors desoldered so they can

be measured outside of the circuit. For the measurement a HAMEG HM8118 inductance (L), capacitance (C) and resistance (R) (LCR) meter is used. The accuracy of this meter is 0.5 % or better in all ranges, which guarantees trustworthy readings. The measured capacitance and ESR values are presented in Table 3.2.

To support the interpretation of Table 3.2, two columns are added that show the difference between specified and measured values in percent. Additionally, the cells in this column were assigned a color based on the magnitude of the change. A range of colours between green and yellow is used, with green indicating negligible change and yellow one that is approaching the critical level. The critical level is defined as a drop in capacitance of 20 % or an increase in ESR by a factor of two. These changes are commonly considered to mark end of useful life of a capacitor [125]. A capacitance change of more than 20 % is also considered a failure by the requisite standard in the dry heat test done for the component level qualification of capacitors [38]. Looking at Table 3.2 it is obvious that these capacitors have fared exceptionally well. The capacitance drops on average by about 8 % with a maximum of 16.5 %. The increase in ESR is at most 34.1 %, with most capacitors measuring less than the value specified in the datasheet.

The capacitors used in most driver designs can be separated into two groups: energy storage and decoupling. Energy storage caps can either be found in the PFC stage or at the output of the main converter in single stage designs. They have a high energy capacity and are typically rated for high working voltages such as 450 V or even more. Decoupling caps can store less energy and are therefore physically more compact. They are used in other parts of the circuit, too, for example for an auxiliary power supply or in the control loop of the SMPS controller IC. Table 3.2 shows that the energy storage capacitors are even more robust than their decoupling brethren. This is a desired outcome, as these capacitors are usually vital to the correct function of the device. It is also no wonder, as all manufacturers chose high quality capacitors from renowned brands for this task.

Whether a certain level of degradation of a aluminium electrolytic capacitor causes the failure of a device, first and foremost depends on the actual circuit design. In other words, the amount of parametric change of its components a circuit can stomach is heavily influenced by design decisions. Therefore, defining a fixed failure criterion for drivers in general is nigh impossible. Luckily, in the case of the capacitors scrutinized for this work, the extent of degradation is minimal and it can be said in good conscience that it would not have detrimental effects on the operation of the tested devices.

Table 3.1: List of lifetimes for all drivers that were tested in damp heat.

Manufacturer	Manufacturer part number	Lifetimes / h		
		65 °C/90 %	75 °C/75 %	85 °C/85 %
BAG	CCS1150-50FR-20/220-240	5781.38[†]	8055.88[†]	2592.50[†]
BAG	CCS170-35QS-01/220-240	5781.38[†]	8055.88[†]	947.75[1]
BAG	LCS130-70FX-30/220-240	5781.38[†]	6389.63[9]	1067.75[9]
ERP	PSB30E-0700-42-T			2808.25[†]
LG Innotek	LLP 150W 0.7A 125 280Vdc PISE-A150D	1646.13[9]	513.38[9]	555.75[9]
LUMNIUM	54H-120B-GM-0450			1273.25[7]
N/A	CLNC24W028L			1819.25[9]
N/A	CLNC65W042L			931.25[5]
N/A	LGM22W016P2			2299.00[4]
N/A	LGM52W041P2			2019.00[6]
OSRAM	OT 165/170-240/1A0 4DIMLT2 E	5781.38[†]		*N/A*
OSRAM	OT 40/120-277/1A0 4DIMLT2 E	4328.13[3]	4689.63[3]	1075.75[3]
OSRAM	OT FIT 35/220-240/700 CS	5781.38[†]	8055.88[†]	1463.75[9]
OSRAM	OTi DALI 60/220-240/550 D LT2 L	5781.38[†]	6999.63[1]	2109.75[9]
OSRAM	OTi DALI 90/220-240/1A0 LT2 L	5781.38[†]	8055.88[†]	2097.75[5]
Philips	CertaDrive 60W 360mA 170V 230V			1355.25[2]
Philips	CertaFlux LLS ES 1150m 4500lm 840 HVI MST	1641.88[1]	1341.38[1]	583.75[1]
Philips	Xitanium 9290 008 818	5781.38[†]	4163.63[9]	2592.50[†]
TRIDONIC	LC 25W 100-500mA flexC lp EXC	5781.38[†]	8055.88[†]	2592.50[†,9]
TRIDONIC	LC 57/1050/54 fixC lp SNC2			1272.50[1]
Vossloh-Schwabe	ECXd 700.149	5781.38[†]	5539.63[3]	31.25[*,3]
				1565.75[3]
				1753.00[3]
Vossloh-Schwabe	ECXe 1050.233			665.00[1]
				1155.25[1]
Vossloh-Schwabe	ECXe 350.298			419.25[8]
				573.00[9]
Vossloh-Schwabe	ECXe 700.199	1361.88[1]	8055.88[†]	*N/A*
WE-EF	ED100-66/700-1050/230-50-60/O-O	5781.38[†]	4773.38[7]	519.08[7]
				2808.25[†,7]

N/A Device failed, but time of failure could not be determined.
[†] Right-censored lifetime.
[*] Device was power-cycled hourly during the test. Lifetime will be excluded from further analysis.

Failure mode:
[1] Dielectric breakdown [2] Diode [3] IC package [4] Inductor [5] Metal film capacitor
[6] MOSFET [7] MOV [8] Resistor [9] Unknown

			datasheet values			measured values			
UID	Manufacturer	Series	Cap. / µF	Voltage rating / V	ESR / Ω	Cap. / µF	ESR / Ω	ΔCap.	ΔESR
V001	Aishi	CD11GES	22	500	14.47	19.90	5.71	−9.55 %	−60.5 %
V001	Aishi	RZ	56	80	2.37	49.10	1.32	−12.3 %	−44.3 %
V030	Aishi	CD11GE	15	450	17.68	14.41	6.10	−3.93 %	−65.5 %
V030	Aishi	RS	68	100	1.56	56.86	1.80	−16.4 %	15.4 %
V030	Aishi	RS	150	100	0.71	129.1	0.43	−13.9 %	−39.2 %
V036	Aishi	CD11GE	15	450	17.68	14.52	5.97	−3.20 %	−66.2 %
V036	Aishi	RS	68	100	1.56	56.76	1.48	−16.5 %	−5.15 %
V042	Rubycon	BXA	10	450	26.53	9.490	9.39	−5.10 %	−64.6 %
V042	Rubycon	ZLH	47	35	3.39	40.77	3.43	−13.3 %	1.29 %
V042	Rubycon	ZLJ	120	63	0.99	112.6	0.39	−6.17 %	−60.8 %
V043	Aishi	CD11GE	15	450	17.68	13.98	7.00	−6.80 %	−60.4 %
V043	Aishi	RS	220	35	0.72	188.6	0.97	−14.3 %	34.1 %
V049	Rubycon	BXC	10	450	26.53	8.670	22.5	−13.3 %	−15.3 %
V050	Rubycon	BXA	10	450	26.53	10.85	14.4	8.50 %	−45.5 %
V056	Nippon Chemi-Con	GXE	47	50	2.82	42.96	3.00	−8.60 %	6.31 %
V056	Nippon Chemi-Con	KZN	680	100	0.16	652.6	0.05	−4.03 %	−68.0 %
V056	Nippon Chemi-Con	KZN	680	100	0.16	650.3	0.05	−4.37 %	−69.2 %
V062	Rubycon	BXC	15	450	17.68	14.61	7.01	−2.60 %	−60.4 %
V062	Rubycon	RX30	15	50	8.84	13.17	2.28	−12.2 %	−74.2 %
V063	Rubycon	RX30	15	50	8.84	13.87	2.60	−7.53 %	−70.6 %
V063	Rubycon	BXA	22	450	12.06	21.50	6.85	−2.27 %	−43.2 %
V075	Chang	RT	10	50	13.26	9.510	16.5	−4.90 %	24.4 %
V075	Nippon Chemi-Con	KY	100	25	1.86	86.72	1.51	−13.3 %	−18.7 %
V075	nichicon	HE	820	63	0.15	779.6	0.07	−4.93 %	−48.5 %
V092	Aishi	CD11GES	27	450	9.82	24.26	3.48	−10.1 %	−64.6 %

Table 3.2: Capacitance and ESR values for aluminium electrolytic capacitors from a test in dry heat at 85 °C. The capacitors were desoldered from the tested devices after the experiment was terminated. Datasheet specifications are included for reference.

3.2 Failure Modes

Once a device fails and the time of failure has been recorded, the question of which mechanism caused the failure and what triggered it has to be resolved. This requires a forensic approach as outlined in Section 2.5. From a total of 39 failed drivers the failure mode can be determined for 27 devices. The frequency of the different failure modes is shown in Figure 3.1. Dielectric breakdown of the PCB material is by far the most common failure mode. Failures of a diode, inductor or resistor are only observed in one case each.

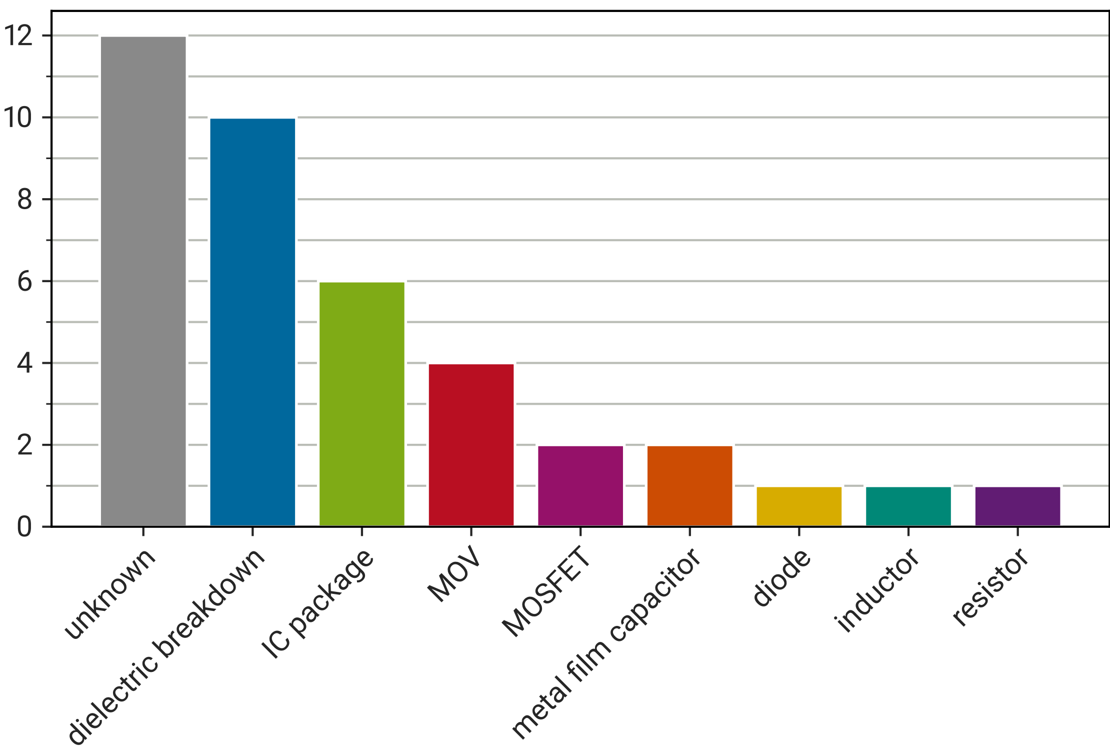

Figure 3.1: Bar chart illustrating the frequency of the different failure modes identified in the tested devices.

The physics behind each failure mode are substantially different, warranting a separate section for each one. The sections are organized by the affected components. In the following eight sections the observed failure modes will first be introduced through a literature review. This is followed by a forensic analysis showing in detail how the failure mode manifests itself in a given device. Unambiguously identifying the correct one based on what can be observed from a failed driver can be tricky as one defect can trigger secondary ones. The presented analyses are therefore given the utmost care. A subset of the findings presented below has been published before in [142].

3.2.1 Dielectric Breakdown of the PCB

Although dielectric breakdown can affect all components of an electronic circuit assembly, this section will be limited to breakdown occurring on or inside the PCB. As this failure is only encountered under damp heat conditions, only the mechanisms sensitive to moisture are taken into account.

It is commonly understood, that the presence of moisture can decrease the insulation resistance of the PCB material and thus lead to dielectric breakdown [80, s. 14.3.3]. This effect is amplified if ionic contaminants are present. For example, Verdingovas, Jellesen, and Ambat [121] could demonstrate that the acidic residues left on the PCB by common lead-free fluxes can cause leakage that increases exponentially with relative humidity. Zhan, Azarian, and Pecht [135] have reported sudden drops of surface insulation resistance in the presence of certain flux types. According to their research it is caused by an acidic electrolyte piercing the oxide layer of the metal pads and thus forming a conductive path between them. Although modern so called *no-clean* fluxes supposedly do not require cleaning after circuit assembly, they can leave acidic residues if heat is not applied evenly to the board [51]. The presence of contaminants is not limited to the surface of the PCB. They can also find their way into the PCB material itself during the manufacturing of the board. This can cause dielectric breakdown along the contaminated glass fibres [82].

Four mechanisms that can lead to dielectric breakdown in or on the PCB can be identified [18, s. 57.2.1.3]:

1. conductive contaminant bridging,
2. dendritic growth,
3. conductive anodic filament growth and
4. metal whiskers.

In conductive contaminant bridging two conductors are shorted by the dissolved ionic residues themselves. These residues form an electrically conductive electrolyte film on the PCB's surface, which can short conductors of different potential [120]. Depending on the current capability and sensitivity this short can cause a circuit malfunction or even catastrophic failure.

Dendritic growth is a two step process. In the presence of moisture, metal ions coming from the component leads or tracks dissolve and form an electrolyte on the surface of the PCB. These metal ions migrate from an anode to a cathode bias along a conductive path under DC bias. They are deposited at the cathode, forming a metallic dendrite [59]. This dendrite can either directly short the two electrodes or reduce their isolation distance to the point where an arc can form.

The most glaring difference between dendrites and conductive anodic filaments is that the latter one grows from anode to cathode. These filaments form inside the PCB and follow the glass fibres [70]. Moisture induced delamination next to the anode forms the pathway for the growth of the filament and electrochemical breakdown of the anode supplies the metal ions that finally form the filament [101]. Once the filament is fully formed it can lead to a short between the anode which in turn causes the failure of the circuit. The presence of moisture and ionic contaminants is required for both the delamination as well as the electrochemical reaction to progress.

Metal whiskers are the third type of metallic filament that can cause shorts between different contacts. These filaments are very thin and can spontaneously erupt from metal surfaces. Engineers and scientist became aware of this effect during World War II as they caused notable trouble with military equipment [14]. Research into this failure mechanism took off in the 1950s and is ongoing to this day [93, 60, 34, 85]. A wider audience was introduced to them due to their suspected role in the failure of the accelerator pedal in Toyota cars in the early 2000s [111]. Sudden acceleration probably caused by malfunction of the accelerator pedal lead to drivers losing control over their vehicle and multiple cases of injuries and even fatalities. However, even after decades of research acceleration factors for the growth of metal whiskers could not be identified [91]. It is therefore unlikely that any of the failures caused by dielectric breakdown can be traced back to metal whiskers. If that would be the case, the devices would fail at a comparable rate in the field.

Several cases of dielectric breakdown were observed in the experiments and their detailed description can

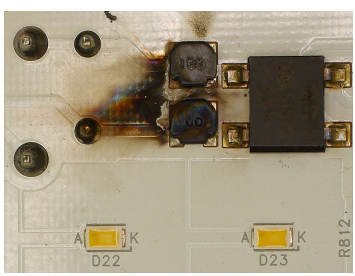

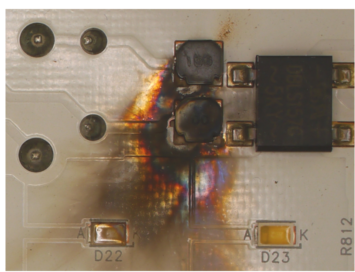

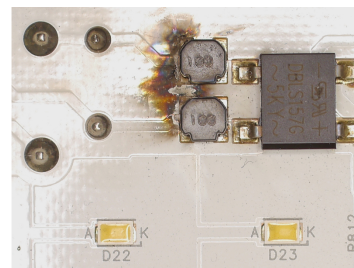

Figure 3.2: Pictures showing the breakdown on the PCB between two inductors for all three failed devices. The failure mode is highly consistent, presenting an almost identical sight in the three devices.

be found below. It was however not possible to determine which of the four aforementioned mechanisms caused these failures, as the resulting short-circuit events caused too considerable damage, making a more detailed analysis all but impossible.

Philips CertaFlux LLS ES 1150m 4500lm 840 HVI MST

This driver integrates one half of the LED module on the same board and is designed for use in industrial vapour tight linear lighting fixtures. Its PCB is single-sided and generally made to a lesser standard. The board seems to be made from FR-2 material. Catastrophic failure has been recorded for the three devices tested in damp heat. The failure is caused by an arc forming between two inductors that are part of the primary side EMI filter. The inductors are wired in series with the neutral and life leg of the line voltage and thus suppress differential mode noise coming from the driver's converter circuit from flowing back to the grid. The current flowing in the arc between the inductors triggers the input fuse of the driver as a secondary effect, leading to the total failure of the device. The distance between the sharp corners of the two pads is merely 1 mm.

Figure 3.2 shows the metallic shine caused by metal deposited on the PCB during the eruption of the plasma arc. Judging from the burn marks, it comes as no surprise that the current flow triggered the input line fuse of the driver. Thanks to the online monitoring during testing, this current flow can be quantified. The current draw and power factor for the three failed devices is presented in Figure 3.3. The device with V016 shows the smallest acceleration factor as it was tested at 85 °C/85 %. As it took the longest time to finally fail the highest RMS current is recorded for it. Just before the failure happened its current draw surpassed 350 mA, more than twice the normal operating current. Still, the curves for the three devices look nearly identical. That these three measurements closely agree supports the assessment that the dielectric breakdown is the root cause leading to the failure of the three devices. That the applied external stresses (humidity and temperature) do indeed accelerate the progression of this failure mechanism is backed up by the different timescales.

The progression over time of the power factor supports the hypothesis of an arc forming between the two terminals. The power factor starts out at over 0.9 and then increases over time. This increase is due to the degradation of metal film capacitors, effectively reducing the capacitance connected across the power line. However, once the current draw starts to increase due to current flowing through the arc, the power factor decreases. An electric arc represents a highly non-linear load as it only ignites once a certain voltage threshold is crossed. Thus, its power factor is quite low. As the current draw of the device under test becomes dominated by the arc its power factor continues to decrease.

Figure 3.3 also shows an unusual *snap-back* effect after the initially exponential rise in current. It seems like the arc caused an effect that limited and even reduced its own impedance. Yet, this only delays but does not stop the current finally exceeding a sustainable level and triggering the input protection fuse, rendering

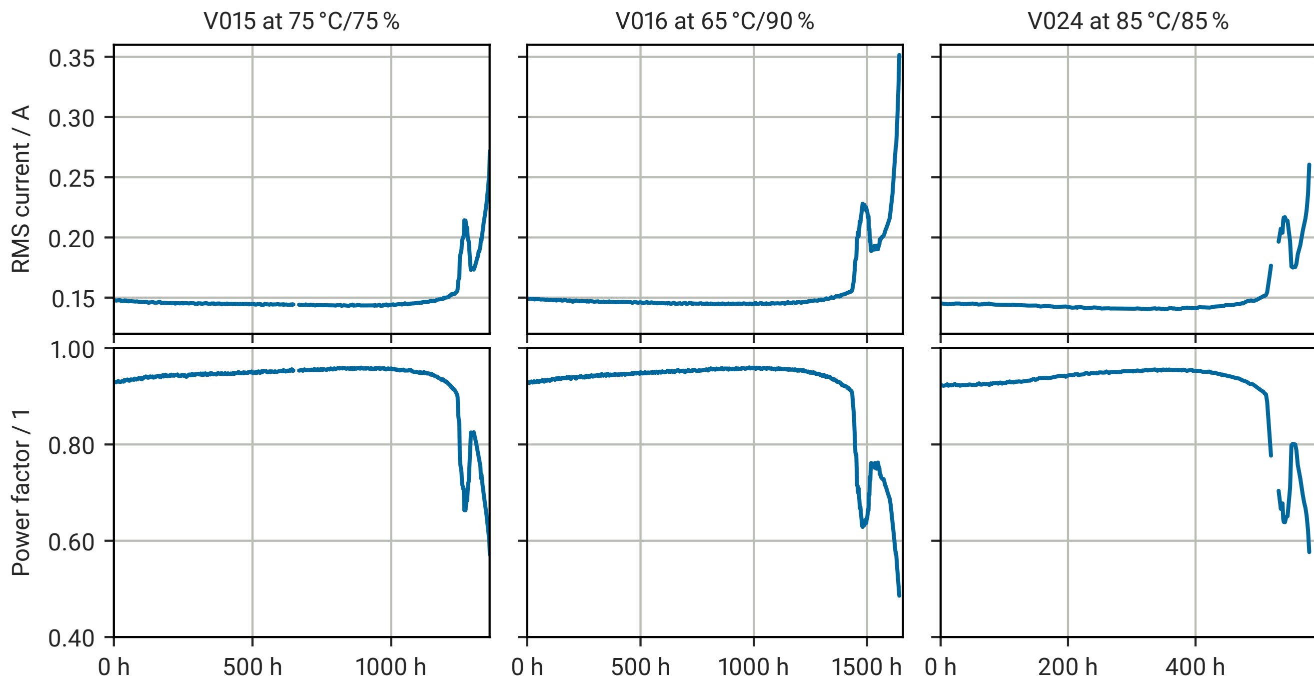

Figure 3.3: Plots of primary side RMS current and power factor for the three failed devices. The three devices show identical behaviour: before the failure the current increases while the PF simultaneously decreases. Due to equipment malfunction the plot for the third driver shows a gap in the data.

the device inoperable.

BAG CCS170-35QS-01/220-240

This medium-power constant current driver is rated for indoor use. It is tested in dry heat and in 65 °C/90 %, 75 °C/75 % and 85 °C/85 %. Curiously, only the device V037 subjected to the 65 °C/90 % environment failed in unexpectedly spectacular fashion. The intense burn marks on the PCB shown in Figure 3.4 made the the analysis of the failure mechanism quite challenging. After most of the soot had to be cleaned up before the damage could be properly assessed. To aid with the analysis the outlines of the through-hole technology (THT) components on the top side of the assembly are shown as semi-transparent overlays in Figure 3.4.

To isolate the likely root cause of the failure an event tree is drawn up. Martin presents this approach in his 1999 book [80, s. 14.5.4] for the analysis of failures of PCBs. The result is presented in Figure 3.5. The analysis concludes that the dielectric breakdown most likely originated on the surface of the PCB and between the pads of the large aluminium electrolytic capacitor mounted on the top side. Once the initial conductive path has been established the resulting charring and possibly arcing causes the damage to spread. This explains the size of the damaged area on the board.

Why this failure cannot be observed in the two other damp heat conditions is unclear. A possible explanation is that this device's PCB's surface was contaminated during manufacturing, making a dielectric breakdown more likely. It is also conceivable that the acceleration of failure mechanism is highly dependent on the relative humidity and have not manifested themselves at the 75 °C/75 % and 85 °C/85 % conditions by the time the

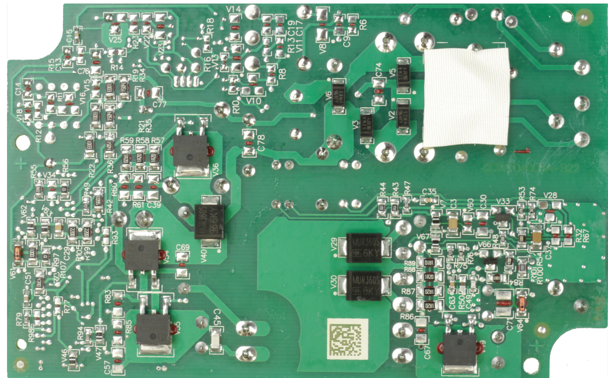

(a) PCB before testing.

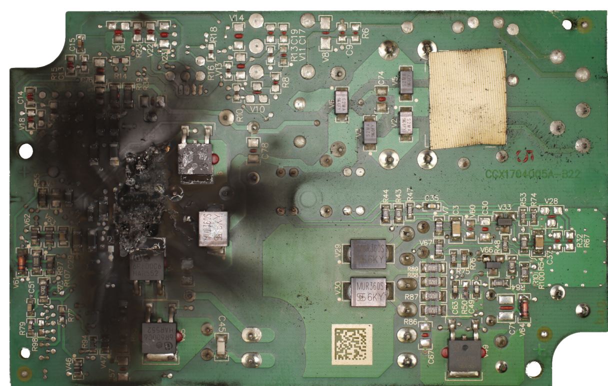

(b) PCB of failed device.

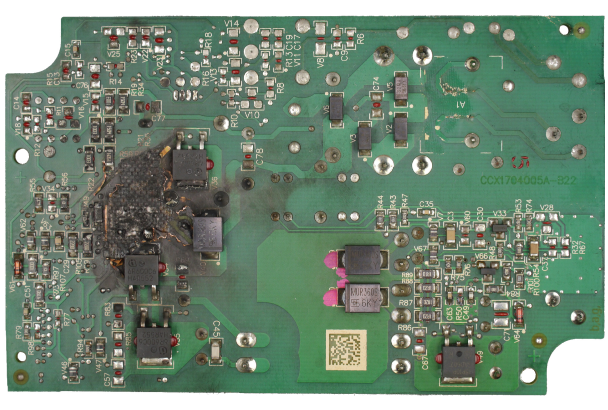

(c) PCB after cleaning.

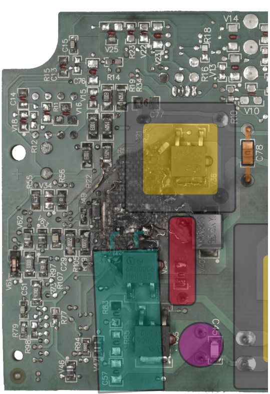

(d) PCB with top side components overlaid.

Figure 3.4: Analysis of the PCB from the failed device V037. First image shows the PCB before testing for reference. Burn marks are shown before and after the soot is cleaned up with isopropyl alcohol. Last image shows the PCB after cleaning and with the top side components in a transparent overlay (transformer yellow, diode orange, aluminium electrolytic capacitor turquoise, metal film capacitor red, inductor purple).

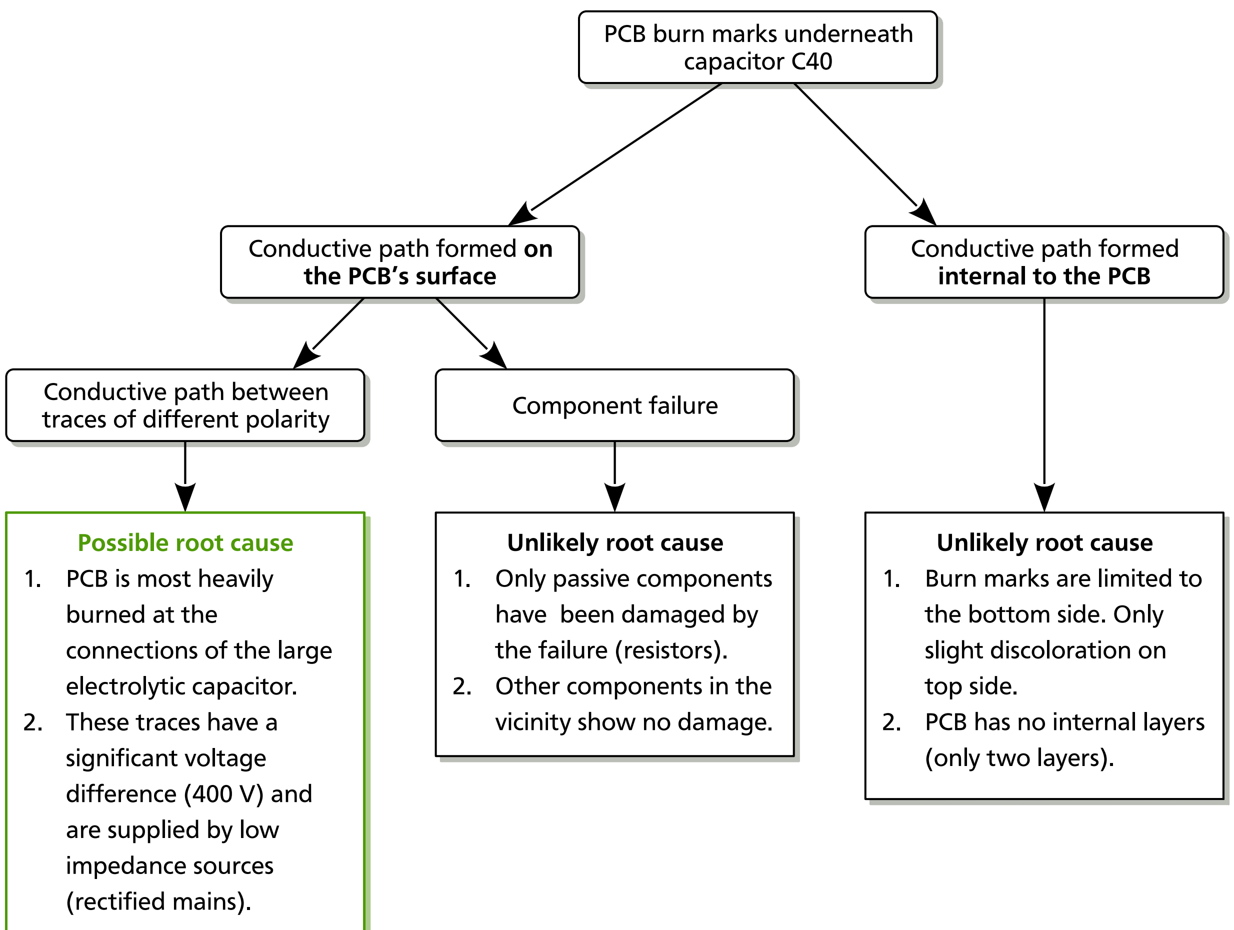

Figure 3.5: Event tree and analysis to determine the root cause for the dielectric failure of device V037.

tests are terminated.

It is also noteworthy that this failure does not announce itself in the monitored parameters. No notable increase in the primary side current just before the failure can be observed, which hints at it happening rather spontaneously. The other parameters did change over time but the trend is identical to what was recorded for the other tested devices.

OSRAM OTi DALI 60/220-240/550 D LT2 L

This is another driver rated for indoor use. It belongs in the medium-power class and can connect to a DALI bus. It stands out – at least for the purposes of the lifetime test – in that its PCB has four layers instead of the common two. This can be considered to be indicative of higher quality products. On the other hand it opens the possibility of failures due to a dielectric breakdown between in the inner layers. This failure mechanism is observed with the device V068 tested at 75 °C/75 %.

The visual inspection reveals a burned resistor. This resistor connects the PFC capacitor with the input of the auxiliary power supply for the microcontroller circuit. It is deduced that this resistor is a protective component and works akin to a fuse. As this resistor has clearly been burned by an overcurrent event, the root failure cause has to be located further downstream. Careful inspection reveals a small burned spot between two conductors on the bottom side. It can be seen in Figure 3.6a. By applying current to the auxiliary power supply circuit with a lab power supply it is confirmed that a short-circuit has indeed formed. The thermal image in Figure 3.6c shows that the location of this short-circuit coincides with the location of the burn mark, confirming the initial suspicion.

The output voltage $V_{DCDC,out}$ of the auxiliary power supply is measured to be 15.7 V and the voltage of the PFC V_{PFC} as 400 V. However, the short did occur between the PFC voltage V_{PFC} and the switching node of the auxiliary power supply $V_{DCDC,SW}$ as highlighted in Figure 3.6b. The voltage difference $V_{PFC} - V_{DCDC,SW}$ between these two nodes measures about 400 V. It briefly dips every time the MOSFET in the SMPS circuit is turned on. The simplified circuit diagram in Figure 3.6d shows to which nodes the measured voltages correspond in the used buck-converter topology.

It can not be said with certainty whether the breakdown occurred between these two voltage potentials due to $V_{DCDC,SW}$ being a node that sees continuous switching transients or because of contamination on the fibres of the PCB material.

TRIDONIC LC 57/1050/54 fixC lp SNC2

This is a simple fixed current driver rated for indoor use. It is lacking a communication interface and belongs in the medium power bracket. The device V111 that is tested at 85 °C/85 % failed due to dielectric breakdown.

The visual inspection of the failed device leads to the discovery of multiple severely burned surface-mount technology (SMT) resistors. Overall, the PCB shows intense discolouration. This might be due to it being made from inferior FR-2 material. In addition to the discolouration some components show signs of corrosion, too, such as the formation of white or green crystals at their terminations. The continuity check reveals that the device's fuse, which consists of two narrow tracks on the PCB, has burned out. It also identifies a failed MOSFET that is shorted between all three terminals.

The failed components are shown in Figure 3.7. The four parallel resistors forming the current shunt resistor have been consolidated into R2 in the simplified schematic. In this schematic a small flame icon indicates a failed component. In a second visual inspection under a microscope a dielectric breakdown on the PCB

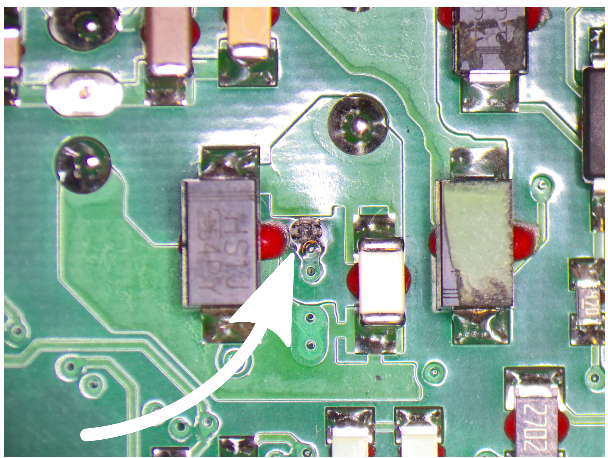

(a) Burned spot on driver PCB.

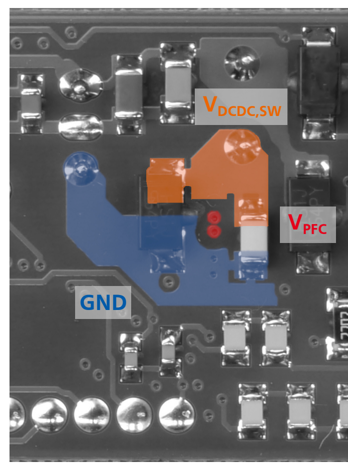

(b) Tracks surrounding the spot with voltage labels.

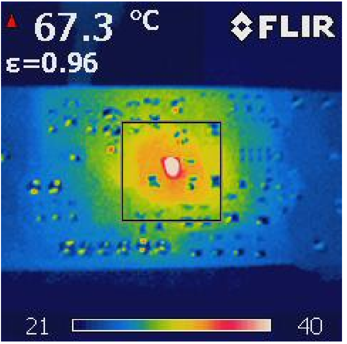

(c) Thermal image of the area while current is applied.

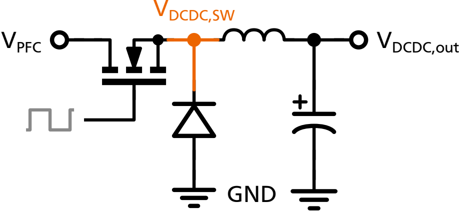

(d) Simplified schematic diagram of the buck-converter used for the auxiliary power supply.

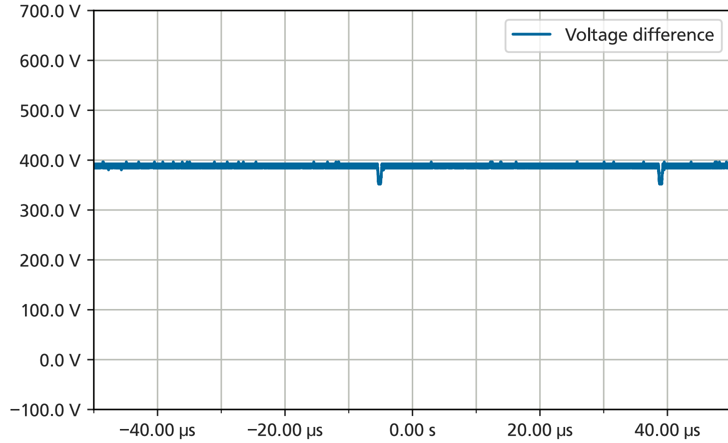

(e) Oscilloscope screenshot showing the voltage difference $V_{PFC} - V_{DCDC,SW}$.

Figure 3.6: Detailed analysis of the dielectric breakdown of device V068, from the location of the actual failure to the circuit schematic and finally the voltage difference between the nodes where the failure occurred.

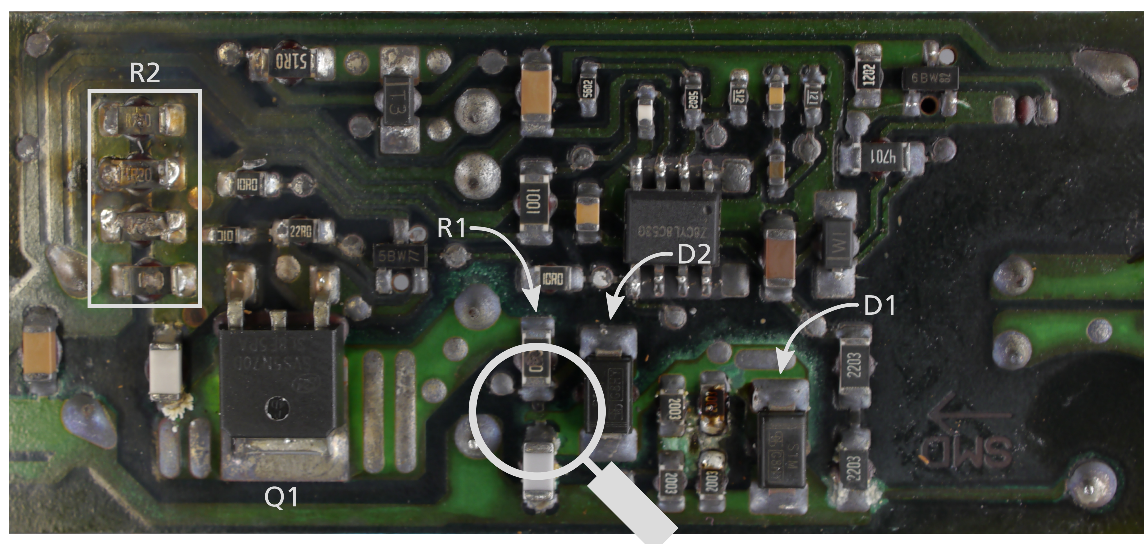

(a) Section of the PCB of the failed driver V111.

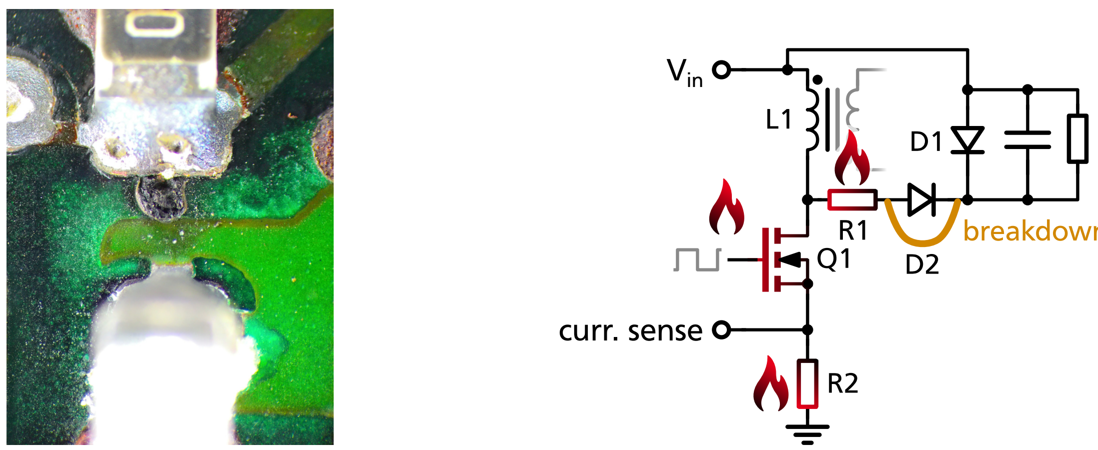

(b) Magnified area shows dielectric breakdown.

(c) Simplified schematic of the driver. Damaged components are marked

Figure 3.7: Damage on the PCB of driver V111. The damaged components can be referenced using the assigned designators. The magnified image highlights the breakdown that short-circuits diode D2.

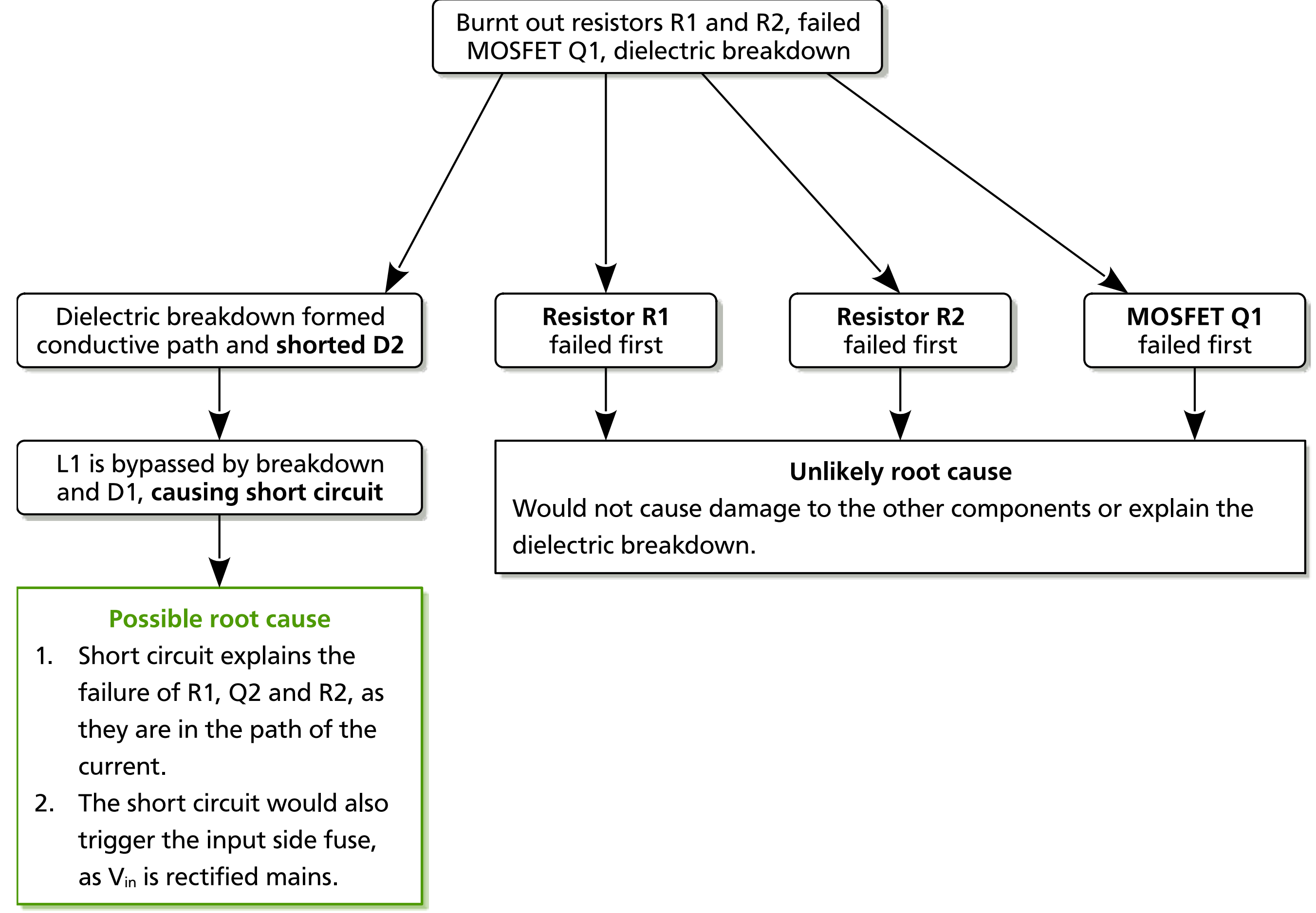

Figure 3.8: Event tree analysis of the failure of device V111.

between resistor R1 and diode D1 is discovered. As can be seen in the simplified schematic, this breakdown effectively short-circuits diode D2.

Due to the many failures found on this device an event tree analysis is conducted. Its results are presented in Figure 3.8. Although it cannot be ruled out that either of the five components D1, D2, R1, R2 or Q1 failed on their own, this would not explain the damage done to the other components and is considered to be unlikely. The dielectric breakdown that caused a short circuit across diode D2 is therefore thought to be the root failure cause. This short circuit effectively bypasses the coupled inductor L1 so it no longer limits the current flow. A much larger current can then flow through D1, R1, Q1 and finally R2 into ground. This current damaged all the components in its path.

At the location of the dielectric breakdown the distance between the PCB pads for the cathode of diode D2 and the right terminal of resistor R1 is approximately 0.5 mm. Rectified mains voltage is present across this very small isolation distance, resulting in a voltage difference of about 325 V DC.

Vossloh-Schwabe ECXe 1050.233

The Vossloh-Schwabe ECXe 1050.233 is a no-frills, low power driver with a fixed output current of 1050 mA. It features a single-sided PCB made from FR-2 material. Unsurprisingly, it is built using a single SMPS stage.

Two devices are tested in the 85 °C/85 % environment. The devices V118 and V119 failed after 665 h and 1155 h, respectively. The visual inspection finds that the shunt resistors have been severely damaged in both devices. Minor damage is found in the gate resistors connecting the control IC to the MOSFET's gate pin. The subsequent continuity check confirms that the input fuse of both devices has been triggered. It also finds a short circuit between all connections of the main switching MOSFET in both devices.

Under magnification a dielectric breakdown between the coupled inductor of the main SMPS circuit and the power supply of the control IC is found. In the schematic presented in Figure 3.9f this breakdown is marked by a lightning icon. To assess whether the voltage difference between the two affected circuit nodes is sufficient to trigger a breakdown and then damage the control IC it is measured using an oscilloscope. The result can be seen in Figure 3.9g. The voltage between the two nodes has a repetitive waveform at frequency of 100 Hz and reaches a peak of almost 500 V. The gap between these two nodes is just 0.6 mm wide, as shown in Figure 3.9c. It is reasonable to assume that the voltage difference is sufficient to trigger a dielectric breakdown.

The question remains whether this dielectric breakdown is the root failure cause. An event tree analysis is conducted to identify the root failure cause and its results are presented in Figure 3.10. A failure of either the MOSFET or the shunt resistors would cause a high current to flow through the inductor that – once the current flow is finally interrupted – would induce a high voltage across the terminals of the inductor. This voltage is also called back EMF. However, this voltage would be dissipated by the snubber network[1] placed across the terminals of the inductor. It is therefore highly unlikely that this series of events would lead to a dielectric breakdown. It would also not explain why the gate resistors were damaged as well.

Thus, it is safe to assume that the dielectric breakdown is indeed the root failure cause for both devices. The breakdown would form a conductive path between the high voltage present at the inductor and the low voltage power supply of the control IC. This voltage then finds a path through the IC's internal circuitry to the gate control pin and from there to the transistor's gate. As a MOSFET's gate is quite vulnerable to high voltages it is no surprise that it is catastrophically damaged. The failure of the shunt resistors is then caused by the high current flowing through the broken transistor. This chain reaction only stops once the input fuse of the device is triggered.

Vossloh-Schwabe ECXe 700.199

This low-power driver has all the hallmark features of a cost optimized design: its circuit board is single sided and made from FR-2 material; it lacks a PFC stage; its output current is selectable, but limited to three fixed levels. The three devices tested at 85 °C/85 %, 75 °C/75 % and 65 °C/90 % all fail during testing. Unfortunately, the time of failure can only be reliably determined for one of the three devices. The analysis of the failed devices finds intense burn marks on the bottom-side of their PCBs. Additionally, several areas show signs of corrosion. The burn marks are limited to the same area in all three devices, hinting at a common failure mode.

An in-depth visual inspection under a microscope reveals that a dielectric breakdown has caused the failure. It affects almost the exact same spot in all three devices. The detailed damage can be seen in Figure 3.11 for each device. The breakdown occurred between two windings of the coupled inductor that is part of the main flyback SMPS circuit. A schematic of the circuit can be seen in Figure 3.12. The primary winding is switched by the MOSFET which is in turn controlled by the IC. The IC requires a low voltage power supply. An auxiliary winding is used to supply this voltage during normal operation. The breakdown causes a high

[1]The snubber network consists of a diode, a resistor and a capacitor. No current flows through it during normal operation as the diode is reverse biased.

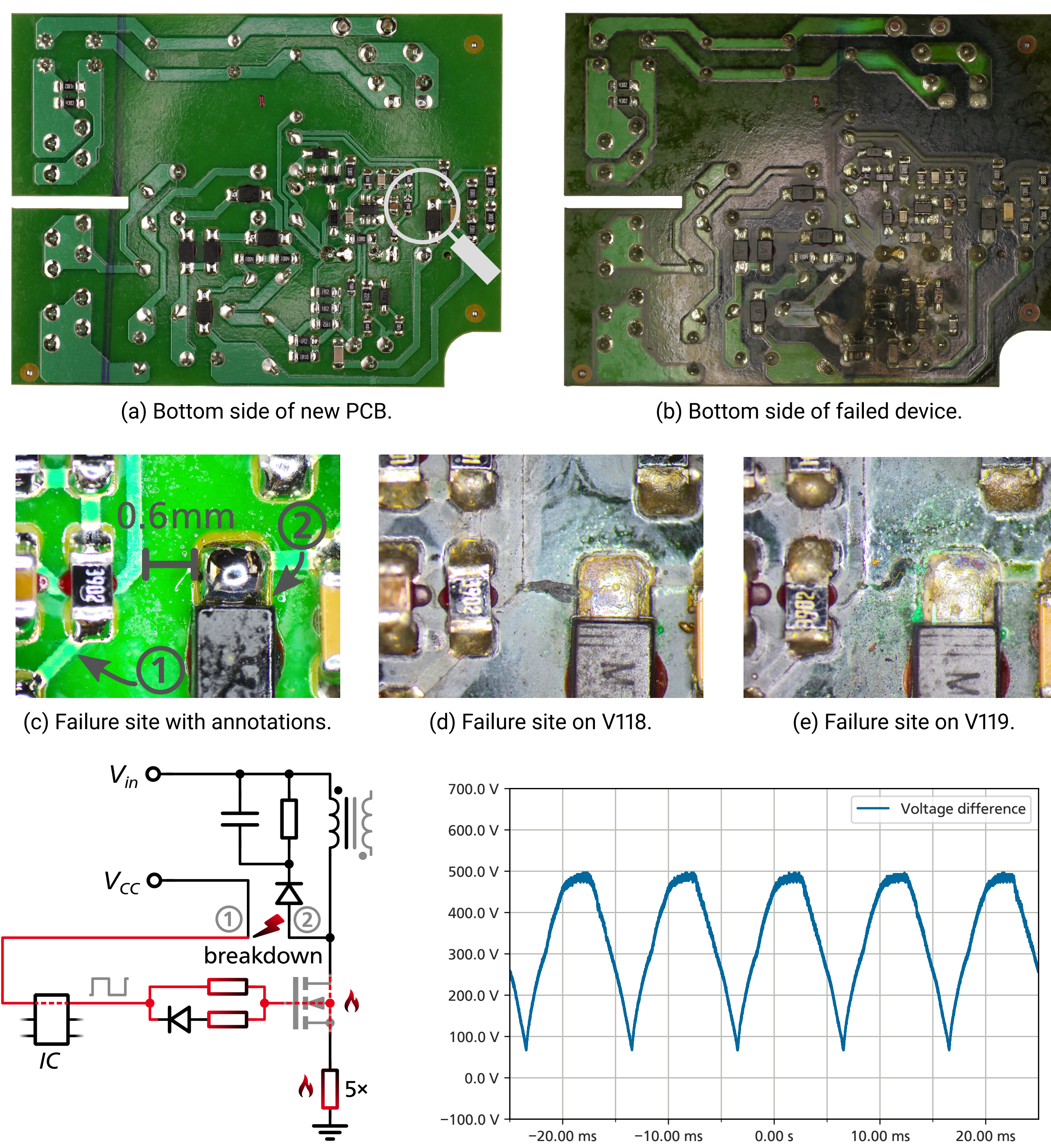

(a) Bottom side of new PCB.

(b) Bottom side of failed device.

(c) Failure site with annotations.

(d) Failure site on V118.

(e) Failure site on V119.

(f) Simplified schematic.

(g) Voltage difference between circuit nodes *1* and *2*.

Figure 3.9: Analysis of the failure of driver Vossloh-Schwabe ECXE 1050.233. The magnifier in the first image indicates where the failure was observed but on a new PCB. The first detail image also shows a new PCB. The breakdown on the devices V118 and V119 can be seen in the two following detail images. The voltage across the two circuit nodes where the breakdown occurred reaches almost 500 V.

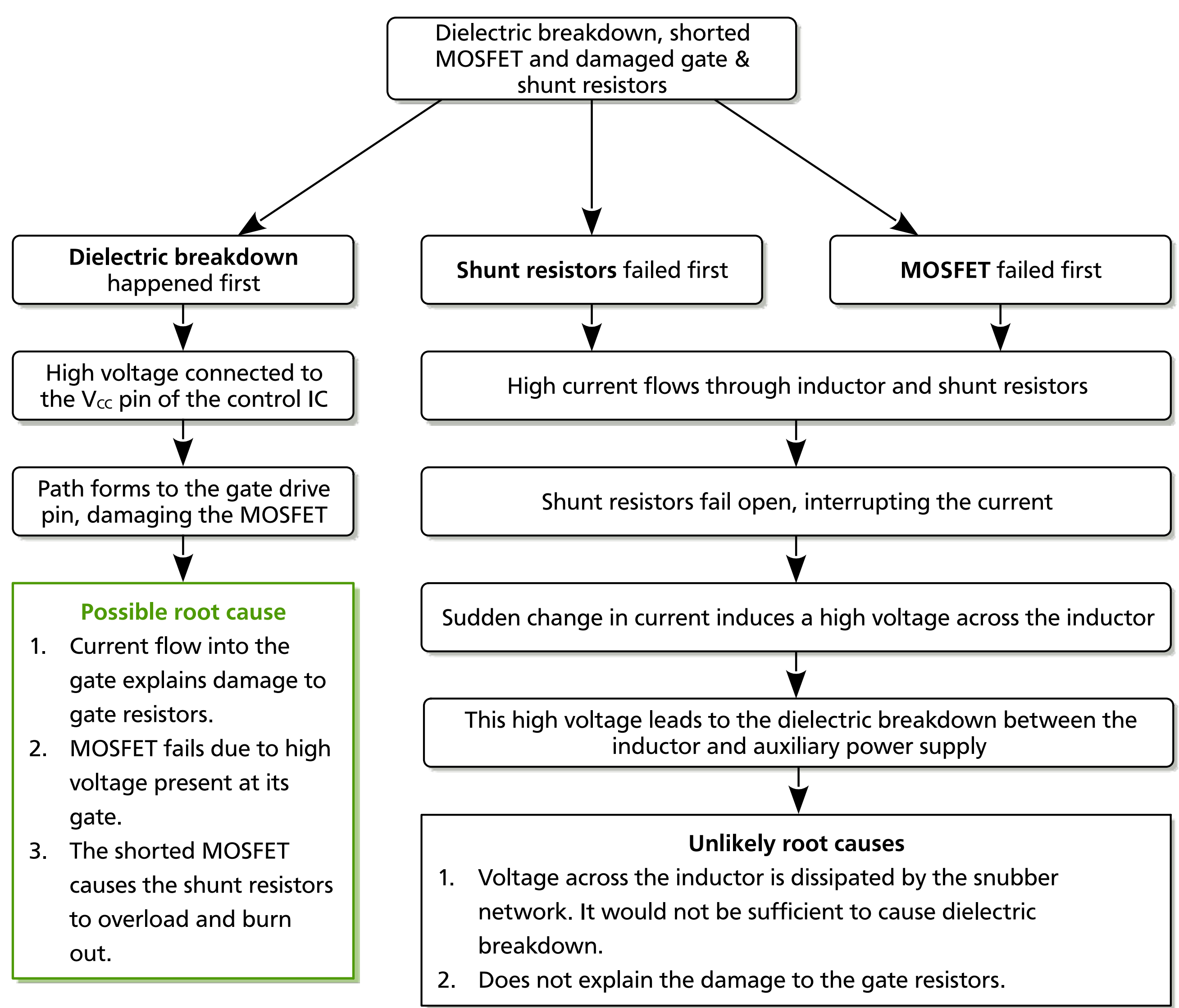

Figure 3.10: Event tree analysis of the failure of the driver Vossloh-Schwabe ECXe 1050.233.

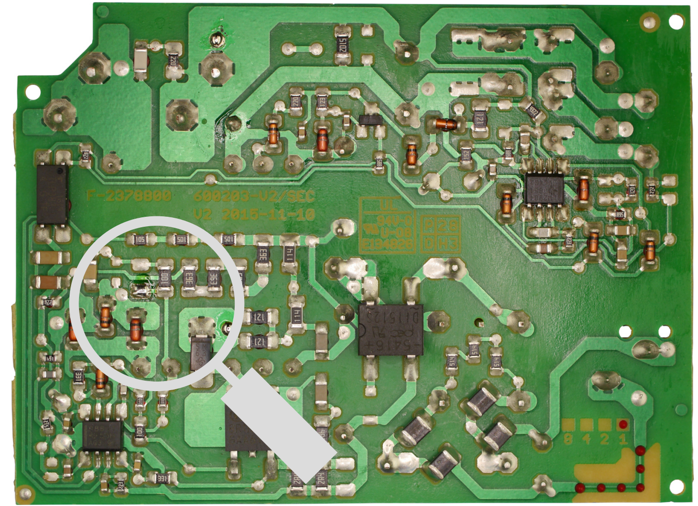

(a) Bottom side of new PCB.

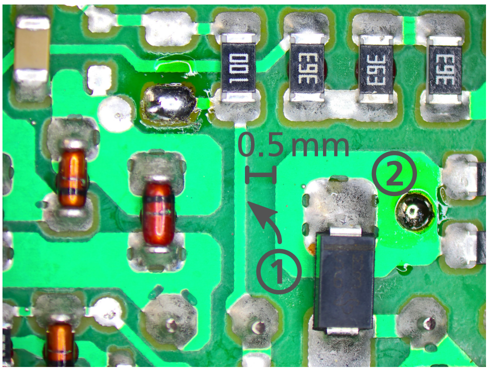

(b) Failure site with annotations.

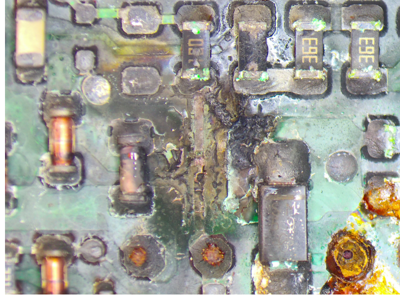

(c) Failure site on V076.

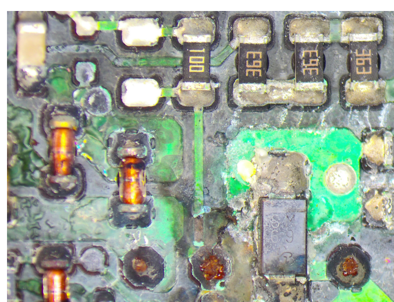

(d) Failure site on V077.

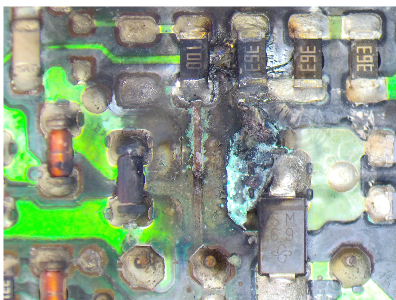

(e) Failure site on V081.

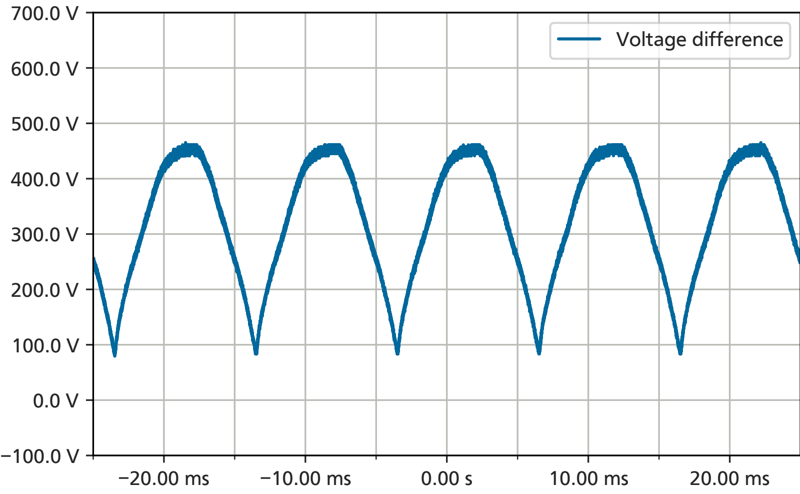

(f) Voltage difference between circuit nodes *1* and *2*.

Figure 3.11: Analysis of the failure of driver Vossloh-Schwabe ECXE 700.199. The magnifier in the first image indicates where the failure was observed but on a new PCB. The first detail image also shows a new PCB. The distance between the two circuit nodes measures barely 0.5 mm.

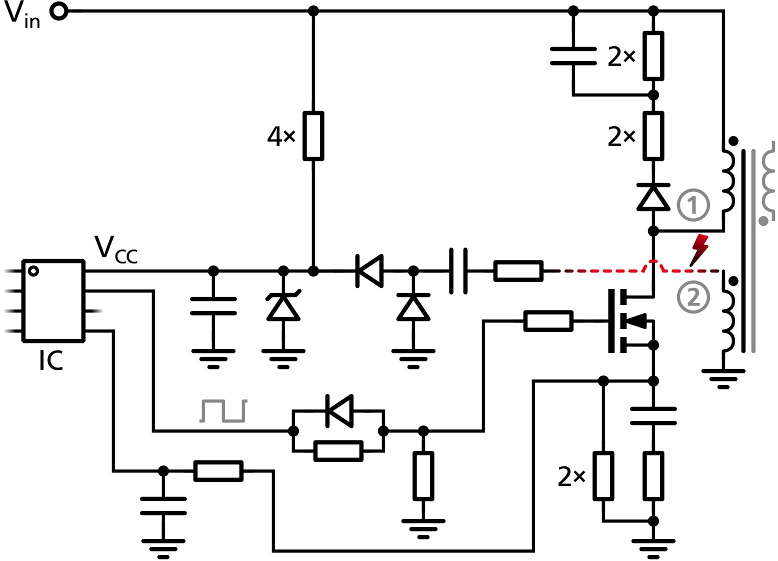

Figure 3.12: Simplified schematic of driver Vossloh-Schwabe ECXE 700.199. The path of the dielectric breakdown is indicated by a lightning icon. The trace that burnt-off as a consequence of that short is drawn dashed.

current to flow between the primary winding and this auxiliary winding, vaporizing the PCB track connecting the auxiliary winding to the power supply circuit for the IC. Without its power supply the control IC cannot function, thus causing a catastrophic failure of the device.

The output from the auxiliary is rectified with two diodes and its voltage clamped by a Zener diode. In two devices the Zener diode failed as a short circuit, again hinting at the significant current that must have flown during the failure event. The voltage between the two nodes – denoted 1 and 2 in the schematic and detail image – is measured with an oscilloscope. The result can be seen in Figure 3.11f. The voltage difference reaches almost 500 V during normal operation while the isolation distance between the nodes is a mere 0.5 mm.

3.2.2 IC Package Failure

The integrated circuit or IC for short has become the most important building block in modern electronic circuits. The level of integration and thus functionality achievable with ICs is impossible with discreet circuits. In recent years ICs have made a foray into the realms of power electronics thanks to modern semiconductor technology allowing them to cope with ever higher voltages. This evolution has lead to the introduction of highly integrated SMPS controller ICs for off-line power supplies like the ones found in the tested drivers. This section discusses the failure modes of the plastic packages of those ICs observed during testing.

It has been known that humidity can permeate plastic IC packages and subsequently cause device failures due to corrosion of the internal metallization at least since the 1960s [94, 117, p. 394]. In his seminal work Peck [95] presented a mathematical model for this type of failure. Corrosion is one the three major failure mechanisms of packaged semiconductors in humid environments. It might be surprising at first, but corrosion can not only interrupt electrical connections inside the package but also form new ones. This is due to dendrytic growth, a process in which metal ions are deposited along the field lines between an anode and cathode and thus forming a new conductive path. The effect requires the presence of water as an electrolyte. The metal ions are supplied by parts of the metallization that are subject to corrosion. This in turn can lead to shorts between potentials inside the package and finally to the catastrophic failure of the component. The work of Paye, Claudi, and Stecher indicates, that IC packages generally do not fail due to an dielectric breakdown of the mold compound [92]. It can be concluded that short current events inside the package are caused by the formation of conductive paths through to the aforementioned corrosive effects.

The second major mechanism is the so called popcorn failure. It is caused by the evaporation of water inside the package during reflow soldering. It gets its name from the popping sound that can sometimes be heard when the expanding water vapour causes the package to burst. Fukuzawa, Ishiguro, and Nanbu were the first to describe the mechanism in 1985 [39]. Continuous research in this area finally lead to the standardized moisture sensitivity qualification of plastic packages and the associated handling instructions [53, 52]. As this kind of failure is only observed during manufacturing it is out of the scope of this work.

Finally, the third type of failure mechanism that is commonly referred to in literature is hygroscopic swelling. Zhang et al. [136] and Fan and Suhir [37] treat this mechanism comprehensively in their works. Polymeric materials like the ones commonly used in chip packaging swell upon the absorption of moisture, as the water molecules occupy a certain intramolecular volume between the chains of the polymer. This causes mechanical stresses inside the packages and can decrease interfacial adhesion between the different materials used in the package. This can aggravate the popcorn effect, as water can condense once a gap has formed between different materials. The mechanical effects can also lead to fractures in the die or the chips contacts, e.g. bond wires. This type of failure is subtle in that it can typically not be seen with naked eye. However, very sensitive methods of analysis are capable of visualizing these failures. Examples of such methods include Moiré interferometry and c-mode scanning acoustic microscope (C-SAM) [37, 113 ff., 389 ff.]. Due to the high number of tested samples and the prohibitive costs of such analyses they could not be carried out for this work.

There are still other types of failure mechanisms, as indicated by the extensive collection of models in the JEDEC publication JEP122H [50, p. 93].

OSRAM OT 40/120-277/1A0 4DIMLT2 E

This is a low-power constant current driver rated for outdoor use. Still, all three devices tested in damp heat failed. The failure cause can be located in the SMPS IC that is part of the auxiliary power supply for the

microcontroller circuit. This supply is implemented as a basic buck converter with its input connected to the PFC capacitor. The high voltage of approximately 400 V present at this capacitor is directly fed to the SMPS IC, as it integrates a power MOSFET for switching as well as the required control circuitry. The IC is packaged in a comparatively small SO-8 chip package which severely limits the achievable isolation distances and thermal dissipation. After the failure a crack has formed on the top side of the IC, indicating that a thermal overload event occurred either on the die or between contacts of the lead frame. Figure 3.13 shows the cracks in the three damaged ICs in detail. The output voltage of the auxiliary power supply is measured to be 7.8 V in a driver that had not been subjected to any testing. No voltage is present at the output capacitor of the auxiliary supply of the three failed drivers.

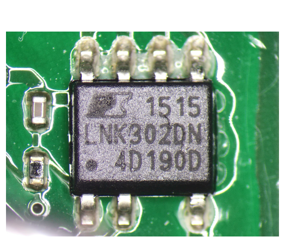

(a) New IC.

(b) Failure site for V002.

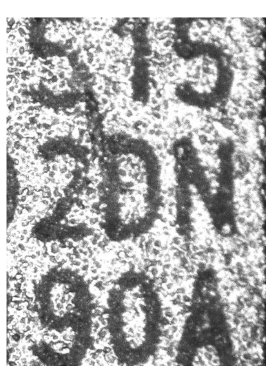
(c) Failure site for V003.

(d) Failure site for V004.

Figure 3.13: SMPS IC *LNK302DN* on the PCB and detail images of the three ICs showing cracks after they had failed. The images are shown in greyscale to enhance the contrast of the cracks.

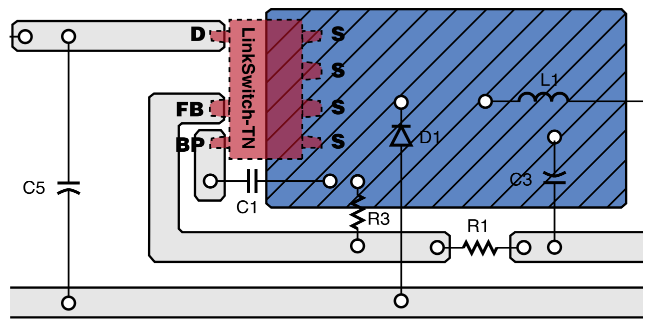

(a) Manufacturer recommended layout.

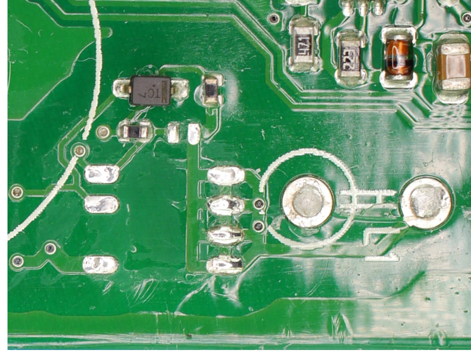
(b) Actual implementation.

Figure 3.14: Comparison between the layout recommended by the IC's manufacturer [76] and the actual layout found on the PCB of driver OSRAM OT 40/120-277/1A0 4DIMLT2 E. The chip has been removed so that the top copper layout is unobstructed. The layout is missing a copper fill connected to the IC's pins.

To confirm that the failure of the auxiliary power supply would cause a catastrophic failure, a new driver is modified by removing the SMPS IC. The driver was verified to work properly before the modification was carried out. After the modification the output of the driver is completely dead, confirming that the auxiliary power supply is essential for the driver circuit to work.

The mechanism that caused the failure of the SMPS IC is clearly dependent on the relative humidity in the

surrounding air. It could be caused by corrosion of the metal layers of the lead frame or even on the die. Yet, that might not explain the cracking of the plastic package. It is therefore deemed plausible that a leakage current started to flow between the high-voltage circuit nodes due to the ingress of humidity. At one point this current increased drastically which in turn evaporated the humidity or even burned the epoxy material of the plastic package. This internal pressure caused the package to crack while damaging the die, lead frame and/or bond wires at the same time, rendering the IC inoperable.

Examining the PCB of the driver it becomes apparent that the SMPS IC lacks a sufficient heat sink. Figure 3.14 shows the layout recommendation from the manufacturer's data sheet [76] next to the layout as it is found in the driver. There are no noteworthy copper areas connected to any of the pins of the IC's package as would be recommended by the manufacturer. It is likely that this lack of cooling aggravated the effects the accelerated test had on the driver.

Vossloh-Schwabe ECXd 700.149

This medium-power driver with programmable output current also failed due to damage in an IC package. The three devices tested at 65 °C/90 % as well as one tested at 75 °C/75 % show this type of failure. Figure 3.15 shows the dead ICs on the four failed devices. This IC is once more an SMPS controller providing the auxiliary power supply for the microcontroller circuit. Part of the plastic package has been blasted away by a pressure that seems to have built up at the interface between the package and the die. As the device tested in dry heat did not suffer such damage, it can be concluded that this failure mechanism is triggered by humidity. As previously discussed, it is plausible to assume that this type of IC is susceptible to this type of failure due to the high voltages present on the die and on the lead frame.

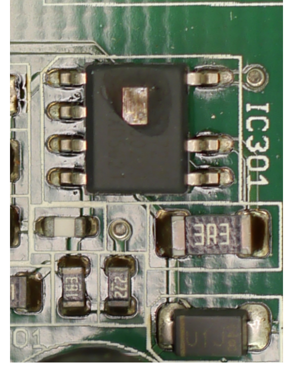

(a) Failure site for V084.

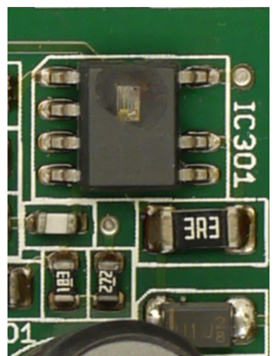

(b) Failure site for V088.

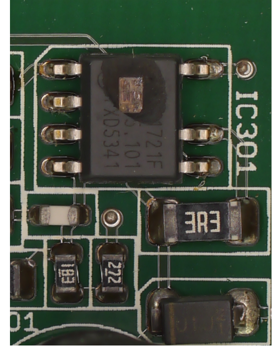

(c) Failure site for V091.

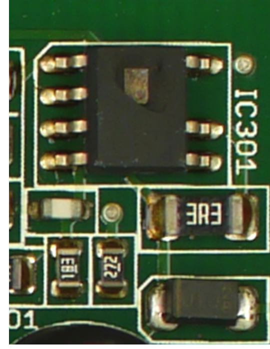

(d) Failure site for V086.

Figure 3.15: Pictures of the damaged ICs from the four failed devices. The damage pattern is almost identical between the four images.

One of the three devices tested at 65 °C/90 % failed after just 30 h. This device was power-cycled every hour (one hour on, one hour off). The failure mode is identical to the other failed devices. It can therefore be concluded that the power-cycling drastically accelerated this failure mode. Mc Brien and Heltzel [82] have shown that the insulation resistance of PCB material dropped significantly in a high humidity environment after the first thermal cycling. As the IC that failed in this device is expected to heat up due to switching losses, it is feasible that the power-cycling caused a similar effect. Another possible explanation is that the temperature swings created by the power-cycling caused a kind of pumping effect that accelerated the transport of moisture into the package where it could cause damage. Conseil et al. [17] have observed such

an effect with plastic cases that are typically used to house electronic assemblies. In their experiments the temperature cycling led to accumulation of water vapour inside the case. If a similar effect would apply to IC packages it could explain the massive lifetime acceleration that the power-cycling caused.

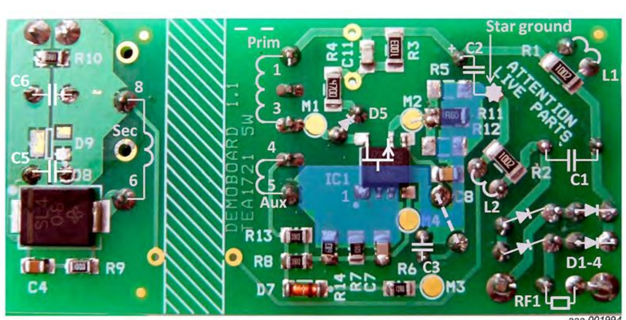

(a) Manufacturer recommended layout.

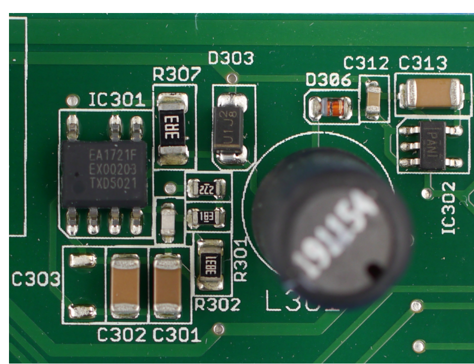

(b) Actual implementation.

Figure 3.16: Comparison of the manufacturer recommended layout for the IC [114] and the actual implementation on the PCB of driver Vossloh-Schwabe ECXd 700.149. There is no copper fill connected to the IC's pins in the implementation.

Once again, no discernible efforts were made to dissipate the heat generated by the SMPS IC. The manufacturer's application note explicitly recommends a copper area connected to certain pins of the IC for cooling [114]. Figure 3.16 shows the recommended board layout next to the actual implementation in the driver. It is once more reasonable to assume that improved cooling would have extended the lifetime of the driver in damp heat conditions.

3.2.3 Metal Oxide Varistor

MOVs were invented in Japan in the late 1960s [31] and have become ubiquitous over the following decades, thanks to their ease of use and performance in surge suppression applications. They are functionally similar to Zener diodes as their I-V-characteristic shows a steep increase in current once a voltage threshold is surpassed. They differ from Zener diodes in that they are bidirectional devices, meaning that their clamping behaviour is independent of the polarity of the applied voltage. They are also fundamentally different in how they are made: varistors are manufactured by sintering metal oxide grains (typically zinc oxide (ZnO)) into a cylindrical shape of variable height and then adding electrodes at the end faces. The grains form semiconductor junctions at their boundaries, thus the current capability of the component is determined by the cylinder's diameter and its breakdown voltage by its height [74]. The formation of these junctions cannot be precisely controlled, which is why Horowitz and Hill called them a *"statistical bidirectional zener"* [46, p. 475]. As conduction occurs in the entire bulk of the device it is more robust than for example a Zener diode, where conduction can only happen at small active area of the semiconductor junction.

In LED drivers MOVs are typically found in the input filter stage on the line side. They are necessary to comply with EMI and electromagnetic compatibility (EMC) regulations .They require devices to be immune against specified disturbances coming from the power line, most importantly voltage surges [131, p. 215]. These devices can fail in spectacular ways as they are connected to a high energy source. Fires caused by MOV failures even lead to a revision of the requisite standards in the late 1990s [46, p. 476]. To limit the damage a MOV that failed in a short circuit mode and is connected between live and neutral can cause, it should be protected by an inline fuse with an adequate interrupting current rating. Some standards even require this type of protection [77, s. 7.2.5.1, 106, p. 36].

Although they are considered to be highly reliable and long-lasting components, MOVs do degrade over time. This degradation leads to an increase in leakage current at voltages below the device's threshold and can, due to the resulting resistive heating, cause thermal runaway and destruction of the MOV [13]. A continuous connection to an AC voltage – like in surge suppression applications as discussed above – has been demonstrated to have an accelerating effect on the MOV's degradation [115, 45, 126]. Exposition to high levels of humidity can cause the leakage current to rise even quicker [56, 72, 128]. It has been shown experimentally that the humidity induced leakage current is limited to the interface between the ZnO bulk and the MOV's housing rather than that moisture would penetrate the bulk of the device [62, 127]. Application of a DC voltage across the varistor as well as repetitive current pulses have also been shown to lead to an increase in leakage current [7, 75, 83]. A similar trend has been reported for MOVs that have been subjected to an AC voltage with noticeable distortion [6].

WE-EF ED100-66/700-1050/230-50-60/O-O

This is a medium power constant current driver designed for outdoor use with fixed output current and without a communication interface. Its double-layer PCB is made from high-quality FR-4 material and it has the most complex EMI filter circuit of all drivers tested. This filter circuit consists of two common-mode chokes and two MOVs. Still three of the five tested devices did fail and those that failed show a consistent failure signature. In all three devices the second of the two MOVs, marked RV2 in Figure 3.17, failed catastrophically. For one device this failure only occurred after it was removed from the experiment and tested for functionality under lab conditions. The device's case had been removed at that point, so that the experimenter could fully appreciate this rather violent failure mode as it unfolded right before his eyes.

The elaborate EMI filter circuit used in this driver is illustrated in Figure 3.17. This circuit is unusual not

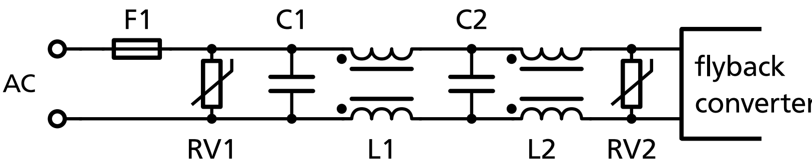

Figure 3.17: Schematic of the EMI filter circuit of the WE-EF ED100-66/700-1050/230-50-60/O-O. The topology is unusually complex, as two filter sections, each consisting of a common-mode choke, metal film capacitor and MOV, have been connected back to back.

only because it is composed of two filter sections with a common-mode choke, metal film capacitor and MOV each, but also because the components in the two sections are arranged in a different order. Most notably, the MOV RV2 is the last component in the filter chain. As outlined earlier, the purpose of MOVs in circuit is the suppression of high voltage surges coming from the power line. These energetic pulses should be attenuated as soon as they enter the circuit to protect all upstream components form further damage. Due to the high currents associated with these pulses even robust inductive components such as common-mode chokes can be damaged by them. It is for this very reason that an MOV is typically placed after the fuse but before all other filter components. As only the MOV sitting right next to the flyback converter failed in the experiments it is reasonable to assume that this position caused additional stress. If that stress is of either high frequency or of the common-mode type the two chokes and capacitors could attenuate it sufficiently to explain why the MOV RV1 did not fail during testing.

To confirm this theory a test setup was devised measuring the voltage across the varistor as well as the current flowing through it. A differential probe and current clamp are used to measure the voltage and current, respectively. To be able to synchronize the oscilloscope's trigger to the switching of the SMPS circuit the probe head of a magnetic trigger probe amplifier [130, pp. 37–40] is placed next to the main inductor. The test setup is shown in Figure 3.18a. First, the current through the MOV flowing during a cycle of the AC line voltage is measured. It is shown in Figure 3.18b. Although the voltage across the varistor follows a nice sine wave, the current flowing through it looks more like a pulsed signal modulated by said sine wave. This current flow is not caused by the applied AC waveform, but must rather stem from the switching of the SMPS circuit. This is confirmed by synchronizing the current measurement to the switching of the converter as shown in Figure 3.18c. Once the converter starts switching the current surpasses 30 mA peak to peak, constituting a significant stress to the component. It can be concluded that the MOV designated RV2 failed due to being subjected to a continuous stress through the current pulses injected into it by the SMPS circuit. The identical MOV RV1 is shielded by the common mode choke from these pulses and consequently did not fail during testing.

LUMNIUM 54H-120B-GM-0450

This medium power driver is a prime example of a cost optimized design. Its circuit board is single-sided and made from cheap FR-2 material. It uses a single stage, non-isolated topology. The PCB allows for a ripple removal circuit but the necessary components have not been populated. One device is tested in the 85 °C/85 % environment and it failed after 1273 h. The visual inspection finds several cracked metal film capacitors and a MOV showing signs of thermal runaway. A section of the PCB can be seen in Figure 3.19, showing two of the cracked capacitors as well as the damaged MOV.

The continuity check reveals that the input fuse has been triggered. Looking at the circuit diagram in Figure 3.20a it is obvious that once the MOV RV2 fails as a short circuit a very high current will flow from the

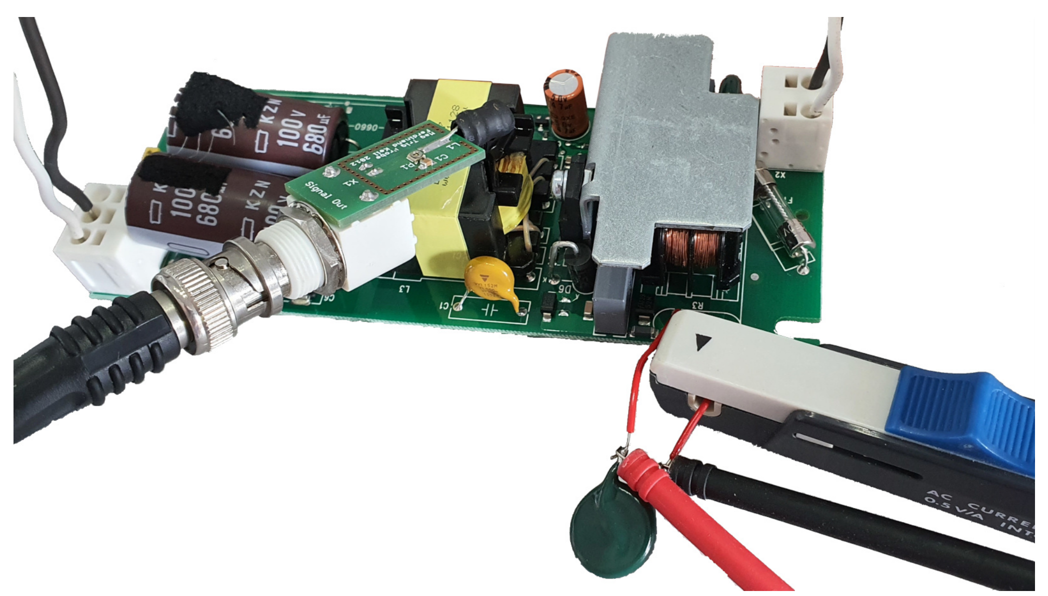

(a) Test setup to measure the voltage and current for MOV RV2.

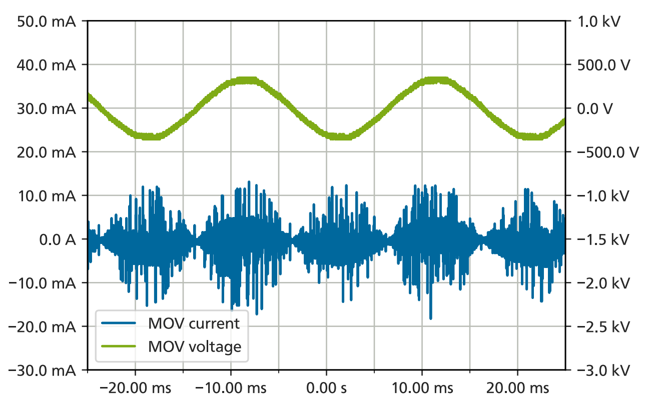

(b) Current through the MOV. Trigger set to line.

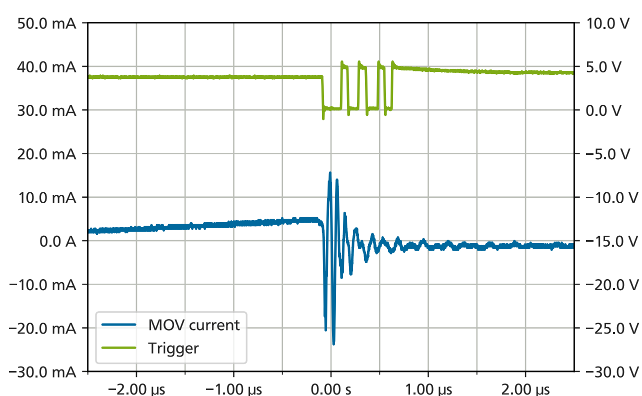

(c) Current through the MOV. Trigger set to SMPS switching.

Figure 3.18: Test setup for measuring the voltage and current at MOV RV2 of the driver WE-EF ED100-66/700-1050/230-50-60/O-O and the resulting measurement results.

line input. This current will in turn trigger the input fuse F1, rendering the device useless. The circuit is odd in that a second MOV is connected across the output of the bridge rectifier and right next to the inductor and switching transistor. This MOV is subjected to the rectified mains voltage in addition to the switching noise emanating from the transistor and inductor.

To determine whether the switching noise might have a detrimental effect on the MOV the voltage across the component and the current flowing through it are measured. The measurement results are shown in Figure 3.20. As the capacitance of the metal film capacitors connected at the output of the bridge rectifier is quite limited, the voltage across the MOV RV2 looks more than rectified sine wave than a DC voltage. At its peak it reaches about 333 V as can be seen in Figure 3.20b. This rectified sine wave causes a peak-to-peak leakage current of approximately 1.8 mA to flow through the MOV. However, if the oscilloscope is triggered on the switching of the SMPS circuit a much more significant current pulse surpassing 20 mA peak to peak can be measured. The waveform is shown in Figure 3.20c. It is once more reasonable to conclude that these current pulses accelerated the degradation of the varistor and thus caused it to fail.

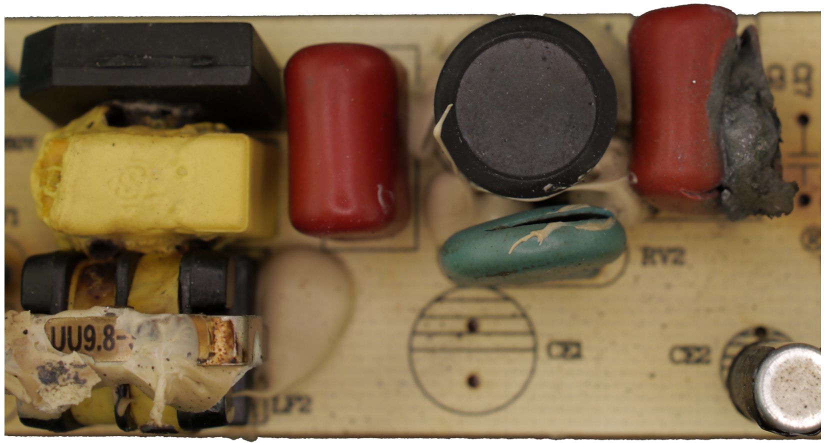

Figure 3.19: This section shows two metal film capacitors and an MOV that failed during the testing of the driver LUMNIUM 54H-120B-GM-0450 in an 85 °C/85 % environment. The failed MOV is identified to be the root failure cause for the device.

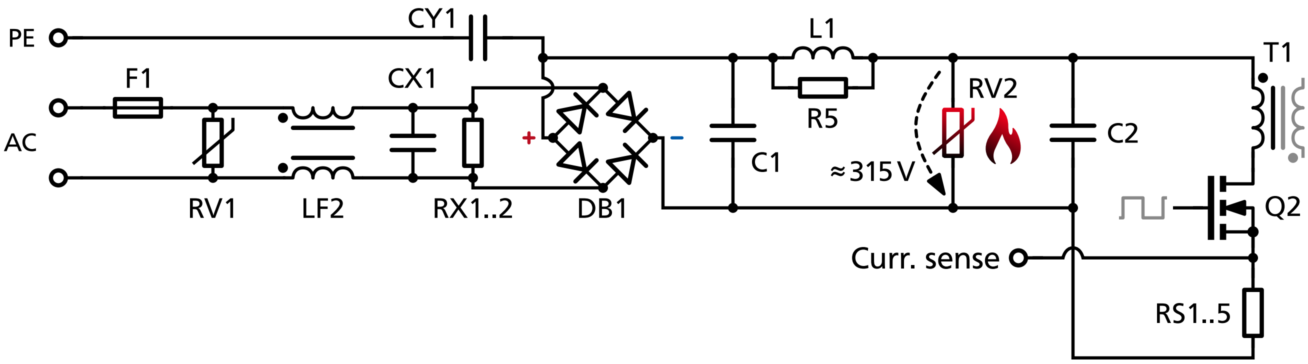

(a) Schematic of the driver from the line input to the switching MOSFET.

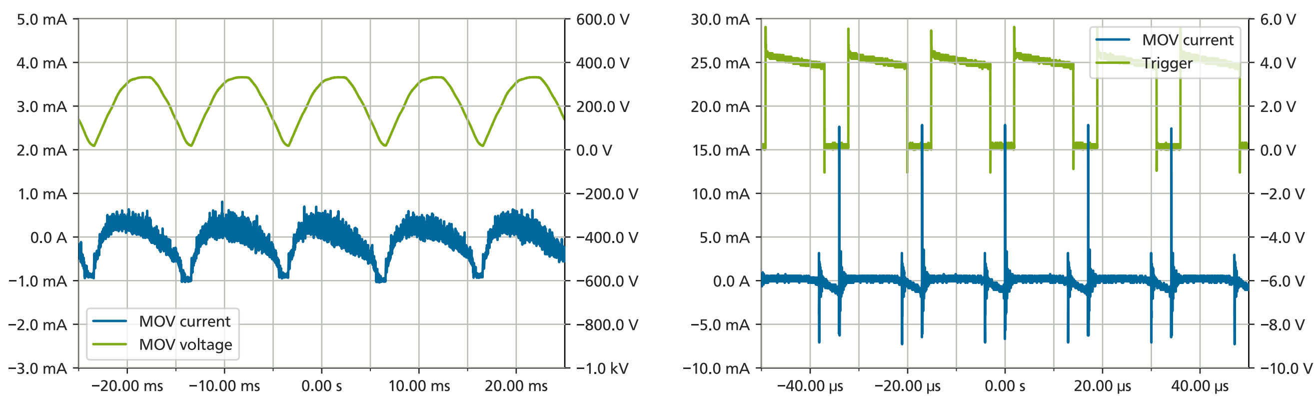

(b) Current through the MOV. Trigger set to line.

(c) Current through the MOV. Trigger set to SMPS switching.

Figure 3.20: Simplified schematic of the driver LUMNIUM 54H-120B-GM-0450 and measurement results for the MOV RV2.

3.2.4 MOSFET

Metal-oxide-semiconductor field-effect transistors (MOSFETs) are widely used in SMPS circuits as their favourable properties allow for very efficient designs. The most common circuit topologies use transistors like switches, meaning they are either turned completely off or on. Although the control of a MOSFET's gate is not trivial at high switching frequencies, modern power converters work at frequencies as high as several MHz. This allows for smaller energy storage components such as inductors and capacitors, which enables the very compact devices commonly used today.

A short is the most common failure mode for MOSFETs [80, s. 1.6]. The electrical breakdown between source and drain has been linked to the accidental triggering of the intrinsic bipolar transistor between these contacts [55]. Although modern devices are more robust, this failure mode still remains the most common [110]. Additionally, it has been demonstrated experimentally that MOSFETs get more susceptible to this type of breakdown with increasing temperature [5]. This temperature dependence can likely be explained by an increase of the body diode leakage current as well as an increase of the body region resistance with temperature, causing a voltage drop sufficient to trigger the intrinsic bipolar transistor Celaya et al.

Vossloh-Schwabe ECXd 700.149

The device tested in dry heat at 85 °C shows a different failure mechanism from those described in Section 3.2.2. A visual inspection does not uncover any obvious faults. Testing of the active components however reveals that the MOSFET in the constant current output stage has failed. The component is desoldered from the PCB and it is confirmed that a short circuit has formed between the source and drain connection of the MOSFET. It is assumed that the parasitic bipolar transistor in the MOSFET was triggered, causing a short-circuit and ultimately the failure of the tested device. This failure mode was effectively masked in the tests in damp heat, as the devices failed much earlier and due to different failure modes. The short-circuit in the MOSFET only manifested itself after more than 10 000 h, while no device lasted more than 6190 h in damp heat.

N/A LGM52W041P2

This medium-power driver from an unknown manufacturer has a fixed output current of 390 mA. It offers no advanced features and uses a simple single-stage SMPS topology. Its output is not galvanically isolated from the power line. The device V137 was tested in the 85 °C/85 % condition and failed catastrophically after 2019 h. Once its case is opened, intense burn marks on the backside of the assembly caught the eye. A detailed visual inspection shows that the six shunt resistors have burned out completely. An image of the section of the assembly containing these resistors is presented in Figure 3.21a. Also, one of the pins of the control IC U1 has burned off, leaving a smoke trail next to it. All other components, including the ripple removal stage at the output seem to be fine.

The continuity check however reveals a dead short between all pins of the main switching MOSFET Q1. After desoldering the component it is confirmed that a short has indeed formed inside of it. A simplified schematic of the device including all failed components is presented in Figure 3.21b. The rectified line voltage enters the circuit as V_{in} and then connects to the inductor T1. The failed switching transistor Q1 is controlled by the IC U1. The IC measures the current flowing through the inductor by means of the shunt resistors. The resistors show intense burn marks. As three components have failed catastrophically the root failure cause is not immediately obvious and an event tree analysis is conducted to identify it. Its result is shown in Figure 3.22.

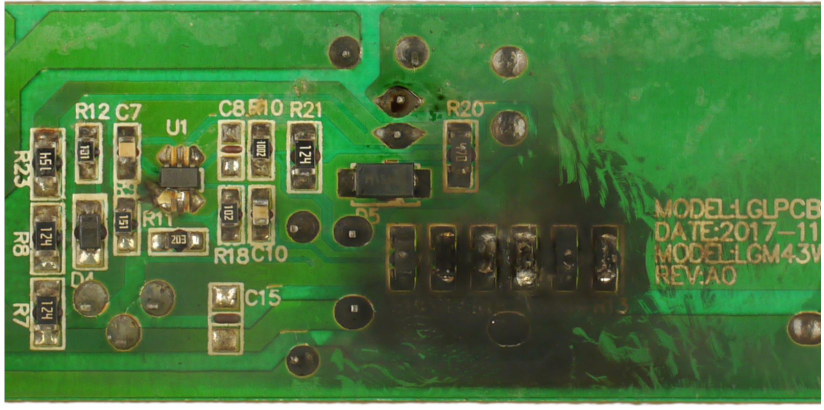

(a) Bottom side of the PCB of device V137. The damaged resistors and IC can be seen.

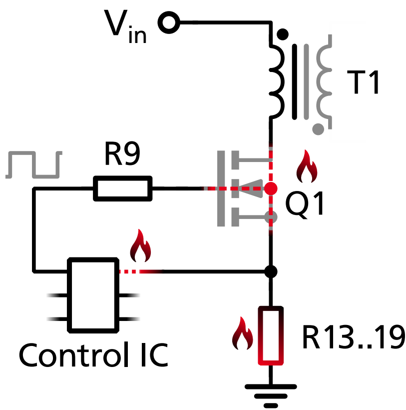

(b) Simplified schematic including the damaged components.

Figure 3.21: Bottom side of the failed device of driver type N/A LGM52W041P2 next to a simplified schematic. The component designators of the damaged components can easily be cross referenced between the schematic and the actual circuit.

First the two unlikely root causes will be discussed. The shunt resistors could have failed either as short or open. In case of an open no over-current event would have been triggered, so this can be set aside. If one or more of the resistors would have failed short this would likely lead to a chain reaction destroying all resistors. And if that failure happens while the transistor Q1 is conducting, a high voltage would be applied to the control IC on a pin that is designed to only handle the miniscule feedback voltage from the shunt resistors. It is reasonable to assume that this could cause the destruction of the IC U1. However, it would not explain the damage to the transistor. Due to its high thermal mass and the added heat sink even the high current flowing until all resistors would have burned out is unlikely to have an effect on the transistor. Thus, this is an unlikely root cause.

That a malfunction of the control IC U1 would have caused the failure is similarly unlikely. If it had driven the transistor Q1 to conduct permanently this could have caused the destruction of the shunt resistors and subsequently fused open the current measurement pin of the IC. But it is unlikely that this would have caused damage to the MOSFET for the same reasons that were mentioned previously.

This leaves the failure of the MOSFET Q1 to be the main culprit. A failure of this component due to thermal runaway would lead to an ensuing over-current event which in turn would destroy the shunt resistors. As discussed before this could cause the destruction of the control IC U1. As a short was measured between all pins – including the gate connection – the current that lead to the destruction of the chip could have entered the device through either the gate control or the current feedback pin. However, as the gate resistor R9 shows no signs of damage it can be concluded that the current entered through the current feedback pin. This is no surprise, as this pin would expect only relatively small voltages during normal operation of the device. To conclude, it is reasonable to assume that this driver failed due to the breakdown of its MOSFET, too. Given that the transistor even has been attached to an aluminium heat sink, its failure might have been caused by a defect introduced during manufacturing or assembly.

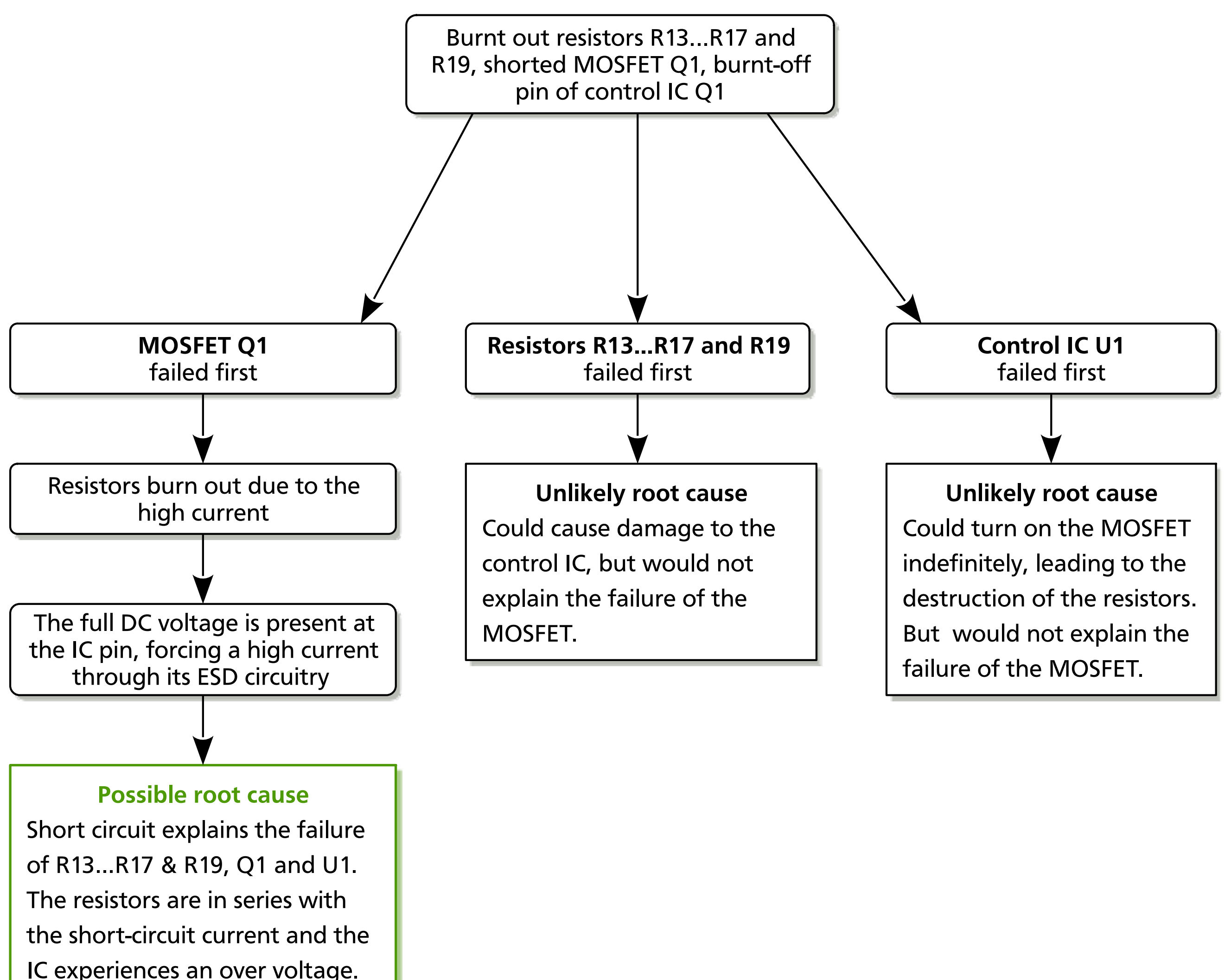

Figure 3.22: Event tree analysis of the failure of device V137.

Philips Xitanium 9290 008 818

This low-power driver's output current can be set by connecting an appropriate resistor. Besides of this industry standard interface it features a two-stage topology. Its output is galvanically isolated from mains through the coupled inductor used in the constant current output stage. The device V097 that was tested at 85 °C/85 % failed catastrophically. Unfortunately, the time of the failure cannot be determined. To reduce the outside dimensions of the device two sub-assemblies are used in the driver. One contains the components of the power stage like transistors, capacitors and inductors and is made from FR-2 material. The other one carries the control electronics and the density of the component placement is significantly higher on its two layer PCB made from FR-4.

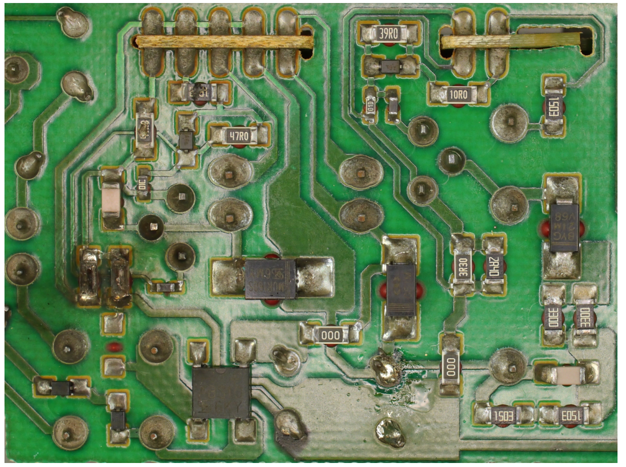

(a) Power stage.

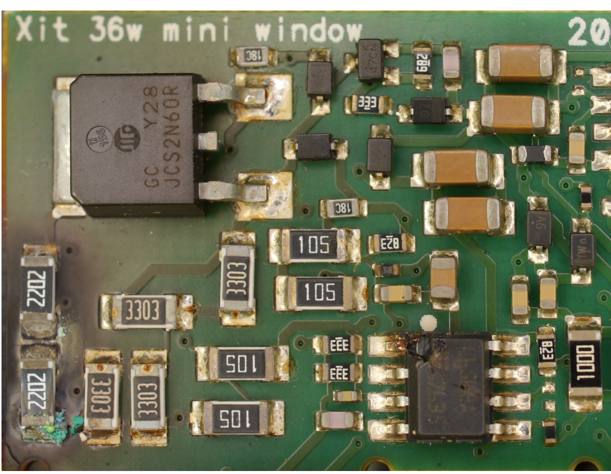

(b) Control electronics.

Figure 3.23: Damaged components on the two sub-assemblies of the failed device V097. Note that the two damaged resistors on the left side of the control PCB did play a role in the failure of the device.

The visual inspection of the failed device reveals burn marks on several SMT resistors on the bottom side of the power stage assembly as well as on an IC package on the control electronics board. The two damaged PCBs can be seen in Figure 3.23. The following continuity check shows that the switching MOSFET of the PFC stage has failed with a short between all of its contacts. The component is desoldered and the finding confirmed. This case presents itself with several failures, requiring a more in-depth analysis to determine the root failure cause. Luckily though, this failure pattern is identical to the one discussed in Section 3.2.4. The conclusion should therefore be the same as well, namely that the failure was triggered by a short that has formed between the contacts of the switching transistor.

3.2.5 Metallised Film Capacitor

These capacitors get their name from the metallised film being used in their construction. The very thin layer of metal forms the electrodes of the capacitor while the plastic film is its dielectric. The application of the metal on the plastic is usually achieved through vapour deposition. They also exhibit so called self-healing: if a short between the electrodes would happen to form due to a pinhole in the plastic film, the resulting short current would evaporate the metallised film in that area and thereby remove the short [109, p. 113].

Metallised film capacitors are commonly used to suppress the EMI and thus preventing it to reach the mains connection point. In this application they are placed across the live leg and either the neutral leg of the mains or protective earth. As they are permanently biased and supplied by a high energy source these capacitors must adhere to strict high safety standards [41]. It is especially important that, if they fail, they fail in a safe manner, without putting users at risk or heating up to the point of combustion.

However, the application of metallised film capacitors is not limited to the EMI filter at the mains input of the driver. As aluminium electrolytic capacitors are considered to be one of the components of an SMPS with a comparatively high failure rate [61], efforts have been underway to replace them with lower capacitance film capacitors [78, 124]. Due to this trend, metallised film capacitors are now being increasingly used in SMPS circuits and for different purposes.

Although they are considered to be quite robust, metallised film capacitors can still fail. After a failure they present either an open or short circuit with almost equal probability [80, s. 1.6]. In the presence of heat and humidity, loss of electrode area due to self-healing or corrosion of the metal film can lead to an open circuit; dielectric breakdown or moisture absorption of the plastic film can cause a short circuit [40, 9, 125]. In EMI suppression applications a potential short will cause very high currents to flow, which will either remove the short in a destructive way or trigger the device's fuse or an upstream line circuit breaker. It is therefore recommended to always place a line fuse before any other component to guarantee that a short circuit current will be interrupted in a timely manner and potential damages are limited.

As these capacitors are rather susceptible to moisture many were severely damaged in the damp heat conditions. Albeit, degradation or complete failure of one or more metallised film capacitors did not necessarily cause failure of a tested device, due to the fact that most them are being used in the EMI filter on the line side of the driver. The EMI filter, while being essential for a given driver design to pass certification to the applicable standards, is not necessarily needed for proper operation of the circuit. Thus, many devices continued to operate even after most if not all of their metallised film capacitors had failed.

N/A CLNC65W042L

This medium power driver from an unknown manufacturer shows all the typical signs of a cost optimized design: it uses a single sided FR-2 board and a single stage topology. The latter is surprising for a design with a rated output power of 65 W, but makes sense from a cost saving perspective. The data sheet specifies a PF in excess of 0.95, which could be verified during testing. This goes to show that a careful design can alleviate the need for a PFC stage even at this power level.

One device is tested in the 85 °C/85 % environment and failed after 931 h. The site of the failure is shown in Figure 3.24. It is immediately obvious that the two metal film capacitors were badly damaged during the experiment. Both show cracked casings and partially charred blobs of molten material have exited them. In the side view the cause of the failure can be clearly seen: some of the molten innards of one capacitor have run beneath the bridge rectifier where it shorted its pins. As this plastic lava is conductive – due to it containing the metal of the end contacts of the capacitor as well as the metal layers forming the electrodes –

it shorted the pins of the bridge rectifier. This causes the line breaker to trip, preventing further damage. The device's fuse however did not blow.

The degradation of of the metal film capacitors on the primary side of the driver circuit is noticeable in the acquired data. Figure 3.25 illustrates how this degradation causes an increase of the measured power factor over time. This effect is due to the decrease in capacitance and increase in ESR of the capacitors, which in turn reduces the reactance the capacitors present. The real power consumed by the driver stays almost constant as indicated by the plot showing the primary side current. Therefore, as reactance decreases and real power stays constant the resulting power factor increases over time. This effect was noticed with all drivers that have metal film capacitors on the primary side of the circuit.

This goes to show that although metal film capacitors in many cases might not be essential to the operation of an LED driver, they can trigger a secondary failure mode that leads to the untimely demise of the device as a whole.

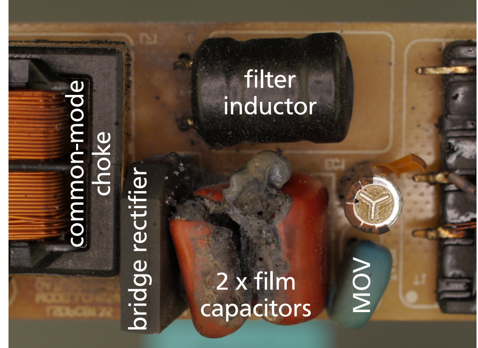

(a) Top view with component labels.

(b) Side view.

Figure 3.24: PCB of the device V149 showing two badly damaged film capacitors. Connection to mains is coming from the left side, the main converter can be found to the right. Figure 3.24b shows that molten debris from one of the caps made its way between the pins of the bridge rectifier.

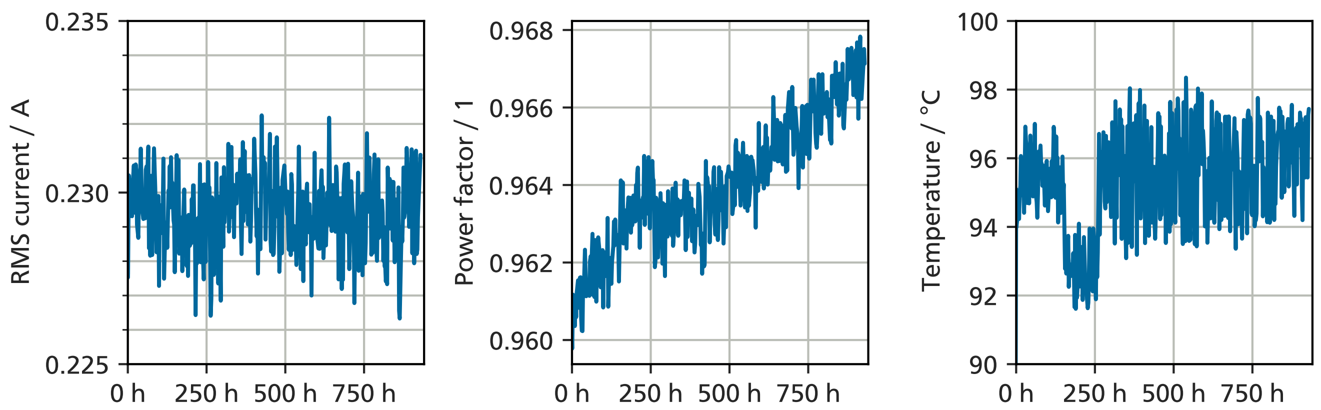

Figure 3.25: Plots showing the measured RMS current, power factor and temperature for the device V149. The power factor increases over time, while temperature and primary side current stay almost constant.

OSRAM OTi DALI 90/220-240/1A0 LT2 L

This OSRAM branded medium power driver is high-end both in terms of functionality as well as materials and components. It features a programmable output current and can be controller remotely over a DALI bus interface. The circuit uses a two-stage topology and is built on a multilayer FR-4 PCB. Still, the device V065 tested in 85 °C/85 % failed after 2098 h. Its PCB is presented in Figure 3.26. The visible damage is limited to several cracked metal-film capacitors.

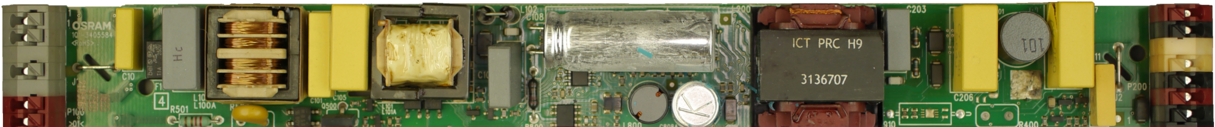

(a) PCB of device V065 after testing.

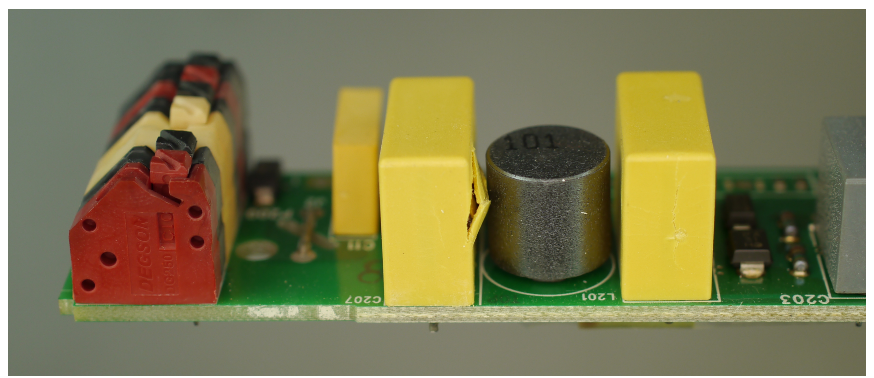

(b) Detail showing the cracked metal-film capacitor C207.

Figure 3.26: PCB of the device V065 after testing in 85 °C/85 %. The damaged capacitors C206 and C207 can be seen surrounding the grey cylinder in the center of the detail image. Both feature cracks in their case, but the damage to C207 is the most drastic.

No additional fault is uncovered by a detailed inspection. The input fuse has not been triggered. To test the auxiliary power supply the circuit was powered up and its output voltage measured. However, this too did not reveal an issue. An hypothesis of the possible failure mode could only be formulated after the recorded electrical data is evaluated, an selection of which is presented in Figure 3.27. The primary side related measurements such as the RMS current and power factor shown the typical signs of failing metal-film capacitors in the input filter section. Additionally, an almost exponential increase over time of the output current ripple can be observed. It is therefore hypothesized that the failure of the output decoupling capacitors finally lead to the failure of the device as a whole. To confirm that the capacitors C206 and C207 have both failed they are desoldered and their capacitance and ESR measured. Their capacitance is measured to be 60.5 pF or less with an ESR of 1.3 MΩ or more. In comparison to the value of their brand-new counterparts of about 560 nF and 75 mΩ it becomes clear that these capacitors have failed completely.

To test this hypothesis a brand new driver of the same type and from the same manufacturing lot is modified by removing the two output decoupling capacitors, designated as C206 and C207. The device is tested before and after the modification. Without these capacitors a loud high-frequency noise coming from the circuit's inductors can be heard. This indicates an instability or oscillation in the output stage's control loop. While all other parameters were kept constant – including the settings of the electronic load at the output – the output power fell from 74 W to 67 W and the output current from 620 mA to 540 mA. Although an instant

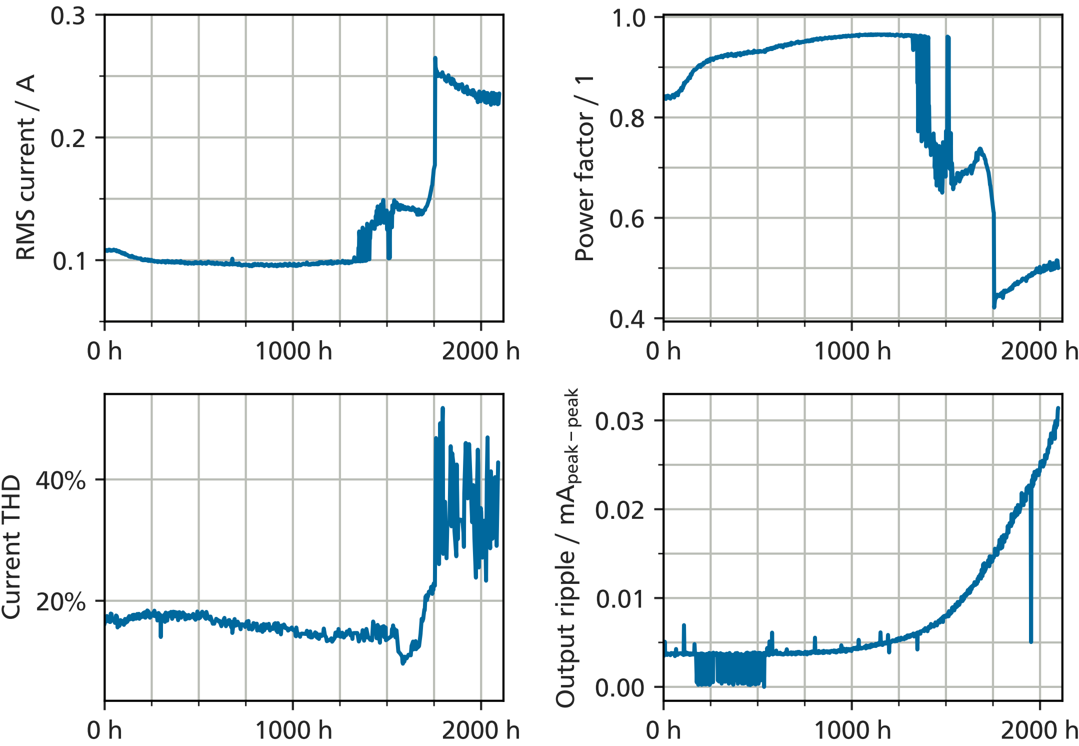

Figure 3.27: This data was recorded during the testing of V065. Shown here are the RMS input current, power factor, current THD and output current ripple. The slow increase in current ripple proves that the output decoupling capacitor's performance degraded significantly over the course of the experiment.

catastrophic failure is not observed it can be shown that the failure of these two capacitors causes an abnormal mode of operation. It is reasonable to assume that this would, after some time, lead to the failure of the device through some other – so far undetermined – failure mode.

3.2.6 Diode

The humble diode is one of the essential building blocks of any off-line power supply. In SMPS designs one would first encounter diodes as part of the rectifying circuit converting the AC input to DC so that the converter can deal with it. The diodes used for rectification only have to deal with comparatively slow signals, namely the 50 Hz or 60 Hz sine wave coming from mains. However, they have to withstand rather high voltages and – depending on the power rating of the driver – comparatively high currents as well. Diodes are also commonly used in most switch-mode converter topologies. Here they can be replaced with actively controlled transistors to increase efficiency at the cost of added circuit complexity.

Diodes are considered to be quite reliable circuit components. Military handbook 217 lists their baseline failure rate as $\lambda_b = 0.0010$ failures/10^6 hours, compared to 0.060 failures/10^6 hours for MOSFETs [103]. When diodes fail, they fail as short in 51 % and as open in 29 % of the observed failures. The remaining 20 % show a noticeable parametric change [80, s. 1.6]. The open failure mode is caused by a failure of the connection to the semiconductor die at the heart of the diode, for example due to a bond wire lift-off or thermal overload following a short circuit failure [133]. Several mechanisms can lead to a short circuit failure of a diode, namely [133]:

- static high voltage breakdown,
- catastrophic increase of leakage current,
- snappy recovery,
- reverse recovery dynamic avalanche breakdown,
- thermal overload.

Static high voltage breakdown can easily be avoided by adhering to proper design margins when choosing a diode. It is therefore considered to be an unlikely failure mode. Snappy recovery and dynamic avalanche breakdown have been connected to high switching speeds. These are only present in the SMPS part of an off-line LED driver circuit. The effects would not be observed in the bridge rectifier following the mains input. However, the source of the necessary current pulse can also be extrinsic. Electrostatic discharge (ESD) events have been shown to induce failures that are similar to the two previously mentioned mechanisms [30].

Philips CertaDrive 60W 360mA 170V 230V

This simple medium power constant current driver uses a single stage topology and lacks a communication interface. Its PCB is made from FR-2 material. The used electronic components have been cost optimized as well. A single device is tested at 85 °C/85 % and failed after 1355 h with an unusual failure signature. The first visual inspection reveals that its PCB track fuse has opened and an SMT resistor on the bottom side shows burn marks (see Figure 3.30a). The following continuity check reveals that the rectifying diode D13 has failed as a short circuit. This is checked again after the component has been removed from the circuit.

To identify the root failure cause the schematic of the input filter of the circuit is reverse engineered up to the bridge rectifier. The result can be seen in Figure 3.28. The burnt resistor is shown in the bottom center of the schematic. Given that the inductor L4 is connected in parallel with this resistor it was suspected to have failed as well. A thorough examination of this component proves that it has failed as open circuit. An inspection under a microscope reveals a pin hole burn mark in the epoxy body of the inductor. All failures have been marked in Figure 3.28 as well.

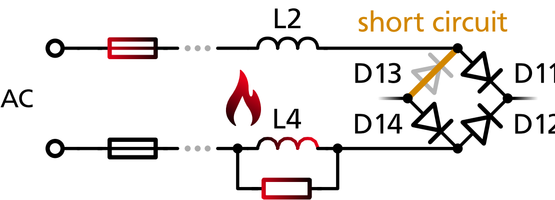

Figure 3.28: Reverse engineered schematic of the filter section of the driver Philips CertaDrive 60W 360mA 170V 230V. Parts of the circuit have been left out as they were neither damaged nor are they conducive to the understanding of the failure.

The question remains which of the components started the succession of events that lead to the failure. The analysis shown in Figure 3.29 lays out the reasoning that identified diode D13 as the root failure cause. The failure of either the inductor L4 or the resistor would not be sufficient to explain the total damage the device suffered. However, once the diode D13 would have failed as a short circuit, a high current would flow every half cycle of the mains sine wave[2]. Being supplied by the power line this short circuit current can reach tremendous levels, which in turn explains the damage done to the inductor and resistor as well as the triggering of the fuse.

[2]During the other half cycle of the sine wave the current would be blocked by the still intact diode D14.

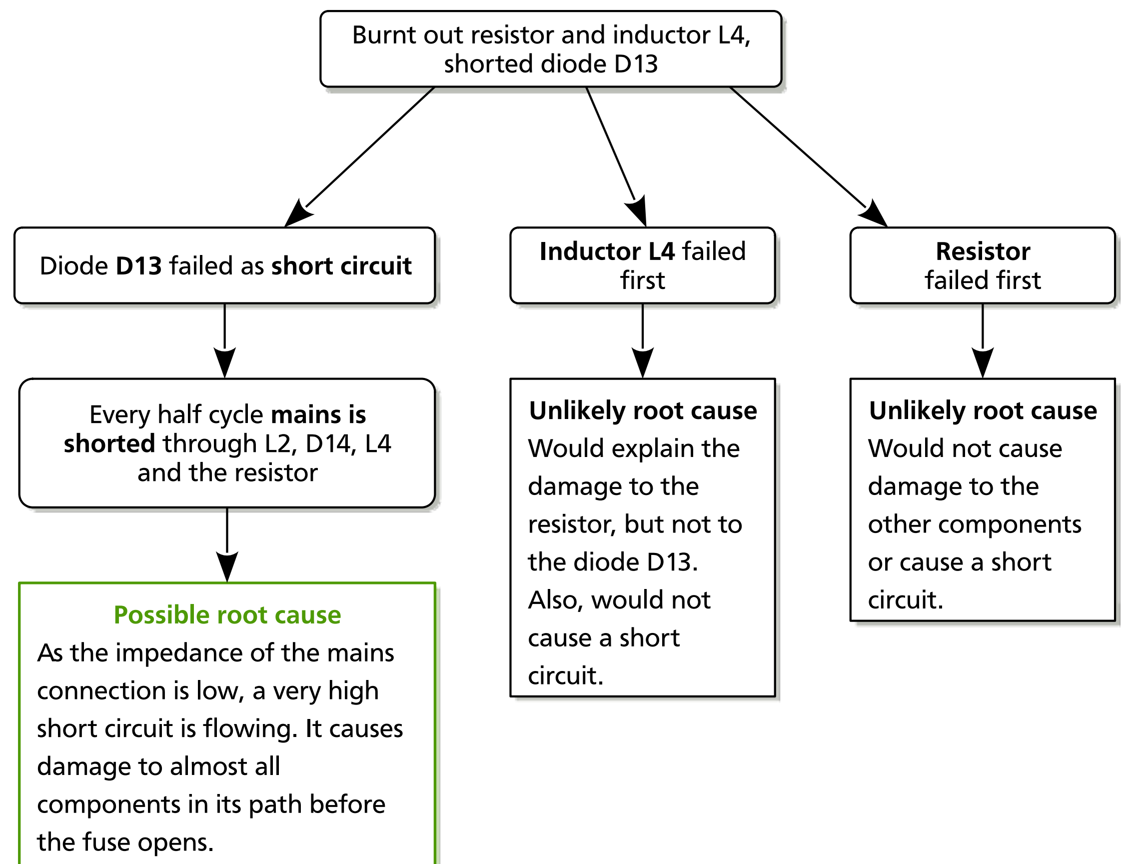

Figure 3.29: An event tree analysis is conducted to identify the root failure cause for the driver Philips CertaDrive 60W 360mA 170V 230V. It is clear, that only the failure of diode D13 explains the observed failure signature.

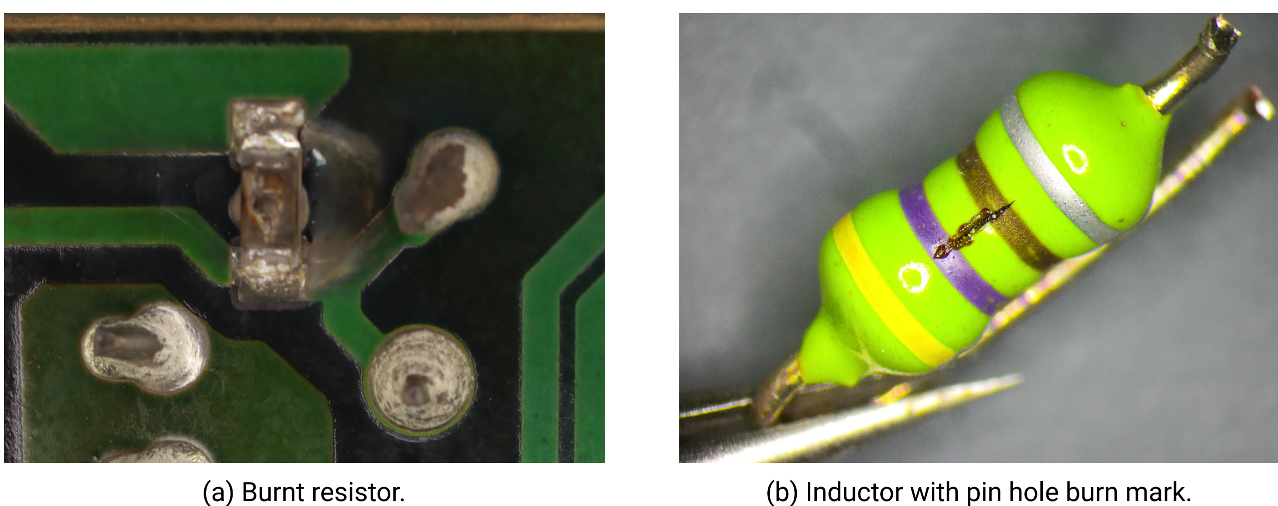

(a) Burnt resistor.

(b) Inductor with pin hole burn mark.

Figure 3.30: Detail images showing the damaged components on the driver Philips CertaDrive 60W 360mA 170V 230V. The inductor shown in the right image is connected in parallel to the resistor on the left. The burn mark in the inductor is approximately 2 mm long and 150 µm wide.

3.2.7 Inductor

Inductors or coils come in many different shapes and sizes. They consist of wire, usually copper, wound on a core or bobbin. The core can be made from a variety of materials with different magnetic properties, such as ferrite, iron powder or just air. An inductor can store energy in its magnetic field or dissipate it in its core. The specific design of an inductor – namely the type of wire, winding technique and core construction – determines its application. In LED drivers inductors are used to store energy or to suppress unwanted signals. They are often the most prominent component on the assembly in the form of a coupled inductor that is part of the main SMPS circuit. Or the can be found near the line input where they suppress disturbances coming from the grid and prevent electrical noise generated by the driver to couple back into it.

In both cases the inductor is a vital part of the circuit and its demise will lead to a total failure of the device. The good news is that inductors are generally considered to be quite robust components. Military handbook 217 gives a baseline failure rate of just $\lambda_b = 0.000\,030$ failures/10^6 hours for fixed value inductors, which is about thirty times less than the one for diodes. Still, one failure caused by an inductor is observed during testing.

N/A LGM22W016P2

This device is representative of the class of low power and low cost off-line drivers. It features a single stage topology on a single-sided FR-2 circuit board. The device V134 is tested in an environment of 85 °C/85 % and failed after 2299 h.

As neither the THT components on the top side of the PCB nor the SMT components on its bottom side show any discernible damage a detailed investigation of the failure is undertaken. The continuity check reveals that although the fuse has not been triggered inductor L1 has failed as open circuit. The component is desoldered and inspected under a microscope after its protective heat-shrink tubing has been removed. Under magnification the failure cause can quickly be identified: the magnet wire is missing a section near one of the pin terminals. It is evident that the wire has fused open as metal beads have formed on both sides of the wire ends. Unfortunately, the current rating of the inductor can not be determined. Given that neither the fuse was triggered nor any other component shows any damage, an over-current event can be ruled out as the cause of the failure. Looking at the magnet wire under high magnification signs of corrosion can be seen, such as the characteristically bright green copper oxide. It is likely that the wires protective lacquer was damaged during production or assembly which in turn allowed contaminants to reach the bare copper surface. This lead to corrosion during the testing at a high relative humidity. The wire's resistance increased over time as the corrosive process ate away ever more of its copper. This finally lead to a thermal runaway event in which the wire fused open, causing the total failure of the device. Although the evidence is circumstantial, this is another failure mode that can be linked to surface contamination.

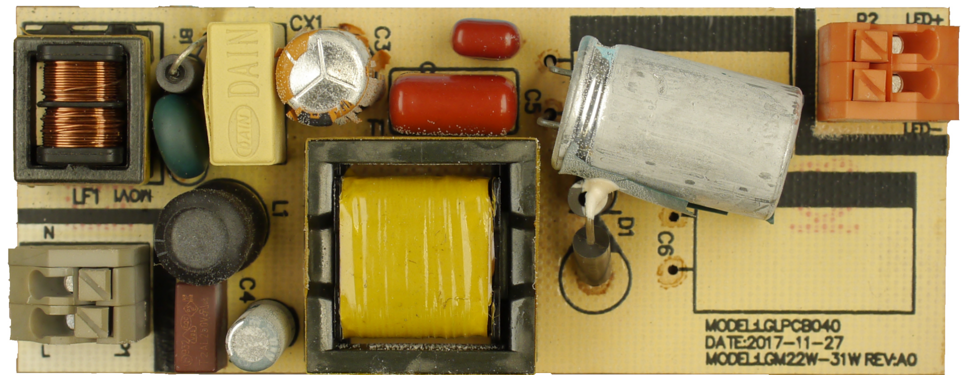

(a) Top side of the tested PCB.

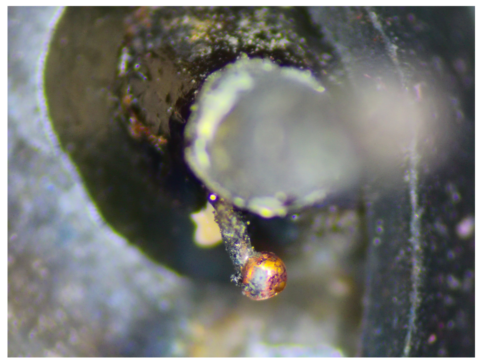

(b) Pin 1 of inductor L1.

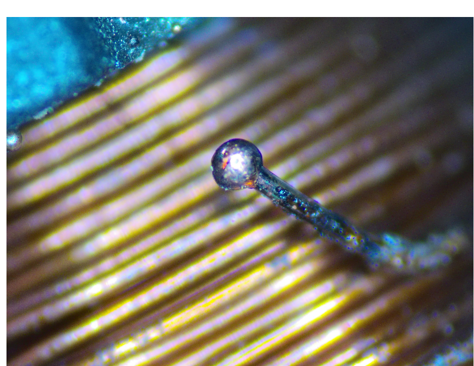

(c) Winding of inductor L1.

Figure 3.31: The top side of the PCB of device V134 shows no serious damage. However, under the microscope the fused open winding of inductor L1 can clearly be seen. Figure 3.31c also shows signs of corrosion as evidenced by the bright green copper oxide.

3.2.8 Resistor

Resistors have to be the most foundational electronic component. They inadvertently are part of almost every circuit as they are either introduced deliberately or as a parasitic effect of other components. As even wiring and circuit board tracks present some resistance to the current it is close to impossible to avoid resistors. This section focuses on resistors as components. These come in a variety of packages, but the axially leaded THT packages and chip size SMT packages are the most popular. In a typical off-line LED driver a bunch of resistors can be found fulfilling different roles in the circuit: as shunt resistors they measure the current through an inductor or transistor; in a voltage divider connected to a feedback pin of the main control IC they configure some kind of limit; or a resistor in series with a capacitor forms a so called snubber circuit, suppressing unwanted oscillations at critical circuit nodes to pass EMC requirements.

Just like inductors, resistor are commonly considered to be rather robust circuit components. Military handbook 217 gives a failure rate of $\lambda_b = 0.0037$ failures/10^6 hours for chip size film resistors, which is two orders of magnitude higher than the value listed for inductors. This goes to show that resistors are indeed robust but not infallible. The handbook also lists an environmental factor of $\lambda_E = 12$ for maritime applications[3], hinting at a detrimental effect of water on the reliability of resistors. According to Martin, fixed film resistors fail as open in 59 % of cases, while parametric changes are the second most common failure mode at 36 % of cases [80, s. 1.6]. The remaining 5 % fail as short.

Although many of the observed failures did include damaged resistors, only one case was identified where resistors were the principle cause of failure. This speaks for their robustness as components.

Vossloh-Schwabe ECXe 350.298

The Vossloh-Schwabe ECXe 350.298 is a medium power driver with no advanced features. Its output current is fixed at 350 mA. Two devices are tested in the 85 °C/85 % environment. The devices V123 and V124 failed after 419.25 h and 573 h, respectively. Unfortunately, no failure cause can be determined for driver V124.

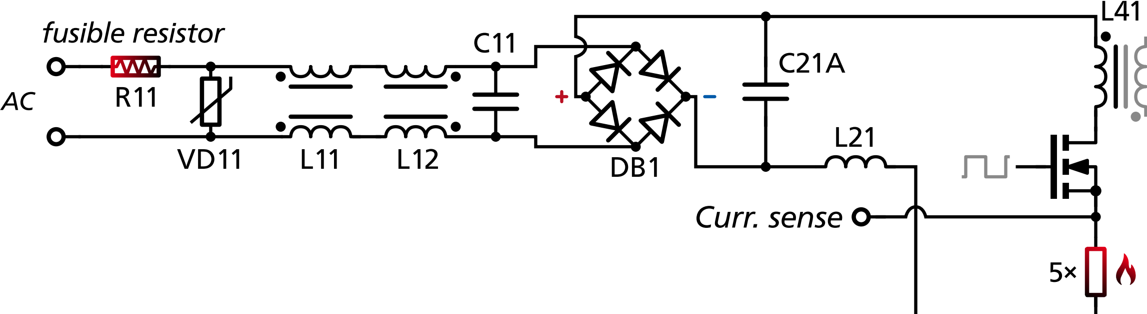

Figure 3.32: Schematic of the driver Vossloh-Schwabe ECXe 350.298 from the mains input to the primary side of the SMPS circuit.

The preliminary visual inspection does not reveal any obvious damage to the device V123. The continuity check finds that the fusible resistor R11 at the line input of the device has failed open. But not until the assembly is placed under a microscope the damage to the shunt resistors can be identified. The five shunt resistors are connected in parallel and convert the current flowing through the switching MOSFET and the

[3]The factor presented here is for the N_S environment, which is described as *Naval, Sheltered*. This is a conservative choice. The factors for harsher environments like *Naval, Unsheltered* or – at the extreme end – *Cannon, Launch* tend to be much higher.

inductor to a voltage that the control IC can measure. In the simplified schematic which is presented in Figure 3.32 the failed components have been highlighted.

It goes without saying that a failure of the fusible resistor R11 would cause a failure of the device. However, this would not explain why the shunt resistors were damaged as well. These are likely the root failure cause. Four out of five resistors did fail as open circuit. If – preceding the complete destruction of the resistive element – one or multiple resistors had experienced a sudden drop in resistance, this would have caused an increase of current through the transistor and inductor due to the feedback loop controlled by the IC. This is because a drop in resistance would lead to a drop in the voltage measured across the shunt resistors, feigning a drop in current to IC which the IC's control loop would counter by in turn increasing the current. Once the current surpasses the level that the fusible resistor R11 can pass safely, it is fused open and the device has failed. It is therefore reasonable to conclude that a parametric failure of one or more of the shunt resistors started the chain reaction that finally lead to the catastrophic failure of the device.

4 Discussion

This chapter will subject the experimental results presented in Chapter 3 to a more detailed analysis.

In the first section the two physical models introduced in Section 2.6 are applied to the accelerated failure time data to estimate their lifetime at different environmental conditions. The estimated lifetimes are compared to the ones guaranteed by the manufacturers of the drivers. This approach is then extended to drivers with right-censored lifetimes. Lastly, to enable a more intuitive understanding the estimated lifetime of these drivers is calculated for a selection of geographical locations.

The second section presents the results from the survival analysis. The properties of the drivers are used to build a set of Cox PH models. The best model is selected and its choice of parameters is discussed. Finally, the last section summarizes what can be done to improve the reliability of future off-line LED driver design based on the findings from the failure mode analysis and the two model-based approaches.

4.1 Lifetime Extrapolation With Physical Models

Section 2.6 introduces two physical models. These models establish a mathematical relationship between the stresses used in the accelerated lifetime test and the acceleration factor. Tests at three environmental conditions are required to estimate the parameters of a suitable model for an experimental design including both temperature and humidity as stresses. Keeping in mind that each data-point is a device tested until it fails, it becomes obvious that the experimental effort required is enormous. The meagre output of the experiments undertaken for this work – only three driver types out of fifteen failed at each of the three tested environmental conditions – is testament to this.

The collected data makes it possible to fit the two models described in Section 2.6 for these three driver types. This extends an analysis of the same data that was presented in an earlier work [149]. The lifetimes of the DUTs for the three types at the three conditions are listed in Table 3.1. The fit of the Peck and Intel model is perfect for each driver type. This comes as no surprise, given that both have three parameters and there are three data points for each of the three driver types. The coefficient of determination was calculated for each combination of driver and model. It was found to be one for every combination, indicating a perfect fit.

The estimated model parameters are presented in Table 4.1. The activation energy E_A is almost identical between the Peck and Intel model. This agreement builds confidence in the results of the fit. Additionally, the values lie in a range of approximately 0.4 to 0.9 eV, which is comparable to what has been found in previous works [50, 83f.]. The difference in activation energy between the three driver types can be explained by the different failure mechanisms that were observed.

The results for LG LLP 150W 0.7A 125 280Vdc PISE-A150D contradict the expected behaviour for both models. For this driver type both models predict the lifetime to decrease with decreasing level of relative humidity, as evidenced by the parameter n having a positive value and B a negative one. Although there are failure mechanisms that get accelerated with decreasing relative humidity (e.g. the evaporation of the liquid

electrolyte in aluminium electrolytic capacitors) that is a highly unlikely explanation for the observation at hand. Unfortunately, this driver type has been potted with a bitumen-like substance making failure analysis all but impossible. Although an unrecognized multitude of failure mechanisms at the three environmental conditions would explain this oddity, it can not be demonstrated forensically. Unfortunately, that means that this driver will have to be excluded from further analysis.

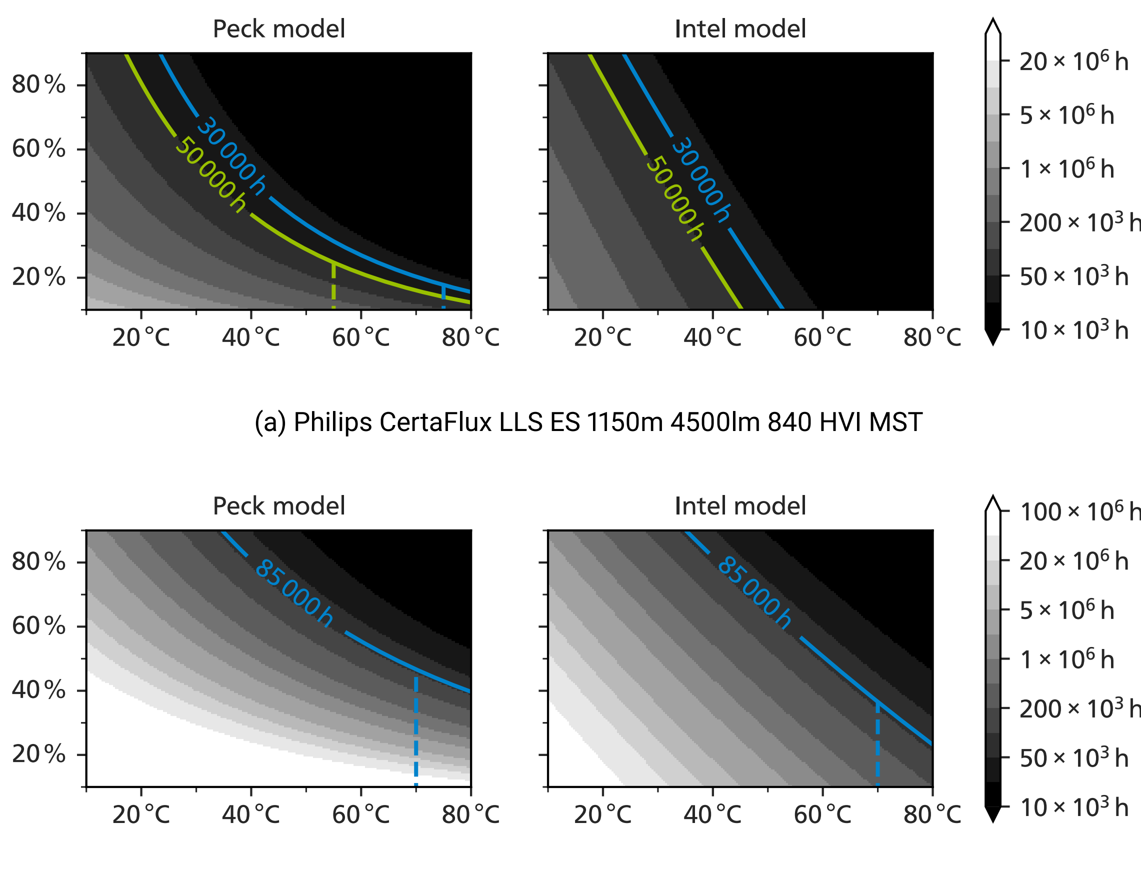

(a) Philips CertaFlux LLS ES 1150m 4500lm 840 HVI MST

(b) OSRAM OT 40/120-277/1A0 4DIMLT2 E

Figure 4.1: Intensity plots visualizing the Peck and Intel model after fitting them for two drivers with complete data. The lifetimes specified by the manufacturers in the data sheets are marked with solid lines. A dashed line indicates the respective temperature limit for each lifetime.

As both models are a function of two variables, namely temperature and relative humidity, a three dimensional plot is required to visualize them. The chosen plot combines an intensity plot with fixed boundaries with a contour plot. The plot is supposed to give a graphical answer to the question, *does the driver live up to the manufacturers specifications?*. Driver manufacturers include lifetime specifications in their data sheets consisting of a value in hours and the maximum temperature at which this lifetime is guaranteed. They regularly specify more than one lifetime value. The lifetime guaranteed by the manufacturer has been drawn as a solid line in the plot. The maximum temperature for this lifetime is marked by a dashed line that intersects the respective solid line. The possible combinations of temperature and relative humidity associated with this lifetime can be read from the plot by following along the solid line. The temperature-humidity combinations in the area defined by the solid lifetime line and the dashed temperature line are all covered by

Table 4.1: Parameters for the Peck and Intel model after fitting them for multiple drivers. The data available for the last three drivers contained right-censored lifetimes. The parameters shown have been calculated using the end of the test as the time of failure.

Manufacturer	Manufacturer part number	Note	Peck model			Intel model		
			A	E_A / eV	n	A	E_A / eV	B
LG Innotek	LLP 150W 0.7A 125 280Vdc PISE-A150D		6.06×10^{-12}	0.448	3.97	5.78×10^{-6}	0.439	−0.049
OSRAM	OT 40/120-277/1A0 4DIMLT2 E		4.68	0.882	−5.21	6.64×10^{-8}	0.894	0.064
Philips	CertaFlux LLS ES 1150m 4500lm 840 HVI MST		0.0268	0.604	−2.156	1.51×10^{-5}	0.609	0.027
BAG	LCS130-70FX-30/220-240	*	1.55	1.070	−6.336	4.37×10^{-10}	1.085	0.078
OSRAM	OTi DALI 60/220-240/550 D LT2 L	*	848	0.664	−4.641	8.58×10^{-5}	0.675	0.057
Vossloh-Schwabe	ECXd 700.149	*	0.935	0.768	−3.919	1.16×10^{-6}	0.777	0.048

* Dataset for this driver contained one right-censored lifetime.

the manufacturer's lifetime specification, meaning that the guaranteed lifetime will be reached or exceeded. Of special interest is the relative humidity at the point at which the solid and dashed lines meet. If this value exceeds 25 % at temperatures of 60 °C or more[1], the driver will outlast the manufacturer guaranteed lifetime in even the harshest outdoor conditions. Finally, the bounded greyscale intensity grading makes it possible to see which temperature-humidity combinations are associated with lifetimes higher and lower than those specified by the manufacturers.

The resulting plots for the drivers OSRAM OT 40/120-277/1A0 4DIMLT2 E and Philips CertaFlux LLS ES 1150m 4500lm 840 HVI MST are presented in Figure 4.1. A trend common between both drivers is that the Peck model predicts longer lifetimes at low humidities when compared to the Intel model. Which of the two models is closer to reality cannot be decided based on the data available for this work.

Looking at Figure 4.1b showing the extrapolation results for the driver OSRAM OT 40/120-277/1A0 4DIMLT2 E it is clear that this type will outlast the manufacturer guaranteed lifetime of 85 000 h at a maximum temperature of 70 °C at humidity levels of 50 % or less. The results for the Philips CertaFlux LLS ES 1150m 4500lm 840 HVI MST on the other hand show a much more limited lifetime. According to Figure 4.1a the manufacturer guaranteed lifetime of over 30 000 h at 75 °C and more than 50 000 h at a temperature of 55 °C is only reached in rather dry environments.

Valuable insight into the performance of a device in the field can be gained by fitting a physical accelerated lifetime model to data from an accelerated lifetime test and using it to extrapolate. The resulting models visualized in Figure 4.1 give a clear indication which driver is more robust and whether one will surpass the lifetime given by the manufacturer in the data sheet.

4.1.1 Model Fitting for Censored Datasets

To fit the two chosen models to more than just three of the tested drivers a strategy to deal with right-censored data is required. Traditional methods that take into account the statistical distribution of the lifetime data cannot be applied to the available dataset as only a single device of each driver type was tested at each environmental condition. The straightforward solution is to take the censoring time to be the failure time of a device. This leads to a conservative model as it is likely that the device would only have failed long after the test has been terminated. Being an estimate that errs on the side of caution it can still demonstrate whether a driver will outlast the lifetime guaranteed by the manufacturer. The analysis is limited to three drivers where only a single lifetime is right-censored. In all three cases the lifetime from the 65 °C/90 % is right-censored. Data from drivers with two or more censored lifetimes must be discarded as their analysis would stretch the explanatory power of the extrapolation to its breaking point.

Model parameters for the drivers BAG LCS130-70FX-30/220-240, OSRAM OTi DALI 60/220-240/550 D LT2 L and Vossloh-Schwabe ECXd 700.149 can be found in Table 4.1. The resulting lifetime plots are presented in Figure 4.2. Their respective manufacturers specify the following lifetimes for these drivers.

- BAG LCS130-70FX-30/220-240: 100 000 h at 65 °C and 50 000 h at 75 °C.
- OSRAM OTi DALI 60/220-240/550 D LT2 L: 100 000 h at 65 °C and 50 000 h at 75 °C.
- Vossloh-Schwabe ECXd 700.149: 100 000 h at 60 °C and 50 000 h at 70 °C.

These lifetimes are again marked in the plots with solid lines and their respective temperature limits by a

[1]The highest ever recorded dew point was 35 °C at an air temperature of 42 °C [119]. This equates to a relative humidity of about 69 %. If air that humid is heated to 60 °C the relative humidity drops to 22.5 %. This is can be regarded as an absolute upper limit for the levels of relative humidity that can be expected outdoors.

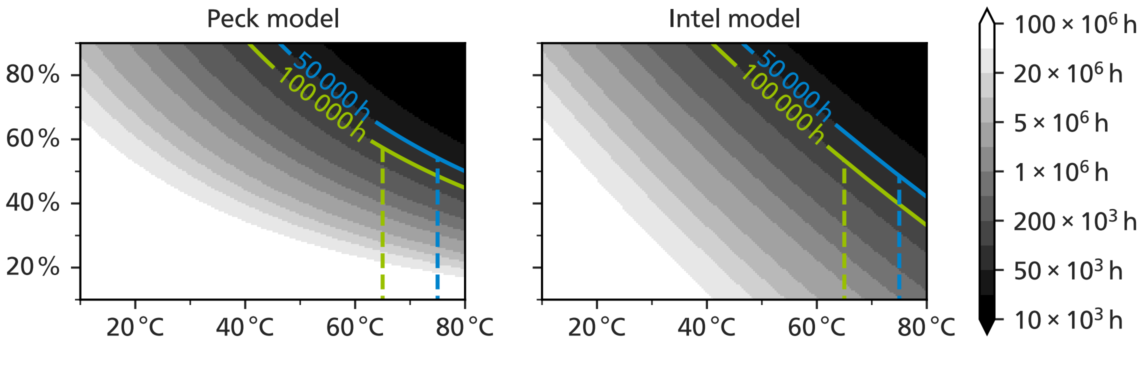

(a) BAG LCS130-70FX-30/220-240

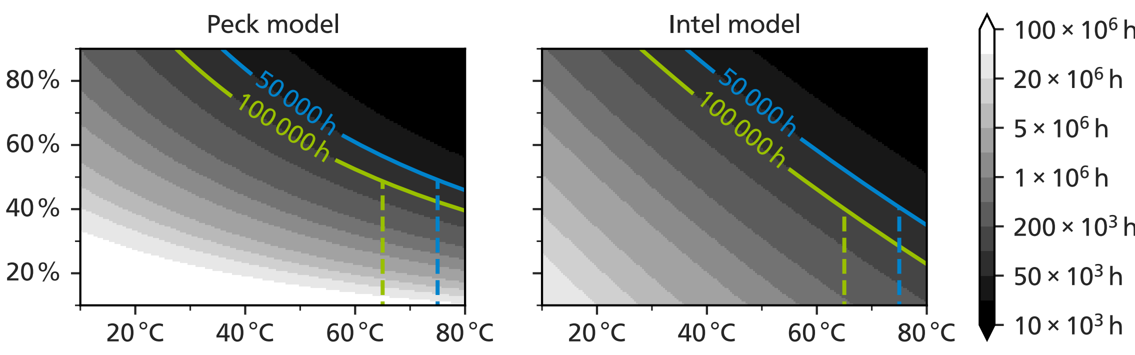

(b) OSRAM OTi DALI 60/220-240/550 D LT2 L

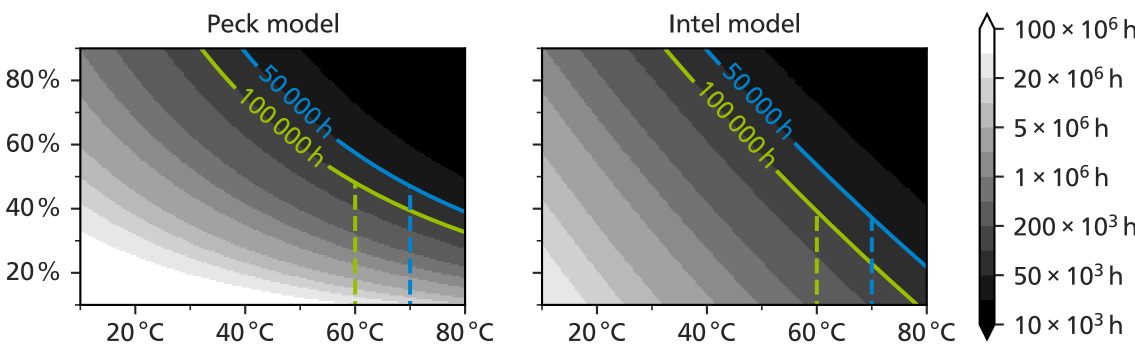

(c) Vossloh-Schwabe ECXd 700.149

Figure 4.2: Intensity plots visualizing the Peck and Intel model after fitting them for three drivers. The data for these three drivers contained one right-censored value each. The lifetimes specified by the manufacturers in the data sheets are marked with solid lines. A dashed line indicates the respective temperature limit for each lifetime.

dashed line. The relative humidity at the intersection of both lines exceeds 40 % in all cases. Comparing that to the critical level of 25 % as defined in Section 4.1, it can be concluded that these drivers will most likely outperform the guaranteed lifetime.

4.1.2 Estimated Driver Lifetime in Different Climatic Conditions

The plots shown in the previous section give an understanding of how long a driver can endure in a given static climatic condition. The question remains what will be the actual conditions a driver will be subjected to in the field. One way to tackle this issue is by calculating the estimated lifetime of a driver at a certain geographic location. Data from weather stations in several cities was acquired using the *meteostat* Python library [69]. Only data from the five year period between January 1st, 2017 and December 31st, 2021 is used for the analysis. The equation to calculate the average lifetime given the temperature T and relative humidity RH measured at the weather station over a timespan is given by

$$\overline{\text{lifetime}} = \frac{\sum_i model(T_i, RH_i) \cdot (t_i - t_{i-1})}{\sum_i t_i - t_{i-1}} \tag{4.1}$$

where t_i is the *i-th* point in time and $model(...)$ the accelerated failure time model. Five cities are selected to represent different climatic conditions.

- Darmstadt, Germany as a stand-in for a moderate continental climate.
- Orlando, Florida (FL), USA a the classical example of a hot and humid climate.
- Dubai, due to its hot and arid climate.
- Beijing, People's Republic of China (PRC) as an example of the rarely considered cold and arid climate.
- Vlieland, The Netherlands to represent a moderate coastal climate.

Using the data presented in Figure 4.3 and the model parameters from Table 4.1 an average lifetime can be calculated with Equation (4.1). The results of these calculations are shown in Table 4.2. A few general trends can be identified. The values estimated using the Peck model are higher than those for the Intel model in most cases. This comes as no surprise, as the Peck model tends to estimate much higher lifetimes at low levels of relative humidity. Vlieland tends to be the exception, here the estimations from both models are almost identical. All drivers would last almost indefinitely in the climate of Beijing. Vlieland and Orlando on the other hand seem to have the toughest climate. Still, most drivers would outlast the manufacturers specification by a huge margin.

The driver BAG LCS130-70FX-30/220-240 is the most extreme example of the bunch. It will probably never fail in normal operation. The Philips CertaFlux LLS ES 1150m 4500lm 840 HVI MST is an exception to the rule. In the tropical Orlando weather its estimated lifetime barely exceeds the 50 000 h guaranteed by the manufacturer. In the dry heat of Dubai this is only the case for the Intel model. Given the uncertainties associated with the huge difference in timescale between the values from the accelerated lifetime test and those that were extrapolated, a value that barely exceeds the requirements is insufficient to instil confidence in the robustness of the driver.

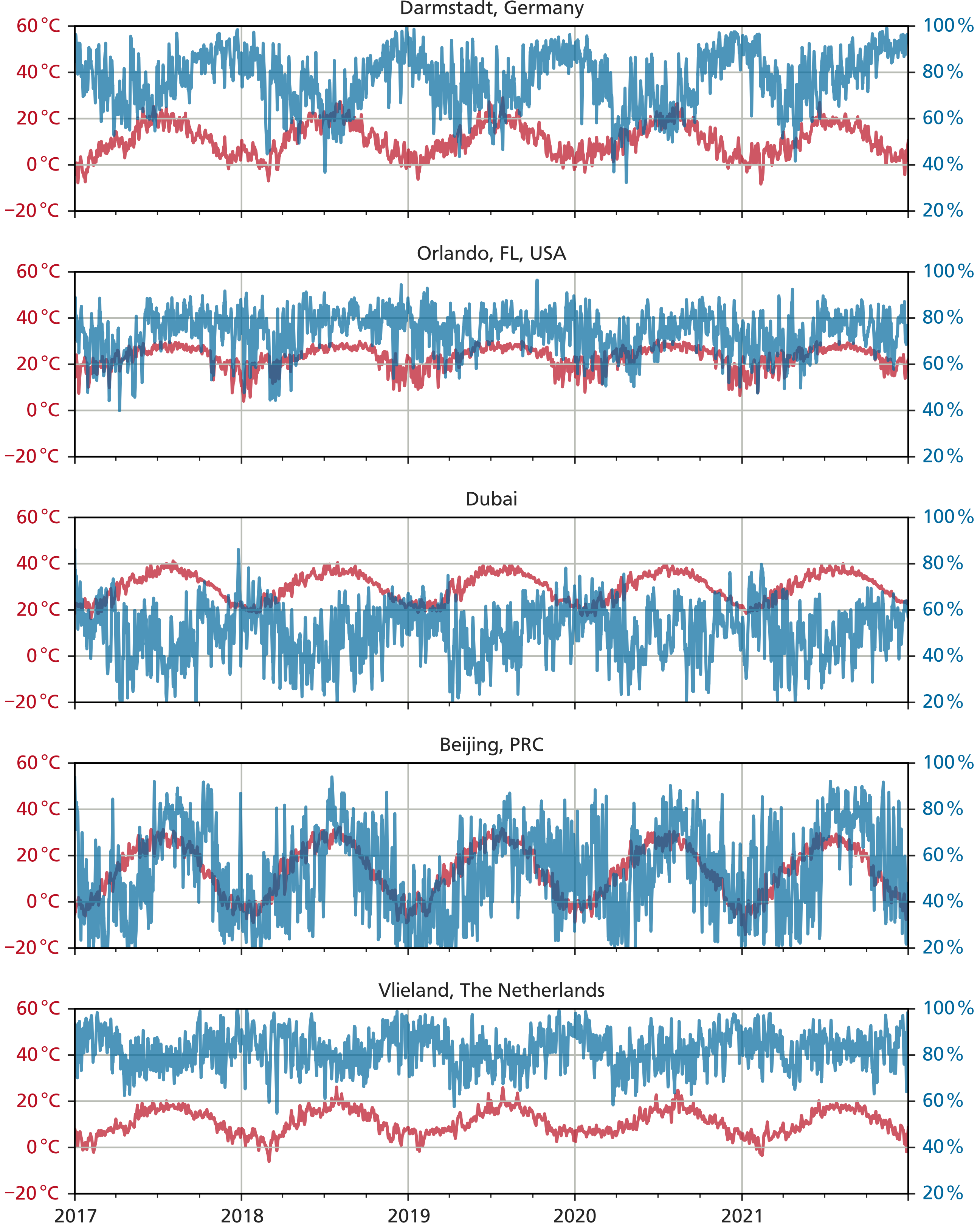

Figure 4.3: Temperature (red) and relative humidity (blue) readings for five selected cities between January 1st, 2017 and December 31st, 2021. The axes are scaled identically between all five plots. Each data point represents the rolling average calculated over two days worth of hourly data.

Table 4.2: Extrapolated lifetimes for five cities with different climates. Lifetimes over 10 000 000 h were clipped as they are physically impossible.

City	Model	OSRAM OT 40/120-277/1A0 4DIMLT2 E	Philips CertaFlux LLS ES 1150m 4500lm 840 HVI MST	BAG LCS130-70FX-30/220-240	OSRAM OTi DALI 60/220-240/550 D LT2 L	Vossloh-Schwabe ECXd 700.149
		Lifetime / h				
Darmstadt, Germany	Peck	>10 000 000	161 637	>10 000 000	3 451 594	3 912 537
	Intel	6 516 049	147 457	>10 000 000	1 591 092	2 552 021
Orlando, FL, USA	Peck	6 769 155	67 147	>10 000 000	1 633 007	1 550 119
	Intel	2 159 233	59 023	>10 000 000	696 786	904 417
Dubai	Peck	>10 000 000	102 912	>10 000 000	>10 000 000	7 285 072
	Intel	2 965 606	59 060	>10 000 000	1 134 171	1 119 923
Beijing, PRC	Peck	>10 000 000	1 256 224	>10 000 000	>10 000 000	>10 000 000
	Intel	>10 000 000	414 833	>10 000 000	>10 000 000	>10 000 000
Vlieland, The Netherlands	Peck	3 856 570	119 669	>10 000 000	990 441	1 751 977
	Intel	3 791 487	121 693	>10 000 000	987 752	1 770 889

4.2 Survival Analysis of the Accelerated Lifetime Test Results

In total 25 different drivers have been tested in the 85 °C/85 % environment. For most drivers only a single device has been included in the test. Nonetheless, this is a significant sample size and well worth exploring, especially considering the wide variety of drivers that have been tested. Using survival analysis methods this sample can be scrutinized to identify properties that can make a driver last longer or fail earlier. The following analysis extends the previous one using the same data that was presented in [146].

A broad selection of properties is recorded for the available drivers. These properties are presented in Table 4.3. The values shown are either taken from the driver's data sheet or obtained through examination of the actual circuit assembly. The following properties are included in the table.

- Whether the SMPS topology contains a dedicated PFC stage or not.
- Whether the driver's output current is programmable, i.e. can be changed by the end-user.
- Whether the driver features a communication interface such as DALI or a dimming input.
- Whether the PCB is made from FR-4 material instead of the cheaper FR-2.
- Whether the circuit assembly has been protected from the elements by either a layer of conformal coating or has been potted.
- Whether the driver is considered to be *high-end* or of a lower quality[2].
- The maximum output power of the driver.
- The maximum output current of the driver.
- The maximum voltage at the output of the driver.

Two of the columns in Table 4.3 contain missing values that are marked as *N/A*. For two drivers it is impossible to check whether they contained a multilayer PCB because of the potting of the circuit assembly. And for one driver the maximum output current is not listed in the corresponding data sheet. These three drivers would have had to be excluded from the analysis due to the missing values. To retain a complete dataset the missing values are imputed using the k-nearest neighbors algorithm. This algorithm selects a number of k neighbors from the dataset based on the features that are not missing. It then uses these neighbors to calculate a value for the missing feature. For this work the number of neighbors k is set to five and the average of the neighbors' values is used to fill in the missing one.

The Cox PH model as introduced in Section 2.7.2 is a suitable model to analyze whether these properties or parameters have a significant impact on the lifetime of a driver. It can also deal with right-censored data, making it possible to take into consideration the devices that did not fail during the test. Which properties to include into the final model as covariates still has to be decided.

The Wilkinson notation [129] is used to describe the possible models in textual form. A model describing the hazard of a device as a function of whether it features a PFC stage, a FR-4 PCB and the value of its maximum output power in Watt can be written as

$$\mathcal{H} \sim \beta_{PFC} + \beta_{power} + \beta_{FR-4}, \tag{4.2}$$

which translates to the Cox PH model

[2]The drivers where categorized as either *low-cost* or *high-end* based on the feedback from industry experts.

Table 4.3: Properties of the drivers that were used as covariates in the various Cox PH models.

Manufacturer	Manufacturer part number	has PFC	curr. programmable	comm. interface	has FR-4 PCB	multilayer PCB	coating/potting	“high-end”	max. power / W	max. current / mA	max. voltage / V
BAG	CCS170-35QS-01/220-240	✓			✓	✓		✓	43.7	700	50
BAG	CCS1150-50FR-20/220-240	✓	✓		✓			✓	50.0	1500	55
BAG	LCS130-70FX-30/220-240	✓					✓	✓	70.0	300	230
ERP	PSB30E-0700-42-T	✓[a]	✓	✓	✓	✓	✓		29.4	700	50
LG Innotek	LLP 150W 0.7A 125 280Vdc PISE-A150D	✓[a]	✓	✓	✓	*N/A*	✓	✓	168.0	700	280
LUMNIUM	54H-120B-GM-0450							✓	54.0	450	160
N/A	CLNC24W028L								24.0	280	80
N/A	CLNC65W042L								65.0	420	154
N/A	LGM22W016P2								22.0	160	145
N/A	LGM52W041P2								52.0	410	135
OSRAM	OT 40/120-277/1A0 4DIMLT2 E	✓	✓	✓	✓	✓	✓	✓	40.0	1050	56
OSRAM	OT 165/170-240/1A0 4DIMLT2 E	✓[a]	✓	✓	✓	*N/A*		✓	165.0	1050	285
OSRAM	OT FIT 35/220-240/700 CS	✓	✓		✓	✓		✓	38.0	700	54
OSRAM	OTi DALI 60/220-240/550 D LT2 L	✓	✓	✓	✓	✓		✓	60.0	550	240
OSRAM	OTi DALI 90/220-240/1A0 LT2 L	✓	✓	✓	✓	✓		✓	90.0	1000	240
Philips	CertaDrive 60W 360mA 170V 230V								67.0	360	340
Philips	CertaFlux LLS ES 1150m 4500lm 840 HVI MST							✓	35.0	*N/A*	245[b]
Philips	Xitanium 9290 008 818	✓	✓		✓	✓		✓	36.0	1050	60
TRIDONIC	LC 25W 100-500mA flexC lp EXC	✓	✓					✓	25.0	500	60
TRIDONIC	LC 57/1050/54 fixC lp SNC2								56.7	1050	60
Vossloh-Schwabe	ECXd 700.149	✓	✓	✓	✓	✓		✓	84.0	700	220
Vossloh-Schwabe	ECXe 350.298								65.0	350	350
Vossloh-Schwabe	ECXe 700.199		✓					✓	40.0	700	60
Vossloh-Schwabe	ECXe 1050.233								45.0	1050	60
WE-EF	ED100-66/700-1050/230-50-60/O-O				✓	✓		✓	66.0	1050	94

[a] The driver’s circuit could not be analysed due to it being potted. It is assumed it features a PFC stage.
[b] This value had to be obtained through measurement as it was not specified in the data sheet.

$$h(t, \mathbf{X}) = h_0(t)\, e^{\beta_{PFC} x_{PFC} + \beta_{power} x_{power} + \beta_{FR-4} x_{FR-4}}. \tag{4.3}$$

Although the dataset at hand is sufficient for a proper analysis, it is still small enough so that all possible parameter combinations can be explored by fitting the requisite Cox PH models. To select the best fitting model the AIC is calculated for each combination. The models are then ranked by the AIC from lowest to highest. Figure 4.4 shows the AIC for the first ten models. The AIC is almost identical for the first three models, after that the value increases significantly. Therefore, the first three models are looked upon in detail. The model parameters for these three models are shown in Table 4.4.

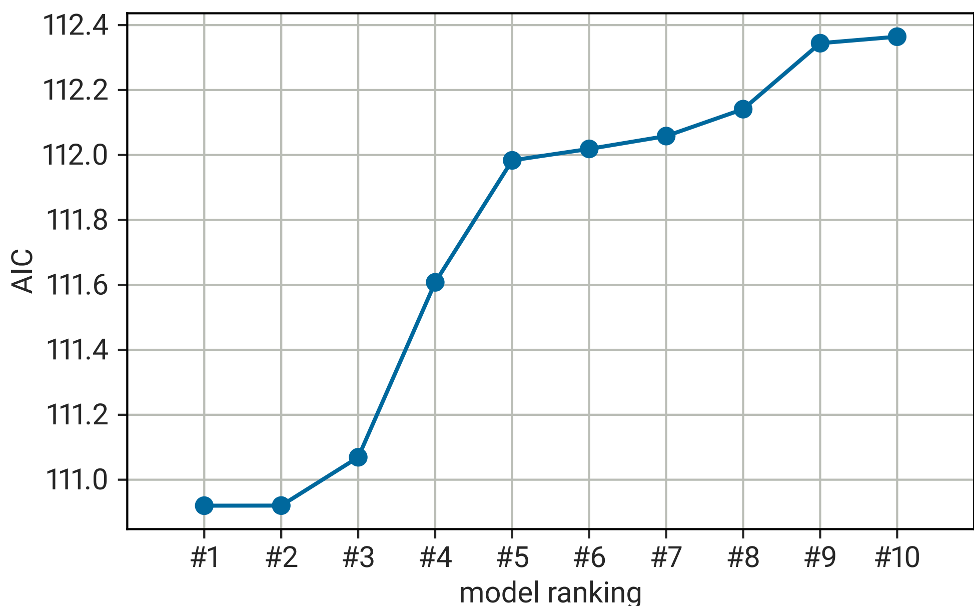

Figure 4.4: Plot showing the ten best fitting Cox PH models, sorted by their AIC value. Note that the first three models have almost identical values.

Although the three models have almost identical AIC values, given a level of significance of $\alpha = 5\,\%$ for the covariates, only the first and last model will be taken into account. For the second model the p-values of the parameters $\beta_{\text{FR-4}}$ and $\beta_{\text{programmable}}$ are much higher than the chosen level of significance and the model is therefore discarded.

The models identify three properties that influence the lifetime of a given driver: whether its PCB is made from FR-4 material; what its maximum output power is; and whether its output current is programmable. It comes as no surprise that the maximum output power has a detrimental effect on the lifetime of a driver. The higher its power the higher are the currents that the SMPS circuit has to handle and – due to the limited efficiency of all electronic circuits – the more waste heat is produced inside the driver's case. The model shows that an increase in power of one Watt increases its risk to fail by3 %.

Having a programmable output current and a robust FR-4 PCB are both features of more upmarket drivers. That these live longer than their cost-optimized counterparts is unsurprising. The first model shows that – corrected for the effect of the output power – a driver with a PCB that is not made from FR-4 is about 4.76 times as likely to fail. And, judging from the last model, a driver with a fixed output current is 3.85 times as

Table 4.4: Model parameters for the three Cox PH models with the lowest AIC value. Only the exponent of the value for the parameters β is given as it is easier to interpret. The p-values are given to indicate whether the effect is statistically significant.

Model	AIC	$\beta_{\text{FR-4}}$				β_{power}				$\beta_{\text{programmable}}$			
		e^{β}	95 % CI		p	e^{β}	95 % CI		p	e^{β}	95 % CI		p
$\beta_{\text{FR-4}} + \beta_{\text{power}}$	110.92	0.21	0.07	0.64	0.01	1.03	1.01	1.05	<0.005				
$\beta_{\text{FR-4}} + \beta_{\text{power}} + \beta_{\text{programmable}}$	110.92	0.38	0.10	1.46	0.16	1.03	1.01	1.05	<0.005	0.41	0.12	1.41	0.16
$\beta_{\text{power}} + \beta_{\text{programmable}}$	111.07					1.03	1.01	1.04	0.01	0.26	0.10	0.68	0.01

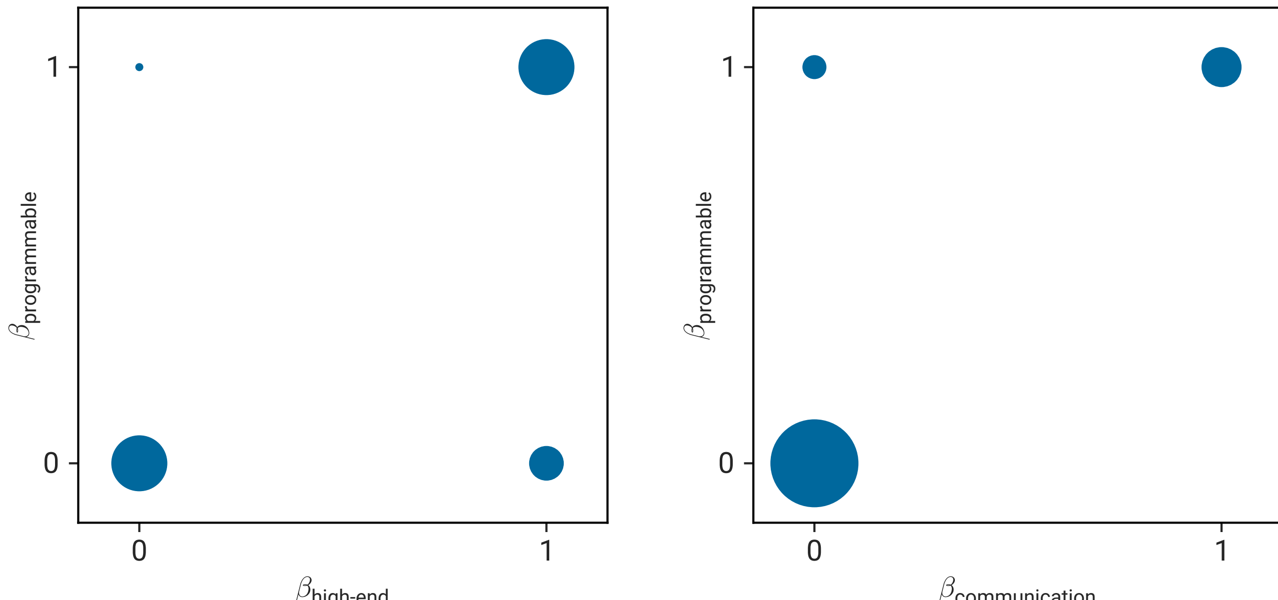

Figure 4.5: Scatter plots illustrating the correlation between $\beta_{\text{programmable}}$ and two other parameters. The diameter of the circles is proportional to the number of drivers that feature this combination of parameters. In case of a perfect correlation, two equally sized circles could be seen along one of the diagonals.

likely to fail compared to one with a programmable output current. It has to be kept in mind that these results are for drivers that were tested in an 85 °C/85 % environment. Assuming that the effect of these properties is independent of the temperature and relative humidity these findings can be applied to drivers in general.

Making the output current of a driver programmable requires a more complex circuit and increases the component costs. It is a feature that is rarely found in cost-optimized drivers and is therefore indicative of more premium products. The question is why this feature is also associated with a longer lifetime. The most likely explanation is that it is a proxy indicating a more careful design. The driver properties as listed in Table 4.3 contain two more parameters that could distinguish higher quality drivers: one is whether a driver features a communication interface; the other is whether this driver is considered to be high-quality by industry experts. To check whether these properties are as good a proxy for the quality and therefore durability of a driver they are charted in two scatter plots versus $\beta_{\text{programmable}}$. The results can be seen in Figure 4.5. Although both parameters are slightly correlated to $\beta_{\text{programmable}}$, neither can serve as its proxy. This agrees with the findings from the Cox PH models, where the models containing these parameters would have scored a higher AIC otherwise. The mechanism that causes drivers with a programmable output current to live longer than those that do not have this feature remains obscure. However, the effect is significant and this property should be taken into account when selecting drivers that are supposed to last a long time.

Why the absence of an FR-4 PCB makes a driver more likely to fail still has to be established. Drivers that do not use FR-4 substrate for their circuit board use FR-2, which is inherently a lower quality material. Three possible routes of explanation need to be explored. The first is a higher failure rate due to surface contamination. The effects of surface contamination have been disseminated in Section 3.2.1. The contaminants on a PCB's surface usually are flux residues. Wavesoldering is inherently prone to leaving flux residues all over the

surface of the PCB as it requires covering the whole area with flux. The wavesoldering process is illustrated in Figure 4.6, showing the flux application with a flux sprayer. After soldering the flux residues should be removed by washing of the circuit assembly. However, it can be shown that all drivers tested for this work were assembled using wavesoldering[3]. The soldering process can therefore not explain the difference in reliability between FR-4 and FR-2 PCBs. Another possible explanation is that FR-2 PCBs tend to not get cleaned after soldering due to the material being more hygroscopic than FR-4 and most modern cleaning solutions being water-based. Unfortunately, there are no publications that would support this hypothesis.

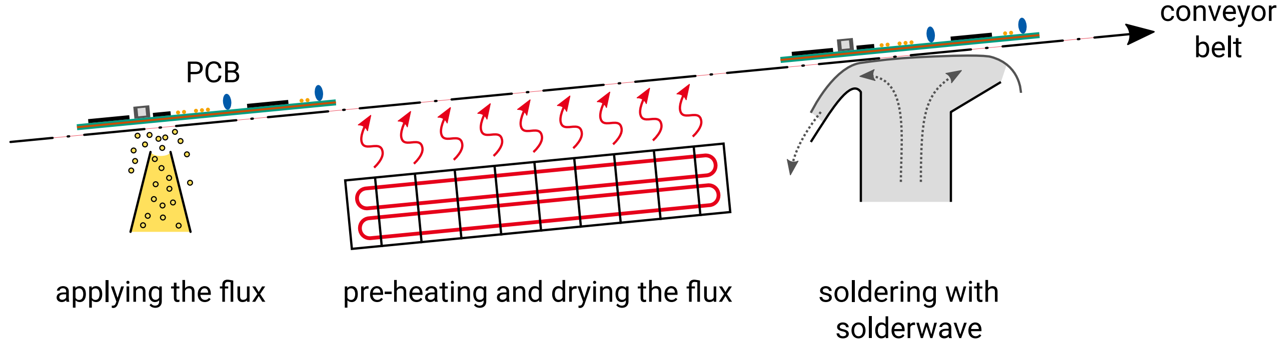

Figure 4.6: Illustration of the wavesoldering process. This is a continuous process, the PCBs get dragged through it on a conveyor belt. Please note the flux sprayer at the beginning of the process. It completely covers the PCB's area with liquid flux.

An attentive observer might also suggest that the observed effect might be merely caused by a correlation between the used PCB material and some other failure mode. As the failure mode is known for the majority of failed devices it is possible to check whether any of them is correlated with the PCB material. This relationship is displayed in Figure 4.7. Looking at the total number of failures there is no discernible difference between both materials. One failure mode where drivers with an FR-2 PCB failed significantly more frequently is the dielectric breakdown, which is expected. For all other failure modes no such effect can be found. The failure of an IC package was not observed in any driver with an FR-2 circuit board, so no comparison can be made here. To put it in a nutshell, the choice of PCB material does of course influence whether a driver fails due to dielectric breakdown of that material, but the effect is genuine and not correlated with any other design, material or component choice.

The final and most likely reason why boards made from FR-2 material fail sooner is that the dielectric properties are simply inferior to those of FR-4, especially in humid environments. This is because FR-2 absorbs moisture much more readily than FR-4 [19, 20]. That water can reduce the isolation resistance of a material has been discussed in detail in Section 3.2.3, so it is more than likely that it would have the same effect in a PCB's base material.

4.3 Improving the Robustness of Off-Line LED Drivers

Looking at the failure mode distribution as illustrated in Figure 4.8 it is clear that the dielectric breakdown of the PCB is the most prominent of them all. This has been confirmed by the survival analysis presented in Section 4.2, where the quality of the circuit board base material was identified as one of the most important factors for the reliability of a device. Designers of off-line LED drivers should therefore carefully consider the

[3]Two signs were taken to be indicative of an assembly that was assembled using wavesoldering: components glued to the bottom side of the PCB with a heat resistant glue and solder traps for the last row of pins of SMT ICs.

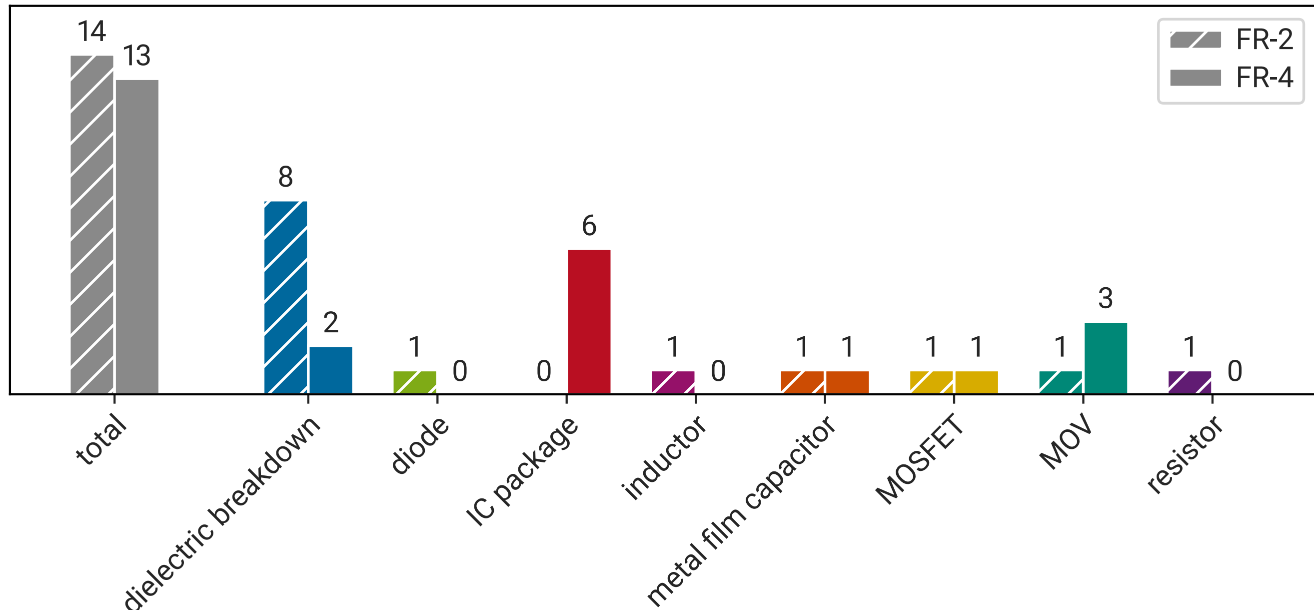

Figure 4.7: Frequency of the different failure modes distinguished by the base material used for circuit's PCB.

choice of PCB material. The Cox PH model presented earlier estimates that choosing an FR-4 board over a cheaper alternative reduces a driver's risk to fail by a factor of 4.76, which is a significant improvement if there ever was one.

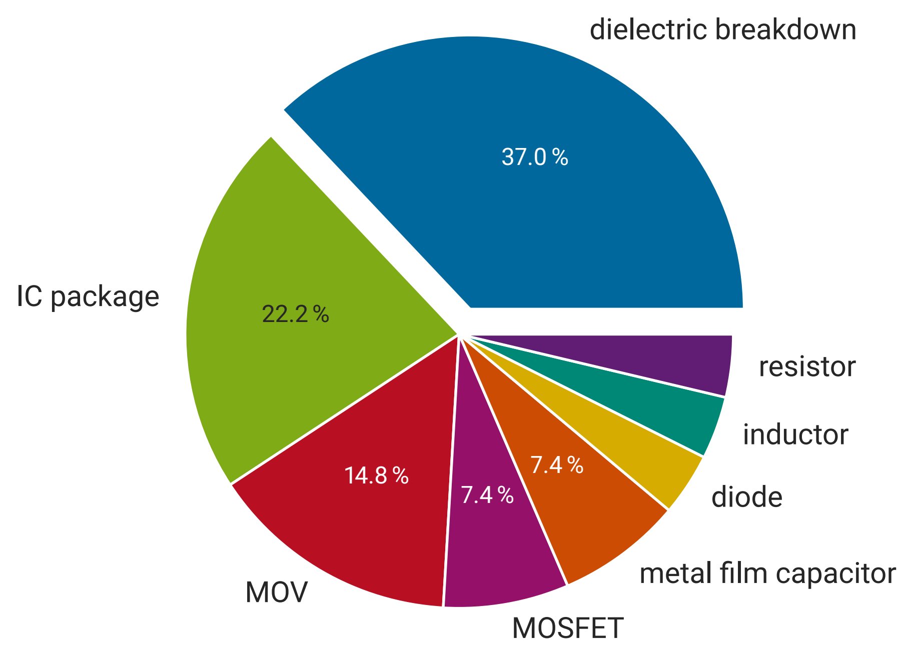

Figure 4.8: Pie chart illustrating the distribution of the observed failure modes. Dielectric breakdown of the circuit board was by far the most frequent failure mode. The devices where the failure mode could not be identified were not taken into account for this plot.

Table 4.5: Minimum required isolation distance as specified by four different international standards. The two peak voltage levels were chosen to represent line voltage and rectified line voltage as commonly found in the PFC stage.

Peak voltage	Minimum required isolation distance / mm			
	IPC-2221A [42]	DIN EN IEC 62368-1 [107]	DIN EN 61347-1 [68]	IPC-9592 [104]
250 V	0.4	0.56	1.0	1.85
500 V	0.8	1.3	2.5	3.1

The forensic analysis in Section 3.2.1 could also demonstrate that if a failure occurs it happens at a location on the PCB where a large voltage difference is separated by a small isolation distance. Tracks with a voltage difference of 325 V and an isolation distance as small as 0.5 mm were observed in the analysis. There exists a wide variety of international standards specifying very different requirements for the minimum required isolation distance even at the same peak voltage differential. A selection of these specifications is presented in Table 4.5. The generic IPC standard IPC-2221A [42] has the most relaxed requirements, while IPC-9592 [104] – being intended for devices in critical applications like telecommunications – asks for a quite substantial isolation distance. Designers should rather err on the side of caution, especially if they are working with lesser quality PCB substrates such as FR-2. It is also worthwhile to think about extending these standards with rules governing the use of PCB materials other than FR-4. The minimum distance requirements should be increased for the less robust ones.

Finally, the design rule checking engines available in today's PCB design software rely on the engineer to enter all necessary constraints manually, for example the maximum current a track will carry or its maximum voltage. These values can be very tricky to gauge correctly making this process error prone, especially in complex circuits such as an SMPS. To tackle this issue a closer integration between circuit simulation, real world measurements and the PCB layout process would be required.

The failure of IC packages and MOVs are also noteworthy. The results presented in Section 3.2.2 are not sufficient to say whether better cooling would have prevented the failure of the ICs. What can be said with certainty is that designers should follow the manufacturer's application notes for these components more closely and add as much heatsinking copper area as possible. Even if this will not improve the robustness of the design it will at least not impede it either.

The MOV failures described in Section 3.2.3 have one thing in common: the MOV that failed is placed in close proximity to a switching node of the SMPS circuit. Without a filtering element suppressing it, the high frequency switching noise can enter the MOV. This causes a leakage current to flow through the component. It is very likely that this current leads to the early demise of the MOV. Therefore, for a more robust circuit MOVs should never be placed next to switching nodes but rather before the common-mode choke that is part of the line side EMI filter.

Finally, the findings suggest that the commonly suspected aluminium electrolytic capacitors no longer cause the failure of modern SMPS circuits[4]. Research efforts can therefore start to focus on other critical components, such as MOVs and ICs.

[4] See Section 3.1

5 Conclusion

This work presents the results of a comprehensive accelerated lifetime study of off-line LED drivers. In the introduction the motivation for the study is given and the working principle of LED drivers is outlined. This is followed by the description of the experimental setup. It includes the measurement equipment that is installed to monitor the DUTs as well as the software that records and analyses the generated data. The analytical approach is presented as well. The core of the work however are the results of the accelerated lifetime tests and their analyses. In total 75 devices have been tested at four different environmental conditions. Over the course of the tests 39 failures have been recorded. The failure mode is identified for 27 devices out of the 39. The most common failure mode is a dielectric breakdown of the driver's PCB, followed by defects of an IC package. By measuring the capacitance of the aluminium electrolytic capacitors from a set of drivers tested in dry heat at 85 °C it can be demonstrated that their degradation is unlikely to cause the failure of modern LED drivers. The two introduced physical models are successfully fitted to the available failure time data for five driver types. Their lifetime is extrapolated for different environmental conditions and is shown to exceed the manufacturers guarantee in all outdoor climates. The results from the test in damp heat at 85 °C/85 % are then used to fit three Cox PH models. These models identify the PCB substrate of a driver, its maximum power in Watt and whether its output current is programmable as the most significant properties for its reliability. Finally, these findings are discussed and recommendations for future designs are given.

5.1 Summary

This work set out to answer the three research questions introduced in Chapter 1. To demonstrate that this enterprise was a success, the following paragraphs will frame an answer for each question.

When do off-line LED drivers fail? By estimating their lifetime with two physical models fitted to the failure time data from the presented accelerated lifetime study, it can be demonstrated that modern LED drivers will most likely exceed the lifetime guaranteed by their respective manufacturers. Due to the limited sample size this result cannot be backed up with a statistical model of the failure time distribution. But the confidence in the results is still significant, as the estimated lifetimes surpass the manufacturer guaranteed values by a huge margin.

Why do off-line LED drivers fail? Although electronic devices are susceptible to heat, the presented results – especially those for the degradation of the aluminium electrolytic capacitors in Section 3.1 – show that heat alone will not cause modern LED drivers to fail any time soon. Adding humidity as an additional stress paints a different picture, as a host of failure modes are now triggered. The experimental effort for tests in damp heat may be high, but it is indispensable if a test is supposed to see drivers fail. It should also be included in the lifetime specifications of electronic devices. When looking at the driver itself, two succinct parameters can be identified that significantly affect its lifetime. These are the maximum output power and the substrate used for the PCB, namely FR-4 or FR-2 material.

How do off-line LED drivers fail? Eight different failure modes are identified in Section 3.2, the two most

common ones being dielectric breakdown of the PCB and a defect of an IC package. It is also noteworthy that in some drivers the failure of a MOV was observed. It is shown that only MOVs placed electrically close to switching nodes in the circuit fail.

These findings can be distilled into a set of recommendations for future driver designs. They can be found in Section 4.3. Knowing that modern LED drivers have proven to be very robust – they have been demonstrated to reach or even vastly exceed the manufacturer guaranteed lifetimes – the question should be asked whether they have been over-engineered. On the one hand longevity is advantageous as the production and installation of a replacement device burdens the limited natural resources; on the other hand a driver that is built so sturdy that it will outlast its technological obsolescence is a wasted opportunity to reduce resource usage. To better navigate this thin line more research into failure modes and accelerated testing is needed.

5.2 Outlook

Three future avenues of research can be drawn from the previously presented results. The first is an accelerated lifetime study with a significant number of samples of each driver type at each environmental conditions. It will allow to estimate the statistical distribution of the lifetime. Using the calculated variability of the lifetime values it will be possible to judge whether the results of this work are spot-on. The estimated statistics can also form the basis for the optimal planning of future accelerated lifetime tests.

The second study should focus on the dielectric breakdown of the PCB. The scientific literature is limited when it comes to PCB substrates other than FR-4, even though materials like FR-2 are commonly used in commercial products. Whether these materials are more susceptible to dielectric breakdown – especially in humid environments – has to be determined. This should also include inquiries into whether their failure is connected to surface contamination or the manufacturing process.

Finally, two components have to be studied in more detail. Whether the degradation of MOVs is affected by switching noise has to be proven in a controlled setting. If so, a follow-up experiment could compare the effectiveness of different countermeasures such as filtering. The second component that has to be scrutinized is the SMPS controller IC. It has to be determined if IC packages handling high voltages of 300 V and more are generally susceptible to failure and how their robustness is influenced by the PCB layout.

Bibliography

[1] Hirotogu Akaike. “Information Theory and an Extension of the Maximum Likelihood Principle”. In: *Breakthroughs in Statistics: Foundations and Basic Theory*. Ed. by Samuel Kotz and Norman L. Johnson. New York, NY: Springer New York, 1992, pp. 610–624. ISBN: 978-1-4612-0919-5. URL: https://doi.org/10.1007/978-1-4612-0919-5_38.

[2] Svante Arrhenius. “Über Die Reaktionsgeschwindigkeit Bei Der Inversion von Rohrzucker Durch Säuren”. In: *Zeitschrift für Physikalische Chemie* 4U.1 (1889), pp. 226–248. DOI: 10.1515/zpch-1889-0416.

[3] Marijan Beg et al. “Using Jupyter for Reproducible Scientific Workflows”. In: *Comput. Sci. Eng.* 23.2 (Mar. 2021), pp. 36–46. ISSN: 1521-9615, 1558-366X. DOI: 10.1109/MCSE.2021.3052101.

[4] Keith H. Billings and Taylor Morey. *Switchmode Power Supply Handbook*. 3rd ed. New York: McGraw-Hill Professional, 2011. ISBN: 978-0-07-163971-2.

[5] David L. Blackburn. “Turn-Off Failure of Power MOSFET’s”. In: *IEEE Transactions on Power Electronics* PE-2.2 (Apr. 1987), pp. 136–142. ISSN: 1941-0107. DOI: 10.1109/TPEL.1987.4766347.

[6] P. Bokoro and I. Jandrell. “The Impact of Harmonics on the V - I Characteristic of ZnO Varistors”. In: *2016 IEEE International Conference on Dielectrics (ICD)*. Vol. 2. July 2016, pp. 658–661. DOI: 10.1109/ICD.2016.7547701.

[7] Maike Bröker and Volker Hinrichsen. “Testing Metal–Oxide Varistors for HVDC Breaker Application”. In: *IEEE Transactions on Power Delivery* 34.1 (Feb. 2019), pp. 346–352. ISSN: 1937-4208. DOI: 10.1109/TPWRD.2018.2877464.

[8] Douglas Brown et al. “Electronic Prognostics - A Case Study Using Switched-Mode Power Supplies (SMPS)”. In: *2006 IEEE Autotestcon*. Sept. 2006, pp. 636–642. DOI: 10.1109/AUTEST.2006.283739.

[9] R.W. Brown. “Linking Corrosion and Catastrophic Failure in Low-Power Metallized Polypropylene Capacitors”. In: *IEEE Transactions on Device and Materials Reliability* 6.2 (June 2006), pp. 326–333. ISSN: 1558-2574. DOI: 10.1109/TDMR.2006.876612.

[10] M. Catelani and L. Ciani. “Experimental Tests and Reliability Assessment of Electronic Ballast System”. In: *Microelectronics Reliability* 52.9-10 (Sept. 2012), pp. 1833–1836. ISSN: 00262714. DOI: 10.1016/j.microrel.2012.06.077.

[11] J. Celaya et al. “Towards Accelerated Aging Methodologies and Health Management of Power MOSFETs (Technical Brief)”. In: *undefined* (2009). URL: https://www.semanticscholar.org/paper/Towards-Accelerated-Aging-Methodologies-and-Health-Celaya-Patil/edf1a682b7d60d1370965b90e9d10aabfae5c1e1 (visited on 21. Jan. 2022).

[12] Christine Ferretti. "Detroit's LED Streetlights Going Dark after a Few Years". In: *The Detroit News* (May 2019). URL: https://eu.detroitnews.com/story/news/local/detroit-city/2019/05/07/detroits-led-streetlights-going-dark-after-few-years/3650465002/ (visited on 17. Sept. 2022).

[13] David R. Clarke. "Varistor Ceramics". In: *Journal of the American Ceramic Society* 82.3 (1999), pp. 485–502. ISSN: 1551-2916. DOI: 10.1111/j.1151-2916.1999.tb01793.x.

[14] K. G. Compton, A. Mendizza, and S. M. Arnold. "Filamentary Growths On Metal Surfaces – "Whiskers"". In: *CORROSION* 7.10 (Oct. 1951), pp. 327–334. ISSN: 0010-9312, 1938-159X. DOI: 10.5006/0010-9312-7.10.327.

[15] Kenneth A. Connors. *Chemical Kinetics: The Study of Reaction Rates in Solution*. New York, N.Y: VCH, 1990. ISBN: 978-1-56081-006-3 978-3-527-28037-7.

[16] W. J. Conover. "Some Reasons for Not Using the Yates Continuity Correction on 2 × 2 Contingency Tables". In: *Journal of the American Statistical Association* 69.346 (1974), pp. 374–376. ISSN: 0162-1459. DOI: 10.2307/2285661.

[17] Helene Conseil et al. "Humidity Build-Up in a Typical Electronic Enclosure Exposed to Cycling Conditions and Effect on Corrosion Reliability". In: *IEEE Trans. Compon., Packag. Manufact. Technol.* 6.9 (Sept. 2016), pp. 1379–1388. ISSN: 2156-3950, 2156-3985. DOI: 10.1109/TCPMT.2016.2590779.

[18] Clyde F. Coombs, ed. *Printed Circuits Handbook*. 6th ed. McGraw-Hill Handbooks. New York: McGraw-Hill, 2008. ISBN: 978-0-07-146734-6.

[19] *Copper Clad FR2 Epoxy Paper Printed Circuit Board*. Datasheet 583654_v1. R-Tech, July 2021. URL: https://static.rapidonline.com/pdf/34-1026_v1.pdf (visited on 16. Sept. 2022).

[20] *Copper Clad FR4 Fibre Glass Printed Circuit Board*. Datasheet 583651_v1. R-Tech, July 2021. URL: https://static.rapidonline.com/pdf/34-1015_v1.pdf (visited on 16. Sept. 2022).

[21] D. R. Cox. "Regression Models and Life-Tables". In: *Journal of the Royal Statistical Society. Series B (Methodological)* 34.2 (1972), pp. 187–220. ISSN: 00359246. JSTOR: 2985181. URL: http://www.jstor.org/stable/2985181 (visited on 9. Aug. 2021).

[22] D. R. Cox and David Oakes. *Analysis of Survival Data*. Monographs on Statistics and Applied Probability. London ; New York: Chapman and Hall, 1984. ISBN: 978-0-412-24490-2.

[23] Cameron Davidson-Pilon. *Lifelines*. DOI: 10.21105/joss.01317.

[24] J. Lynn Davis. *System Reliability Model for Solid-State Lighting (SSL) Luminaires*. Tech. rep. United States: RTI International, Research Triangle Park, NC (United States), May 2017. URL: https://doi.org/10.2172/1360770.

[25] J. Lynn Davis and Anne Arquit Niederberger. "Reliable LED Lighting Technologies Key Factors and Procurement Guidance". In: *Proceedings of the 5th IEEE Global Humanitarian Technology Conference, GHTC 2015* (2015), pp. 191–198. ISSN: 9781467365611. DOI: 10.1109/GHTC.2015.7343972.

[26] J. Lynn Davis et al. "Leveraging Accelerated Testing to Assess the Reliability of Two-Stage and Multi-Channel Drivers". In: *2017 18th International Conference on Thermal, Mechanical and Multi-Physics Simulation and Experiments in Microelectronics and Microsystems (EuroSimE)*. Dresden, Germany: IEEE, Apr. 2017, pp. 1–6. ISBN: 978-1-5090-4344-6. DOI: 10.1109/EuroSimE.2017.7926224.

[27] J. Lynn Davis et al. "System Reliability for LED-based Products". In: *2014 15th International Conference on Thermal, Mechanical and Mulit-Physics Simulation and Experiments in Microelectronics and Microsystems (EuroSimE)*. IEEE, 2014, pp. 1–7. ISBN: 1-4799-4790-3.

[28] Lynn Davis et al. *Accelerated Stress Testing on Single-Channel and Multichannel Drivers - Initial Results*. Tech. rep. RTI International, Feb. 2018.

[29] Lynn. J. Davis. *Accelerated Life Test Results for SSL Luminaire Electronics*. San Francisco, CA, 2015. URL: https://www.energy.gov/sites/prod/files/2015/02/f19/davis-l_reliability_sanfrancisco2015.pdf (visited on 14. Dec. 2021).

[30] Marianne Diatta et al. "Understanding the Failure Mechanisms of Protection Diodes During System Level ESD: Toward Repetitive Stresses Robustness". In: *IEEE Transactions on Electron Devices* 59.1 (Jan. 2012), pp. 108–113. ISSN: 1557-9646. DOI: 10.1109/TED.2011.2173576.

[31] K. Eda. "Zinc Oxide Varistors". In: *IEEE Electrical Insulation Magazine* 5.6 (Nov. 1989), pp. 28–30. ISSN: 1558-4402. DOI: 10.1109/57.44606.

[32] Michael Alin Efroymson. "Multiple Regression Analysis". In: *Mathematical methods for digital computers* (1960), pp. 191–203.

[33] *Environmental Testing - Part 2-67: Tests - Test Cy: Damp Heat, Steady State, Accelerated Test Primarily Intended for Components*. International Standard DIN EN 60068-2-67:2020-08. International Electrotechnical Commission, Aug. 2020.

[34] J. D. Eshelby. "A Tentative Theory of Metallic Whisker Growth". In: *Phys. Rev.* 91.3 (Aug. 1953), pp. 755–756. ISSN: 0031-899X. DOI: 10.1103/PhysRev.91.755.2.

[35] M. G. Evans and M. Polanyi. "Some Applications of the Transition State Method to the Calculation of Reaction Velocities, Especially in Solution". In: *Trans. Faraday Soc.* 31.0 (Jan. 1935), pp. 875–894. ISSN: 0014-7672. DOI: 10.1039/TF9353100875.

[36] Henry Eyring. "The Activated Complex in Chemical Reactions". In: *J. Chem. Phys.* 3.2 (Feb. 1935), pp. 107–115. ISSN: 0021-9606. DOI: 10.1063/1.1749604.

[37] Xue-Jun Fan and Ephraim Suhir. *Moisture Sensitivity of Plastic Packages of IC Devices*. Springer, 2010. ISBN: 1-4419-5719-7.

[38] *Fixed Capacitors for Use in Electronic Equipment - Part 4: Sectional Specification - Fixed Aluminium Electrolytic Capacitors with Solid (MnO2) and Nonsolid Electrolyte*. International Standard DIN EN 60384-4:2017-04. Apr. 2017.

[39] I. Fukuzawa, S. Ishiguro, and S. Nanbu. "Moisture Resistance Degradation of Plastic LSIs by Reflow Soldering". In: *23rd International Reliability Physics Symposium*. Mar. 1985, pp. 192–197. DOI: 10.1109/IRPS.1985.362097.

[40] R. Gallay. "Metallized Film Capacitor Lifetime Evaluation and Failure Mode Analysis". In: *CAS - CERN Accelerator School: Power Converters* 003 (2016), pp. 7–14. ISSN: 9789290834151. DOI: 10.5170/CERN-2015-003.45.

[41] Geert Stevens. *AC Film Capacitors in Connection With the Mains ($\leq$ 60 Hz)*. Application Note 28153. Vishay Intertechnology, Inc., Dec. 2021. URL: www.vishay.com/doc?28153 (visited on 16. Feb. 2022).

[42] *Generic Standard on Printed Board Design*. International Standard IPC-2221A. IPC, May 2003.

[43] Lei Han and Nadarajah Narendran. "Developing an Accelerated Life Test Method for LED Drivers". In: *Proc. SPIE*. San Diego, CA, Aug. 2009. DOI: 10.1117/12.829901.

[44] K. Harada and A. Katsuki. "Deterioration Diagnosis of Electrolytic Capacitor in a Buck-Boost Converter". In: *PESC '88 Record., 19th Annual IEEE Power Electronics Specialists Conference*. Apr. 1988, 1101–1104 vol.2. DOI: 10.1109/PESC.1988.18249.

[45] Jinliang He et al. "AC Ageing Characteristics of Y2O3-doped ZnO Varistors with High Voltage Gradient". In: *Materials Letters* 65.17 (Sept. 2011), pp. 2595–2597. ISSN: 0167-577X. DOI: 10.1016/j.matlet.2011.06.022.

[46] Paul Horowitz and Winfield Hill. *The Art of Electronics: The x-Chapters*. Cambridge ; New York, NY: Cambridge University Press, 2020. ISBN: 978-1-108-49994-1.

[47] John D. Hunter. "Matplotlib: A 2D Graphics Environment". In: *Computing in Science Engineering* 9.3 (May 2007), pp. 90–95. ISSN: 1558-366X. DOI: 10.1109/MCSE.2007.55.

[48] Intel Corporation. *Components Quality/Reliability Handbook*. 1987. ISBN: 1-55512-054-7.

[49] *Is It Worth the Time?* URL: https://xkcd.com/1205/ (visited on 5. Mar. 2022).

[50] JEDEC Solid State Technology Association. *Failure Mechanisms and Models for Semiconductor Devices*. Tech. rep. JEP122H. Sept. 2016.

[51] Morten Stendahl Jellesen et al. "Corrosion in Electronics: Overview of Failures and Countermeasures". In: *European Corrosion Congress*. 2014.

[52] *Joint IPC/JEDEC Standard for Handling, Packing, Shipping, and Use of Moisture/Reflow Sensitive Surface-Mount Devices*. Tech. rep. J-STD-033D. JEDEC Solid State Technology Association, Apr. 2018.

[53] *Joint IPC/JEDEC Standard for Moisture/Reflow Sensitivity Classification for Nonhermetic Surface-Mount Devices*. Tech. rep. J-STD-020E. JEDEC Solid State Technology Association, Dec. 2014.

[54] E. L. Kaplan and Paul Meier. "Nonparametric Estimation from Incomplete Observations". In: *Journal of the American Statistical Association* 53.282 (1958), pp. 457–481. ISSN: 01621459. DOI: 10.2307/2281868.

[55] D.P. Kennedy and A. Phillips. "Source-Drain Breakdown in an Insulated Gate, Field-Effect Transistor". In: *1973 International Electron Devices Meeting*. Dec. 1973, pp. 160–163. DOI: 10.1109/IEDM.1973.188674.

[56] J.J. Kester et al. "Multistress Aging Tests of Polymer Housed Surge Arresters". In: *IEEE Trans. Power Delivery* 13.2 (Apr. 1998), pp. 446–452. ISSN: 08858977. DOI: 10.1109/61.660913.

[57] David G. Kleinbaum and Mitchel Klein. *Survival Analysis*. Springer, 2010.

[58] David G. Kleinbaum and Mitchel Klein. *Survival Analysis*. 3rd ed. Statistics for Biology and Health. New York: Springer, 2012. ISBN: 978-1-4419-6645-2.

[59] G. T. Kohman, H. W. Hermance, and G. H. Downes. "Silver Migration in Electrical Insulation". In: *The Bell System Technical Journal* 34.6 (Nov. 1955), pp. 1115–1147. ISSN: 0005-8580. DOI: 10.1002/j.1538-7305.1955.tb03793.x.

[60] S. Eloise Koonce and S. M. Arnold. "Growth of Metal Whiskers". In: *Journal of Applied Physics* 24.3 (Mar. 1953), pp. 365–366. ISSN: 0021-8979, 1089-7550. DOI: 10.1063/1.1721283.

[61] Chetan S. Kulkarni et al. "Prognostics of Power Electronics, Methods and Validation Experiments". In: *2012 IEEE AUTOTESTCON Proceedings*. Sept. 2012, pp. 194–199. DOI: 10.1109/AUTEST.2012.6334578.

[62] K. Lahti, K. Kannus, and K. Nousiainen. "Behaviour of the DC Leakage Currents of Polymeric Metal Oxide Surge Arresters in Water Penetration Tests". In: *IEEE Trans. Power Delivery* 13.2 (Apr. 1998), pp. 459–464. ISSN: 08858977. DOI: 10.1109/61.660915.

[63] Pradeep Lall, Michael Pecht, and Edward B. Hakim. *Influence of Temperature on Microelectronics and System Reliability*. The Electronic Packaging Series. Boca Raton: CRC Press, 1997. ISBN: 978-0-8493-9450-8.

[64] Pradeep Lall, Peter Sakalaukus, and Lynn Davis. “Prognostics of Damage Accrual in SSL Luminaires and Drivers Subjected to HTSL Accelerated Aging”. In: July 2013. DOI: 10.1115/IPACK2013-73250.

[65] Pradeep Lall, Peter Sakalaukus, and Lynn Davis. “Reliability and Failure Modes of Solid-State Lighting Electrical Drivers Subjected to Accelerated Aging”. In: *IEEE Access* 3 (2015), pp. 531–542. ISSN: 9781479952670. DOI: 10.1109/ACCESS.2015.2404812.

[66] Pradeep Lall, Peter Sakalaukus, and Lynn Davis. “Reliability of Solid-State Lighting Electrical Drivers Subjected to WHTOL Accelerated Aging”. In: *Fourteenth Intersociety Conference on Thermal and Thermomechanical Phenomena in Electronic Systems (ITherm)*. Orlando, FL, USA: IEEE, May 2014, pp. 1164–1170. ISBN: 978-1-4799-5267-0. DOI: 10.1109/ITHERM.2014.6892411.

[67] Pradeep Lall, Junchao Wei, and Lynn Davis. *Solid-State Lighting Life Prediction Using Extended Kalman Filter*. Tech. rep. RTI International, Durham, NC (United States), July 2013. DOI: 10.1115/IPACK2013-73288.

[68] *Lamp Controlgear - Part 1: General and Safety Requirements*. International Standard DIN EN 61347-1:2021-08. International Electrotechnical Commission, Aug. 2021.

[69] Christian Sebastian Lamprecht. *Meteostat Python*. Sept. 2022. URL: https://github.com/meteostat/meteostat-python (visited on 13. Sept. 2022).

[70] D. J. Lando, J. P. Mitchell, and T. L. Welsher. “Conductive Anodic Filaments in Reinforced Polymeric Dielectrics: Formation and Prevention”. In: *17th International Reliability Physics Symposium*. Apr. 1979, pp. 51–63. DOI: 10.1109/IRPS.1979.362871.

[71] Kevin Lane, Chiara Delmastro, and Fabian Voswinkel. *Lighting*. Tech. rep. Paris: IEA, Nov. 2021. URL: https://www.iea.org/reports/lighting (visited on 17. Sept. 2022).

[72] Jianying Li et al. “The Degradation of Epoxy Resin-Coated ZnO Varistors at Elevated Temperatures and Ambient Humidity Conditions”. In: *Active and Passive Electronic Components* 26.4 (2003), pp. 235–243. ISSN: 0882-7516, 1563-5031. DOI: 10.1080/0882751031000116205.

[73] Wu Lifeng et al. “Effect of Electrolytic Capacitors on the Life of SMPS”. In: *Journal of Convergence Information Technology* 6.6 (2011), pp. 491–499. ISSN: 1975-9320.

[74] *Littelfuse Varistors - Basic Properties, Terminology and Theory*. Application Note AN9767.1. Littelfuse, Inc., July 1999. URL: https://www.littelfuse.com/~/media/electronics_technical/application_notes/varistors/littelfuse_varistors_basic_properties_terminology_and_theory_application_note.pdf (visited on 17. Feb. 2022).

[75] Jun Liu et al. “Statistical Pulse Degradation Characteristics of Grain Boundaries in a ZnO Varistor Based on Microcontact Measurement”. In: *Journal of the American Ceramic Society* 93.9 (2010), pp. 2473–2475. ISSN: 1551-2916. DOI: 10.1111/j.1551-2916.2010.03834.x.

[76] *LNK302/304-306 LinkSwitch-TN Family*. Datasheet. power integrations, Sept. 2020. URL: https://www.power.com/sites/default/files/product-docs/lnk302_304-306.pdf (visited on 5. Oct. 2021).

[77] *Low-Voltage Surge Protective Devices - Part 11: Surge Protective Devices Connected to Low-Voltage Power Systems - Requirements and Test Methods*. International Standard DIN EN 61643-11:2019-03. International Electrotechnical Commission, Mar. 2019.

[78] Paulo. C. V. Luz et al. “An Integrated Insulated Buck-Boost-Flyback Converter to Feed LED’s Lamps to Street Lighting with Reduced Capacitances”. In: *2014 11th IEEE/IAS International Conference on Industry Applications*. Dec. 2014, pp. 1–6. DOI: 10.1109/INDUSCON.2014.7059432.

[79] N. Mantel. “Evaluation of Survival Data and Two New Rank Order Statistics Arising in Its Consideration”. In: *Cancer Chemother Rep* 50.3 (Mar. 1966), pp. 163–170. ISSN: 0069-0112.

[80] Perry L. Martin. *Electronic Failure Analysis Handbook: Techniques and Applications for Electronic and Electrical Packages, Components, and Assemblies*. McGraw-Hill Handbooks. New York, NY: McGraw-Hill, 1999. ISBN: 978-0-07-041044-2.

[81] E. A. Maxwell. “Analysis of Contingency Tables and Further Reasons for Not Using Yates Correction in 2×2 Tables”. In: *The Canadian Journal of Statistics / La Revue Canadienne de Statistique* 4.2 (1976), pp. 277–290. ISSN: 0319-5724. DOI: 10.2307/3315141.

[82] CM Mc Brien and S Heltzel. “Insulation Resistance of Dielectric Materials under Environmental Testing”. In: *IPC APEX EXPO Conference Proceedings, San Diego, US*. 2013.

[83] F. A. Modine and R. B. Wheeler. “Pulse Response Characteristics of ZnO Varistors”. In: *Journal of Applied Physics* 67.10 (May 1990), pp. 6560–6566. ISSN: 0021-8979. DOI: 10.1063/1.345135.

[84] Dirk F. Moore. *Applied Survival Analysis Using R*. 1st ed. 2016. Use R! Cham: Springer International Publishing : Imprint: Springer, 2016. ISBN: 978-3-319-31245-3. DOI: 10.1007/978-3-319-31245-3.

[85] National Aeronautics and Space Administration. *Tin Whisker (and Other Metal Whisker) Homepage*. Tech. rep. URL: https://nepp.nasa.gov/whisker/.

[86] *Nationwide Failure of AEL Manufactured LED Streetlights*. July 2021. URL: https://nightskysantafe.org/blog/nationwide-failure-of-ael-streetlights/ (visited on 26. Feb. 2022).

[87] Wayne Nelson. *Accelerated Testing Statistical Models, Test Plans, and Data Analyses*. 1st. Wiley-Interscience Paperback Series. Wiley-Interscience, 2009. ISBN: 0-471-69736-2.

[88] Next Generation Lighting Industry Alliance. *LED Luminaire Lifetime: Recommendations for Testing and Reporting*. Tech. rep. 3rd Edition. Solid-State Lighting Product Quality Initiative, Sept. 2014. URL: https://www.energy.gov/sites/prod/files/2015/01/f19/led_luminaire_lifetime_guide_sept2014.pdf (visited on 21. Dec. 2021).

[89] NI. *NI-VISA Overview*. URL: https://www.ni.com/en-us/support/documentation/supplemental/06/ni-visa-overview.html (visited on 6. Mar. 2022).

[90] Patrick D. T. O’connor. “Arrhenius and Electronics Reliability”. In: *Qual. Reliab. Engng. Int.* 5.4 (Oct. 1989), pp. 255–255. ISSN: 07488017, 10991638. DOI: 10.1002/qre.4680050402.

[91] Lyudmyla Panaschenko. “The Art of Metal Whisker Appreciation: A Practical Guide for Electronics Professionals”. In: *IPC International Tin Whisker Conference*. GSFC. CPR. 01105.2012. 2012.

[92] Julie Paye, Albert Claudi, and Matthias Stecher. “High Voltage Robustness of Mold Compounds under Different Environmental Conditions”. In: *2015 IEEE International Reliability Physics Symposium*. Apr. 2015, CP.5.1–CP.5.6. DOI: 10.1109/IRPS.2015.7112792.

[93] Milton O. Peach. “Mechanism of Growth of Whiskers on Cadmium”. In: *Journal of Applied Physics* 23.12 (Dec. 1952), pp. 1401–1403. ISSN: 0021-8979, 1089-7550. DOI: 10.1063/1.1702147.

[94] M. Pecht. “A Model for Moisture Induced Corrosion Failures in Microelectronic Packages”. In: *IEEE Transactions on Components, Hybrids, and Manufacturing Technology* 13.2 (June 1990), pp. 383–389. ISSN: 1558-3082. DOI: 10.1109/33.56172.

[95] D. Stewart Peck. “Comprehensive Model for Humidity Testing Correlation”. In: *24th International Reliability Physics Symposium*. IEEE, 1986, pp. 44–50. DOI: 10.1109/IRPS.1986.362110.

[96] Richard Peto and Julian Peto. “Asymptotically Efficient Rank Invariant Test Procedures”. In: *Journal of the Royal Statistical Society. Series A (General)* 135.2 (1972), pp. 185–207. ISSN: 00359238. DOI: 10.2307/2344317.

[97] *PISE-A150D 150W Output Power with DALI*. Datasheet. LG Innotek, Sept. 2016.

[98] *Platinous J Series*. Catalogue. ESPEC, May 2013.

[99] *Platinous K Series*. Catalogue. ESPEC, June 2009.

[100] Emilie Raguso. *Berkeley to Replace All Its Streetlights Due to Elevated Failure Rates*. Feb. 2019. URL: https://www.berkeleyside.org/2019/02/19/berkeley-to-replace-all-its-streetlights-due-to-elevated-failure-rates (visited on 26. Feb. 2022).

[101] W.J. Ready et al. “Conductive Anodic Filament Enhancement in the Presence of a Polyglycol-Containing Flux [PWBs]”. In: *Proceedings of International Reliability Physics Symposium*. Apr. 1996, pp. 267–273. DOI: 10.1109/RELPHY.1996.492129.

[102] Jeff Reback et al. *Pandas-Dev/Pandas: Pandas 1.0.3*. Zenodo. Mar. 2020. DOI: 10.5281/ZENODO.3715232.

[103] *Reliability Prediction of Electronic Equipment*. Military Handbook MIL-HDBK-217F-2. Washington, DC: Department of Defense, US, Feb. 1995.

[104] *Requirements for Power Conversion Devices for the Computer and Telecommunications Industries*. International Standard IPC-9592. IPC, Sept. 2008.

[105] Rudolf Barnholt. “Mehr Ausfälle Bei Straßenbeleuchtung”. In: *NGZ Online* (). URL: https://rp-online.de/nrw/staedte/kaarst/mehr-ausfaelle-bei-strassenbeleuchtung_aid-20564945 (visited on 26. Feb. 2022).

[106] *Safety Application Guide for Varistors for use in electronic equipment*. Tech. rep. JEITA EMAJ-R039. Japan Electronics and Information Technology Association, Sept. 2002.

[107] *Safety of Electronic Equipment within the Field of Audio/Video, Information Technology and Communication Technology*. International Standard DIN EN IEC 62368-1:2021-05. International Electrotechnical Commission, May 2021.

[108] Sarah D. Shepherd et al. “New Understandings of Failure Modes in SSL Luminaires”. In: *SPIE Optical Engineering + Applications*. Vol. 9190. SPIE, 2014. DOI: 10.1117/12.2062243.

[109] Ian Robertson Sinclair. *Passive Components: A User’s Guide*. Oxford: Heinemann Newnes, 1990. ISBN: 978-0-434-91856-0.

[110] P. Singh. “Power MOSFET Failure Mechanisms”. In: *INTELEC 2004. 26th Annual International Telecommunications Energy Conference*. Sept. 2004, pp. 499–502. DOI: 10.1109/INTLEC.2004.1401515.

[111] Bhanu Sood, Michael Osterman, and Michael Pecht. “Tin Whisker Analysis of Toyota’s Electronic Throttle Controls”. In: *Circuit World* 37.3 (Aug. 2011), pp. 4–9. ISSN: 0305-6120. DOI: 10.1108/03056121111155611.

[112] *Steady-State Temperature-Humidity Bias Life Test*. Tech. rep. JESD22-A101D. JEDEC Solid State Technology Association, July 2015.

[113] *Stress-Test-Driven Qualification of Integrated Circuits*. Tech. rep. JESD47I. JEDEC Solid State Technology Association, July 2012.

[114] *TEA172X 5 W to 11 W Power Supply/USB Charger*. Application Note AN11060. NXP, June 2012. URL: https://www.nxp.com/docs/en/application-note/AN11060.pdf (visited on 10. Feb. 2022).

[115] S. Tominaga et al. “Stability and Long Term Degradation of Metal Oxide Surge Arresters”. In: *IEEE Trans. on Power Apparatus and Syst.* PAS-99.4 (July 1980), pp. 1548–1556. ISSN: 0018-9510. DOI: 10.1109/TPAS.1980.319580.

[116] Torsten Bronger et al. *PyVISA*. GitHub Repository. URL: https://github.com/pyvisa/pyvisa (visited on 6. Mar. 2022).

[117] *Transistor Manual*. Sixth. Syracuse, NY: General Electric Company, 1962. URL: https://books.google.de/books?id=aMIQAQAAMAAJ.

[118] TU Darmstadt Fachgebiet Lichttechnik, TU Darmstadt Fachgebiet Integrierte Elektronische Systeme, and VDE Prüf- und Zertifizierungsinstitut GmbH. *Zuverlässigkeit Und Lebensdauer von LED-Komponenten, Modulen Und Systemen Und Konsequenz Für Die Auslegung Langzeitstabiler LED/OLED-Leuchten (PQL2)*. Tech. rep. AiF IGF 19278 N. Jan. 2020. URL: https://www.fv-elektrotechnik.de/files/fv/schlussberichte/Schlussbericht%20IGF%2019278%20N%20PQL2.PDF.

[119] NOAA US Department of Commerce. *NWS JetStream - Heat Index*. URL: https://www.weather.gov/jetstream/hi (visited on 19. Sept. 2022).

[120] Vadimas Verdingovas, Morten Stendahl Jellesen, and Rajan Ambat. “Impact of NaCl Contamination and Climatic Conditions on the Reliability of Printed Circuit Board Assemblies”. In: *IEEE Transactions on Device and Materials Reliability* 14.1 (Mar. 2014), pp. 42–51. ISSN: 1558-2574. DOI: 10.1109/TDMR.2013.2293792.

[121] Vadimas Verdingovas, Morten Stendahl Jellesen, and Rajan Ambat. “Solder Flux Residues and Humidity-Related Failures in Electronics: Relative Effects of Weak Organic Acids Used in No-Clean Flux Systems”. In: *Journal of Electronic Materials* 44.4 (2015), pp. 1116–1127. ISSN: 0361-5235.

[122] Pauli Virtanen et al. “SciPy 1.0: Fundamental Algorithms for Scientific Computing in Python”. In: *Nature Methods* 17 (2020), pp. 261–272. DOI: 10.1038/s41592-019-0686-2.

[123] Samu Vuorela and Aulis Tuominen. “Designing a Measurement System for Monitoring the Performance of LED Drivers during Environmental Accelerated Life Testing”. In: *2012 IEEE International Conference on Power System Technology, POWERCON 2012* (2012), pp. 1–4. ISSN: 9781467328685. DOI: 10.1109/PowerCon.2012.6401367.

[124] Beibei Wang et al. “A Method of Reducing the Peak-to-Average Ratio of LED Current for Electrolytic Capacitor-Less AC–DC Drivers”. In: *IEEE Transactions on Power Electronics* 25.3 (Mar. 2010), pp. 592–601. ISSN: 1941-0107. DOI: 10.1109/TPEL.2009.2031319.

[125] Huai Wang and Frede Blaabjerg. “Reliability of Capacitors for DC-Link Applications in Power Electronic Converters - An Overview”. In: *IEEE Trans. on Ind. Applicat.* 50.5 (Sept. 2014), pp. 3569–3578. ISSN: 9781479903351. DOI: 10.1109/TIA.2014.2308357.

[126] Mao-hua Wang, Qing-hua Tang, and Chao Yao. “Electrical Properties and AC Degradation Characteristics of Low Voltage ZnO Varistors Doped with Nd2O3”. In: *Ceramics International* 36.3 (Apr. 2010), pp. 1095–1099. ISSN: 0272-8842. DOI: 10.1016/j.ceramint.2009.12.006.

[127] Mao-hua Wang et al. “Degradation Phenomena Due to Humidity in Low Voltage ZnO Varistors”. In: *Ceramics International* 33.2 (Mar. 2007), pp. 151–154. ISSN: 02728842. DOI: 10.1016/j.ceramint.2005.08.009.

[128] WG A3.17. *Metal Oxide (MO) Surge Arresters - Stresses and Test Procedures*. Technical Brochure 544. cigré, Aug. 2013. URL: https://e-cigre.org/publication/544-metal-oxide-mo-surge-arresters---stresses-and-test-procedures (visited on 16. Aug. 2022).

[129] G. N. Wilkinson and C. E. Rogers. “Symbolic Description of Factorial Models for Analysis of Variance”. In: *Journal of the Royal Statistical Society. Series C (Applied Statistics)* 22.3 (1973), pp. 392–399. ISSN: 0035-9254. DOI: 10.2307/2346786.

[130] Jim Williams. *A Monolithic Switching Regulator with 100μV Output Noise*. Application Note 70. Linear Technology, Oct. 1997. URL: https://www.analog.com/media/en/technical-documentation/application-notes/an70.pdf (visited on 16. Aug. 2022).

[131] Steve Winder. *Power Supplies for LED Drivers*. Elsevier, 2008. ISBN: 978-0-7506-8341-8. DOI: 10.1016/B978-0-7506-8341-8.X0001-1.

[132] Wright Laboratory, Wright-Patterson Air Force Base, Ohio. “Failure Mechanism in Avionics Equipment Preventable by Dehumidification”. In: *FY 1997 Small Business Innovation Research (SBIR) Program - Program Solicitation*. Washington: U.S. Department of Defense, Jan. 1997, p. 246. URL: https://apps.dtic.mil/sti/pdfs/ADA324385.pdf (visited on 2. Mar. 2022).

[133] R. Wu et al. “Overview of Catastrophic Failures of Freewheeling Diodes in Power Electronic Circuits”. In: *Microelectronics Reliability* 53.9-11 (Sept. 2013), pp. 1788–1792. ISSN: 00262714. DOI: 10.1016/j.microrel.2013.07.126.

[134] F. Yates. “Contingency Tables Involving Small Numbers and the X2 Test”. In: *Supplement to the Journal of the Royal Statistical Society* 1.2 (1934), pp. 217–235. ISSN: 1466-6162. DOI: 10.2307/2983604.

[135] Shen Zhan, Michael H. Azarian, and Michael Pecht. “Reliability of Printed Circuit Boards Processed Using No-Clean Flux Technology in Temperature–Humidity–Bias Conditions”. In: *IEEE Transactions on Device and Materials Reliability* 8.2 (2008), pp. 426–434. DOI: 10.1109/TDMR.2008.922908.

[136] G. Q. Zhang et al., eds. *Mechanics of Microelectronics*. Vol. 141. Solid Mechanics and Its Applications. Dordrecht: Springer Netherlands, 2006. ISBN: 978-1-4020-4934-7 978-1-4020-4935-4. DOI: 10.1007/1-4020-4935-8.

A List of All Tested Devices by UID

UID	Manufacturer	Manufacturer part number	Tested in
V001	OSRAM	OT 40/120-277/1A0 4DIMLT2 E	85 °C dry heat
V002	OSRAM	OT 40/120-277/1A0 4DIMLT2 E	75 °C/75 %
V003	OSRAM	OT 40/120-277/1A0 4DIMLT2 E	85 °C/85 %
V004	OSRAM	OT 40/120-277/1A0 4DIMLT2 E	65 °C/90 %
V007	LG Innotek	LLP 150W 0.7A 125 280Vdc PISE-A150D	85 °C/85 %
V008	LG Innotek	LLP 150W 0.7A 125 280Vdc PISE-A150D	85 °C dry heat
V009	LG Innotek	LLP 150W 0.7A 125 280Vdc PISE-A150D	65 °C/90 %
V010	LG Innotek	LLP 150W 0.7A 125 280Vdc PISE-A150D	75 °C/75 %
V014	Philips	CertaFlux LLS ES 1150m 4500lm 840 HVI MST	85 °C dry heat
V015	Philips	CertaFlux LLS ES 1150m 4500lm 840 HVI MST	75 °C/75 %
V016	Philips	CertaFlux LLS ES 1150m 4500lm 840 HVI MST	65 °C/90 %
V024	Philips	CertaFlux LLS ES 1150m 4500lm 840 HVI MST	85 °C/85 %
V025	OSRAM	OT 165/170-240/1A0 4DIMLT2 E	85 °C dry heat
V030	BAG	CCS1150-50FR-20/220-240	85 °C dry heat
V031	BAG	CCS1150-50FR-20/220-240	85 °C/85 %
V032	BAG	CCS1150-50FR-20/220-240	75 °C/75 %
V033	BAG	CCS1150-50FR-20/220-240	65 °C/90 %
V036	BAG	CCS170-35QS-01/220-240	85 °C dry heat
V038	BAG	CCS170-35QS-01/220-240	85 °C/85 %
V039	BAG	CCS170-35QS-01/220-240	75 °C/75 %
V040	BAG	CCS170-35QS-01/220-240	65 °C/90 %
V042	TRIDONIC	LC 25W 100-500mA flexC lp EXC	85 °C dry heat
V043	BAG	LCS130-70FX-30/220-240	85 °C dry heat
V045	BAG	LCS130-70FX-30/220-240	85 °C/85 %
V046	BAG	LCS130-70FX-30/220-240	75 °C/75 %
V047	BAG	LCS130-70FX-30/220-240	65 °C/90 %
V049	Philips	Xitanium 9290 008 818	85 °C dry heat
V050	OSRAM	OT FIT 35/220-240/700 CS	85 °C dry heat
V051	OSRAM	OT FIT 35/220-240/700 CS	85 °C/85 %
V052	OSRAM	OT FIT 35/220-240/700 CS	75 °C/75 %
V053	OSRAM	OT FIT 35/220-240/700 CS	65 °C/90 %
V056	WE-EF	ED100-66/700-1050/230-50-60/O-O	85 °C dry heat
V058	WE-EF	ED100-66/700-1050/230-50-60/O-O	85 °C/85 %
V059	WE-EF	ED100-66/700-1050/230-50-60/O-O	85 °C/85 %
V060	WE-EF	ED100-66/700-1050/230-50-60/O-O	75 °C/75 %
V061	WE-EF	ED100-66/700-1050/230-50-60/O-O	65 °C/90 %

V062	OSRAM	OTi DALI 60/220-240/550 D LT2 L	85 °C dry heat
V063	OSRAM	OTi DALI 90/220-240/1A0 LT2 L	85 °C dry heat
V064	OSRAM	OTi DALI 60/220-240/550 D LT2 L	85 °C/85 %
V065	OSRAM	OTi DALI 90/220-240/1A0 LT2 L	85 °C/85 %
V066	OSRAM	OTi DALI 60/220-240/550 D LT2 L	65 °C/90 %
V067	OSRAM	OTi DALI 90/220-240/1A0 LT2 L	75 °C/75 %
V068	OSRAM	OTi DALI 60/220-240/550 D LT2 L	75 °C/75 %
V069	OSRAM	OTi DALI 90/220-240/1A0 LT2 L	65 °C/90 %
V075	Vossloh-Schwabe	ECXe 700.199	85 °C dry heat
V076	Vossloh-Schwabe	ECXe 700.199	75 °C/75 %
V077	Vossloh-Schwabe	ECXe 700.199	65 °C/90 %
V081	Vossloh-Schwabe	ECXe 700.199	85 °C/85 %
V084	Vossloh-Schwabe	ECXd 700.149	85 °C/85 %
V086	Vossloh-Schwabe	ECXd 700.149	75 °C/75 %
V087	Vossloh-Schwabe	ECXd 700.149	65 °C/90 %
V088	Vossloh-Schwabe	ECXd 700.149	85 °C/85 %
V091	Vossloh-Schwabe	ECXd 700.149	85 °C/85 %
V092	Vossloh-Schwabe	ECXd 700.149	85 °C dry heat
V095	Philips	Xitanium 9290 008 818	75 °C/75 %
V096	Philips	Xitanium 9290 008 818	65 °C/90 %
V097	Philips	Xitanium 9290 008 818	85 °C/85 %
V100	TRIDONIC	LC 25W 100-500mA flexC lp EXC	85 °C/85 %
V101	TRIDONIC	LC 25W 100-500mA flexC lp EXC	65 °C/90 %
V102	TRIDONIC	LC 25W 100-500mA flexC lp EXC	75 °C/75 %
V104	OSRAM	OT 165/170-240/1A0 4DIMLT2 E	65 °C/90 %
V105	OSRAM	OT 165/170-240/1A0 4DIMLT2 E	85 °C/85 %
V107	ERP	PSB30E-0700-42-T	85 °C/85 %
V111	TRIDONIC	LC 57/1050/54 fixC lp SNC2	85 °C/85 %
V116	LUMNIUM	54H-120B-GM-0450	85 °C/85 %
V118	Vossloh-Schwabe	ECXe 1050.233	85 °C/85 %
V119	Vossloh-Schwabe	ECXe 1050.233	85 °C/85 %
V123	Vossloh-Schwabe	ECXe 350.298	85 °C/85 %
V124	Vossloh-Schwabe	ECXe 350.298	85 °C/85 %
V128	Philips	CertaDrive 60W 360mA 170V 230V	85 °C/85 %
V134	N/A	LGM22W016P2	85 °C/85 %
V137	N/A	LGM52W041P2	85 °C/85 %
V144	N/A	CLNC24W028L	85 °C/85 %
V149	N/A	CLNC65W042L	85 °C/85 %

List of Own Publications

[137] L. Shen, F. Keil, and K. Hofmann. *Stabilization Methods for Integrated High Voltage Charge Pumps*. 2014.

[138] K. Hirmer et al. *Low-Cost High-Voltage Arbitrary Waveform Generator for Broad Lifetime Measurements of Electroluminescent Devices*. 2016.

[139] Franz Siegltrum et al. “Werkzeughalter mit integrierter Sensorik”. DE102015220533A1. Apr. 2017. URL: https://patents.google.com/patent/DE102015220533A1/de?oq=siegltrum+keil (visited on 19. Sept. 2022).

[140] Christian Mandel et al. “Bauteil mit einer Antenne”. DE102016117092A1. Mar. 2018. URL: https://patents.google.com/patent/DE102016117092A1/en?q=keil+kim&inventor=hofmann&oq=hofmann+keil+kim (visited on 19. Sept. 2022).

[141] Dominik Großkurth, Klaus Hofmann, and Ferdinand Keil. “Batteriebetriebene Vorrichtung zur Auswertung von Sensorsignalen”. DE102017121933A1. Mar. 2019. URL: https://patents.google.com/patent/DE102017121933A1/en?q=keil&inventor=gro%C3%9Fkurth&oq=gro%C3%9Fkurth+keil (visited on 19. Sept. 2022).

[142] F. Keil and K. Hofmann. “A Comparative Study of the Lifetimes of High-End and Low-Cost Off-Line LED Drivers Under Accelerated Test Conditions”. In: *2019 16th China International Forum on Solid State Lighting & 2019 International Forum on Wide Bandgap Semiconductors China (SSLChina: IFWS)*. IEEE, 2019, pp. 231–234. DOI: 10.1109/SSLChinaIFWS49075.2019.9019814.

[143] T. Schmeiser et al. “Einstellung von Patienten mit entzündlich-rheumatischen Erkrankungen zur immunsuppressiven Therapie im Rahmen der COVID-19 Pandemie – eine Situationsanalyse”. In: *Z Rheumatol* 79.4 (May 2020), pp. 379–384. ISSN: 0340-1855, 1435-1250. DOI: 10.1007/s00393-020-00800-8.

[144] Tim Schmeiser et al. “Evaluation von Patienten mit entzündlich-rheumatischen Erkrankungen unter Immunsuppressiva und ihrer Haltung zur Medikation im zeitlichen Verlauf der Covid-19 Pandemie”. In: *Deutscher Rheumatologiekongress 2020* 48. Kongress der Deutschen Gesellschaft für Rheumatologie (Sept. 2020), 34. Jahrestagung der Deutschen Gesellschaft für Orthopädische Rheumatologie (DGORh). DOI: 10.3205/20DGRH001.

[145] R Hasseli et al. “The Influence of the SARS-CoV-2 Lockdown on Patients with Inflammatory Rheumatic Diseases on Their Adherence to Immunomodulatory Medication: A Cross Sectional Study over 3 Months in Germany”. In: *Rheumatology* 60.SI (Oct. 2021), SI51–SI58. ISSN: 1462-0324, 1462-0332. DOI: 10.1093/rheumatology/keab230.

[146] Ferdinand Keil and Klaus Hofmann. “An Alternative Approach to Traditional Lifetime Testing Based on Comparative Studies and Survival Analysis”. In: *MikroSystemTechnik Congress 2021; Congress*. Nov. 2021, pp. 1–4.

[147] Ferdinand Keil, David Riehl, and Klaus Hofmann. "Converting an Undergrad-Lab to an Interactive E-Learning Experience That Enables Student Teamwork". In: *2021 IEEE Frontiers in Education Conference (FIE)*. Oct. 2021, pp. 1–5. DOI: 10.1109/FIE49875.2021.9637206.

[148] Ferdinand Keil, David Riehl, and Klaus Hofmann. "Statistische Auswertung von Lebensdaueruntersuchungen an elektronischen Baugruppen mit Python". In: *11. DVS/GMM-Fachtagung*. Vol. 375. Fellbach, Germany: DVS Media, June 2022, pp. 316–320. ISBN: 978-3-96144-166-2. URL: https://www.ebl-fellbach.de/ (visited on 14. Sept. 2022).

[149] Ferdinand Keil et al. "Model-Based Analysis of Accelerated Lifetime Test Data of Off-Line LED Drivers". In: *34. Workshop Testmethoden Und Zuverlässigkeit von Schaltungen Und Systemen (TuZ 2022)*. Bremerhaven, Germany, Feb. 2022. URL: http://www.informatik.uni-bremen.de/tuz/2022 (visited on 14. Sept. 2022).

Supervised Theses

[150] Thomas Schrauth. *Optimierung Einer Operationsverstärkerschaltung Zur Auswertung Eines Fluidistors Hinsichtlich Des Elektrischen Rauschverhaltens*. Bachelor's Thesis. Oct. 2016.

[151] Tobias Leipe. *Entwurf Und Umsetzung Einer Elektronik-Experimentierplattform - Drum Machine*. Bachelor's Thesis. May 2017.

[152] Benjamin Lars Northe. *Entwicklung Einer Schaltung Zur Elektrischen Emulation Schnell Veränderlicher Widerstandsthermometer*. Bachelor's Thesis. Nov. 2017.

[153] David Riehl. *Entwurf Eines Induktiv Gekoppelten Energie- Und Datenübertragungssystems Für in Hohlwellen Integrierte Drehmomentsensoren*. Bachelor's Thesis. Aug. 2017.

[154] Chengyang Wang. *Entwicklung Einer Optimierten Ansteuerung Für Ein Rekonfigurierbares Antennensystem*. Master's Thesis. June 2017.

[155] Benjamin Wörfel. *Entwurf Und Umsetzung Eines Ultraschall-Durchflusssensors*. Master's Thesis. July 2017.

[156] Gayathri Satish Bhatt. *Analyzing Motor Oil Impedance Measurements Using Neural Networks*. Master's Thesis. Jan. 2019.

[157] Martin Herold. *Optimierung Eines Induktiv Gekoppelten Daten- Und Energieübertragungssystems*. Master's Thesis. Mar. 2019.

[158] Lukas Marek Boland. *Entwurf Eines Galvanisch Isolierten Datenerfassungssystems Zur Strom- Und Spannungsmessung*. Master's Thesis. Jan. 2020.

[159] Paco Rahn. *Implementierung Einer Klangsynthese Auf Basis Eines Sehr Günstigen Mikrocontrollers*. Bachelor's Thesis. Feb. 2020.

[160] Mahdi Guermazi. *Entwurf Und Optimierung Einer Arduino-Bibliothek Für Die DALI-Schnittstelle*. Bachelor's Thesis. Mar. 2021.

[161] Van Duc Binh Le. *Optimierung Der Bitübertragungsschicht Des DALI Protokolls Durch Den Einsatz Programmierbarer Ein-/Ausgänge*. Bachelor's Thesis. Nov. 2021.

[162] Mohammadmehdi Peiro. *Evaluation Moderner Statistischen Verfahren Zur Modellierung Der Degradation von LEDs*. Master's Thesis. May 2021.

[163] David Witulla. *Entwurf Und Evaluierung Einer Kostengünstigen Audio-Endstufe*. Bachelor's Thesis. Sept. 2021.

[164] Sebastian Zisch. *Implementierung Eines Labor-geeigneten Leistungsanalysators Auf Basis Eines Kommerziellen Leistungsüberwachungs-ICs*. Bachelor's Thesis. Apr. 2021.

[165] Bedis Walha. *Condensation and Contamination Detection on Printed Circuit Boards (PCBs)*. Master's Thesis. Apr. 2022.